Final Technical Report

Innovative Die Material and Lubrication Strategies for Clean and Energy Conserving Forging Technologies

U. S. Department of Energy, Office of Industrial Technologies
Award Number: DE-FC07-01ID14206

Project Period

October 1, 2001 to September 30, 2004

Principal Investigator and Author

Dr. Rajiv Shivpuri
Professor, Industrial, Welding and Systems Engineering
The Ohio State University, 1971 Neil Avenue, Columbus, OH 43210

Recipient Organization

The Ohio State University Research Foundation
Business Officer: David Doty
1960 Kenny Road, Columbus, OH 43210-1063

Team Member Organizations

Provided in the Report

December, 2006

Document Availability

"Reports are available free via the U. S. Department of Energy (DOE) Information Bridge: Web Site http://www.osti.gov/bridge

Reports are available to DOE employees, DOE contractors, Energy Data Exchange (ETDE) representatives, and Informational Nuclear Information System (INIS) representatives from the following source:
Office of Scientific and Technical Information
P. O. Box 62, Oak Ridge, TN 37831
Tel: (865) 576-5728, Fax: (865) 576-5728, E-mail: reports@osti.gov
Web Site: http://www.osti.gov/contact.html

Acknowledgement

This material is based upon work supported by the
U. S. Department of Energy under Award No. "DE-FC07-01ID14206"

Disclaimer

Any opinions, findings, and conclusions or recommendations expressed in this material are those of the author(s) and do not necessarily reflect the views of the Department of Energy."

Proprietary Data Notice

Distribution is Unlimited

Collaborators and Project Partners:

Company	Contact	Phone	Email
Forging Companies:			
FIERF	Karen Lewis	(216) 781-6260	karen@forging.org
	John Nowak (CEO,Walker Forge)	(262) 554-2929	jnowak@walkerforge.com
	George Mochnal Technology Director	(216) 781-6260	george@forging.org
	Bob Swope CEFT Integrator	(330) 904-5361	rms1959@sbcglobal.net
Metaldyne	Mike Crews (Minerva)	(614) 866-8960	michaelcrews@metaldyne.com
	Ben Beaumont (MHO)	(248) 577-8917	benbeaumont@metaldyne.com
	Padma Durbha (MHQ)	(734) 354- 4007	padmadurbha@metaldyne.com
	Murali Bhupathiraju (Plymouth)	(734) 207-6766	murali@metaldyne.com
American Axle	John Pale	(800) 299-2953	John.pale@aam.com
	Inacio Moriguchi	(313) 758-4524	Inacio.Moriguchi@aam.com
	Bob Greczanik (Colfor)	(800) 299-2953	bob.greczanik@aam.com
Sypris	Tom Blankenship	(740) 223-4309	Tom.Blankenship@sypris.com
APP	David Silva	(714) 546-8125	DSilva0829@aol.com
Wyman Gordon	Tony Dumm	(216) 341-0085	tdumm@dropdies.com
GKN Forging	Hank Knott	(248) 371-0800	Hank.Knott@gknsintermetals.com
Alcoa Forged Products	Ralph Sawtell Director R&D	(216) 641-3600	Ralph.sawtell@alcoa.com
Weber Metals	Thomas Stys	(562) 602-0260	Tom.stys@weber.com
Elwood Texas Forge	C. Todd Kidder	(713) 434-5177	tkidder@etf.elwd.com
Lubrication Companies			
Balzers	Dennis Quinto	(207)-839-4372	dennis.quinto@balzers.com
Acheson	Dale Hutchinson	(716) 799-0602	dale.hutchinson@nstarch.com
CMT	Raimo Peltneimi	(704) 423-3310	rpeltoniemi@cmt-solutions.com
Superior Graphite	Bruce Welis	(773) 890-4116	BWells@GraphiteSGC.com
Fuchs	Tim Russell	(724) 867-5000	trussell@fuchs.com
Dylon	Jeff Kondilas	(216) 651-1300	Jkondilas@dylon.com
Die Coating Companies			
Optomec Inc	Rich Plourde	(410) 465-9557	rplourde@optomec.com
Stellite	James Wu	(314) 983-0266	jwu@stellite.com
Balzers	Dennis Quinto	(207)-839-4372	dennis.quinto@balzers.com
Nitrex	M. Waryszewski	(514) 335-7191	maxwarys@nitrex.com
	Witol Liliental	(905) 319-9258	wliliental@nitrexmetaltech.com
Advanced Heattreat	Edward Rolinski	(734)243-0063	research@foxberry.net

Ion Bond	Bernard Janoss	(248) 398-9100	b.janoss@us.ionbond.com
Teikuro Corp	Tohru Arai	(987) 325-9900	ToruTarai@aol.com
Die Material/ Heat Treat Companies			
Kowalski Heat treatment	Steve Kowalski	(216) 631-4411	N/A
Uddeholm	Patricia Miller	(847) 577-2220	Pat.Miller@bucorp.com
Finkl	Algaridas Undersys	(773) 975-2510	alu@finkl.com
Allvac	Thomas Bayha	(704) 292-7127	tom.bayha@allvac.com
Crucible	Ed Severson	(800) 365-1185	eseverson@crucibleservice.com
Steel and Aluminum Producers			
Chaparrel Steel	Peter Wright	(972) 299-5212	N/A
Macsteel	Paul Dimitry	(800) 876-7833	PDimitry@macsteel.com
Timken Steel	Praveen Pauskar	(330) 471-2280	pauskarp@timken.com
Suppliers: Software, Instrumentation			
SFTC	Andy Tang	(614) 451-8330	sales@deform.com
FORGE Software	Etienne Wey	+33 (0) 492924204	info@transvalor.com
OGTechnologies	Shuh Chang	(734) 973-7500	chang@ogtechnologies.com
Flir Systems	Terry Ruane	(440) 871-1134	Terry.ruane@FLIR.com
National Instruments	Matt Rings	(614) 876-6221	mathew.rings@ni.com
Original Equipment Producers (OEMs)			
Sikorsky	William C. Harris	(203) 386-3568	wharris@sikorsky.com
Ford Motor Company	Mel Evans	(313) 621-0777	mevans3@ford.com
Universities/ DOE Labs			
Wright State University	Ramana Grandhi	(937) 775-5090	rgrandhi@cs.wright.edu
	Raghu Srinivasan	(937) 775-5093	raghavan.srinivasan@wright.edu
ORNL	Camden Hubbard	(865) 574-4472	hubbardcr@ornl.gov
Argonne	Ali Erdimir	(630) 252-6571	erdimir@anl.gov

TABLE OF CONTENTS

List of Figures

List of Tables

EXECUTIVE SUMMARY

This final technical report contains the work carried out in the project "Innovative Die Material and Lubrication Strategies for Clean and Energy Conserving Forging Technologies" partially funded by the U.S. Department of Energy under the Award No. DE-FC07-01ID14206. The contracted time for project performance was September 30, 2001 to September 29, 2005. However, DOE/OIT was unable to provide funds for the last two years fiscal years 2003 and 2004 and the project was terminated prematurely in FY 2003-04. Consequently, many of the major research tasks were either modified to achieve a certain milestone or terminated without completion.

Dr. Rajiv Shivpuri, Professor of Industrial, Welding and Systems Engineering, The Ohio State University, was the Project Director and the Principal Investigator for this project. The award was administered by the Ohio State University Research Foundation (OSURF). OSURF was also responsible for all fiscal and administrative matters. The fiscal report is submitted separately. At the Department of Energy, Office of Industrial Technologies, the program managers were Mr. Ramesh Jain and Mr. Dibyajyoti Aichbhowmik at Golden Office.

The main accomplishments in this project were the following:

- A major collaborative effort was established with the forging industry and their suppliers to explore innovative die materials and lubrication strategies for industrial applications. This included workshops and symposium coordinated with forging industry. Presentations were made at the Forging Industry Technical Conferences to disseminate the results throughout the forging industry.
- A Center for Excellence in Forging Technology was established under sponsorship of the Forging Industry Association and the Forging Industry Education and Research Foundation. As a part of this Center two forging cells were installed with industry, OSU, State of Ohio and DOE support: A 1300 ton mechanical press cell and a 350 ton hydraulic press cell. This was a $1.5 million commitment to the forging research.
- Innovative die coatings were explored including the LENS (Laser Enhanced Net Shaping) based Nickel Aluminide coating overlay (details in Appendix A).
- An innovative experimental set up and predictive thermal softening software was developed to optimally select and design die materials for hot forging applications (Appendices B, C and D).
- A lubrication strategy and single droplet based lubrication models were developed for optimal deposition of hot forging lubricants for spread and heat transfer (Appendices E and F).
- Models were developed for lubricant break up and bounce. These models can be used for the reduction of air and ground water pollution due to graphite lubrication of hot die surfaces. (Appendix G).

This report was prepared by Dr. Shivpuri and Mr. Yijun Zhu (Research Associate). It contains details of the research plan and the tasks that were completed during the project duration, some after the project termination with other external or internal support.

1.0 INTRODUCTION

1.1 Project Goals

The goals of this project wre to develop and implement innovative die materials and lubrication strategies to increase die lives by 8X, decrease energy input by 15% and energy cost per part by 50%, reduce particulate emissions from lubricants by 90% and increase die related uptime to 90%. The strategies were selected for maximum and wide energy impact on forging industries, their suppliers (steel and aluminum producers (IOFs), lubricant, surface technology and die material suppliers) and customers (OEMs). They include optimal lubricant spray technology, elimination of graphite in hot forging by advanced surface engineering, gradient die materials and die engineering, lubrication and die enablers for warm forging etc. The forging industry in the U.S. was roughly $12 billion in 1997 (DOD National Security Assessment). Roughly 15% of the total sales value of its products is allocated to energy, an estimated 50 trillion BTUs per year. Environmental impact of use of graphite (in hot forging) and use of conversion coating in cold forging is estimated to add over 20% to the product cost.

The die concept envisioned in this project was a simple one, that of a composite configuration die, shown in Figure 1, with advanced materials and surface coatings strategically selected and located in the die. The objective of the die material design will be to:

- Make the die resistant to abrasive wear, adhesive wear, plastic deformation due to loss in hot hardness, and cracking at sharp internal corners.
- Self-lubricating surface that eliminates the use of lubricants. This surface has to be hard enough to withstand abrasion and adhesion and thermal exposure.

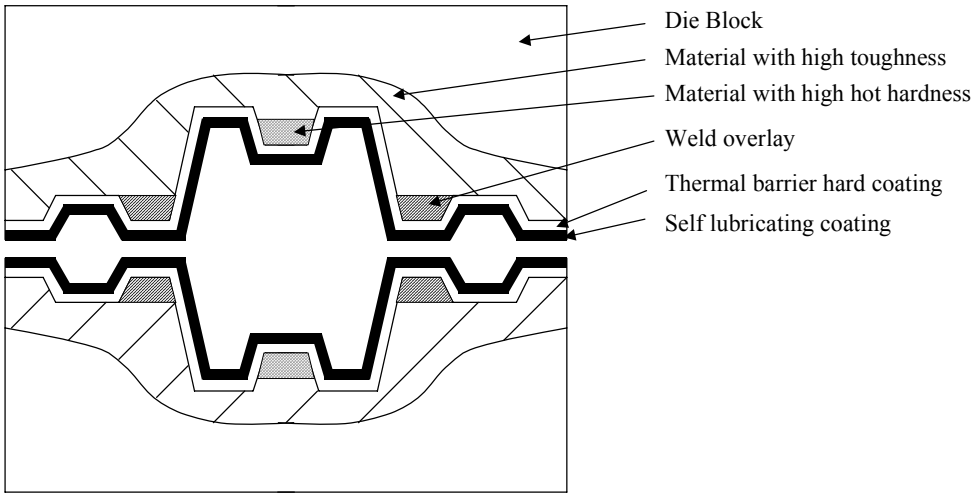

Figure 1: Die configuration for a multi-attribute composite die for high die life and self-lubricating surface

1.2 Energy Savings Expected

Forging sales in US were slightly under $6 billion in 1999. These cover impression die, open die and seamless ring forging. Typical scrap rates in shops that forge to conventional tolerances, ranges anywhere from 5000-10000 ppm. For near net forgings the scrap rate is close to 50,000 ppm (parts per million). Scrap is associated with lack of process control and degradation of tool that is not identified in time.

Hot forging industry spends about $0.06 in energy for every pound of steel forged. Almost 6-8% of cost of a forging is cost of energy. Energy is spent in direct heating of forge stock to required temperatures, operation of press and other equipment, subsequent normalizing and cleaning of forgings. Energy is also used air conditioning and lighting among other indirect uses. Heating is the biggest source of energy consumption in forging industry. For every pound of steel forged, close to 2000 - 4000 BTU of energy is used (based on a average specific heat of about 1-3 BTU/lb/K). Because of inefficiencies in heating and energy consumed in other areas of a forge shop, it could consume over 6000-8000 BTU / lb of steel. Similar numbers can be expected in non-ferrous forging also. Based on a 10,000 ppm scrap rate and a 20% improvement in scrap rate related to premature failure (which may be 20-30% of all scrap), it translates to about 35 BTU per lb of steel forged. Energy is also saved in machining alternate tooling, die repair, heat loss during shut down and startup of furnace and die heating. These factors could put the total energy impact of the project at 50-70 BTU/lb.

Similar results can be realized in Aluminum and Steel industries also. In Aluminum industry, energy consumed in primary production of Aluminum is approximately 23,500 BTU/lb (15.18 kWh/ Kg). Steel processing is one of the highest energy users in US. The steel industry accounts for 2-3% of total U.S. energy consumption. In steel industry, the energy consumed is approximately 10,000 BTU/lb (6.5 kWh/Kg) for primary steel making and secondary processing like rolling and cogging. AISI reports that 12- 15% of the cost of steel made is energy cost. 10-15% of this energy used is in secondary processing of steel (hot and cold rolling, cogging etc). Every pound of aluminum scrapped would result in energy loss of almost 23,500 BTU in the primary processing of aluminum alone. Every pound of steel saved from being scrapped in the forging industry saves energy to the tune of 10,000 BTU for the steel industry.

1.3 Economic Benefits Expected

The forging process is used to manufacture discrete parts for the automotive, appliance, aerospace and construction industry. The $8 billion forging industry consists of a few large shops and hundreds of small shops of mostly independent producers, which employ thousands of workers in their plants. Direct benefits of this research are in the reduction of the following costs involved in forging:

- Die manufacturing costs: These include the cost of the die steel, heat treatment, machining, bench working etc. Die costs are approximately 7% of the cost of forgings. Assuming a project effectiveness of 0.1%, and a 2X improvement in die life, forging industry would save approximately $5 million in direct steel die cost alone. There are additional savings in machining, die repair and heat treatment costs that would potentially double or triple the

savings.

- Operational costs: Cost related to die set up and press down time. Often it is possible to schedule the die mounting and dismounting during the shift break. However, due to variability in the quality of the die steels, the die lives vary considerably and the die downtime may occur during a shift. This results in stoppage of production. A typical die change takes 30 minutes to 6 hours depending on the complexity of assembly and capabilities of the forger. At the rate of $500 / hour of downtime, reduction of one setup would on the average save $1500. A typical midsize forging company reports over 1500* setups / year. Not all setups can be eliminated because batch volumes are not high in custom forging industry. Assuming this can be reduced by 500, savings of approximately $250,000 can be realized.
- Scrap Costs: Down time during a shift results in the production line to be shut down and restarted. This increases scrap and defects related to a non-steady state operation. There is also additional energy spent in induction heater / furnace startup.
- Re-sinking and repair costs for the worn dies: The die blocks can be re-sunk two to three times before a new block has to be used. Die re-sinking does expose new material in the die block that may not have the same mechanical properties as the original material of the cavity.
- Inventory costs: A large inventory of die blocks and pre-machined blocks has to be maintained to minimize die downtime.
- Maintenance and cleaning costs: Less than 10% of lubricant used actually goes into the process. The other 90% contribute to the particulate dispersion that forms thick deposits on machinery, equipment and tools. This results in gradual degradation of performance of the equipment as well as high cleaning costs.

1.4 Environmental Benefits Expected

Forging environment is harsh – smoke, graphite fumes and sound make work environment unpleasant. This graphite-based pollution is serious enough that the National Institute of Occupational Safety and Health (NIOSH) has established a recommended exposure limit for airborne graphite pollution of 2.5 mg/m^3. In fact some of the environmentally conscious states such as California have totally banned the use of oil based graphite lubrication in forge shops. Elimination or lubricant bacteria and better environmental conditions around presses and will significantly reduce the work related hazards and injuries. In addition, the reduction in ground water pollution will affect the neighboring community and reduce pollutants in our waterways. The reduction of post forging machining also significantly reduces the environmental costs associated with machining processes. One of the goals of the project is to reduce the particulate emission in hot forge shops by 10%. This will be achieved by exploring and establishing working domains for environment-friendly lubricants like Dylon and Fuch's LN-1032, reducing colloidal graphite content in lubricant and exploring new techniques for lubricant delivery like encapsulation.

Total emissions from smelting and secondary processing total almost 1.56 lb / lb of aluminum processed, 90% of which is carbon dioxide. In steel processing, in US alone, over 138,000 tons of NOx emissions have been reported (1995). From sintering to cold rolling, total SO2 emissions are over 40 lbs/ton of steel, total Nox emissions are over 15 lbs/ton and other CO and particulate emissions total over 15 lbs/ton of steel manufactured (Source: AISI). There will be a small but significant reduction in pollutants from steel and aluminum industries because of better utilization of the raw materials by the forging industry.

2.0 BACKGROUND

2.1 State of Technology

Forging performed at room (cold) and elevated temperatures (warm and hot) is a poorly understood complex phenomenon that involves evolving metallurgy, tribology at the tool surface and flow characteristics of metal. Technical hurdles that were addressed in this project included

- Lack of knowledge of lubrication behavior in cold and hot forging. The selection of lubricants and lubrication techniques is left to the lubricant and equipment supplier. This results in excessive and poor use of lubricants, and excessive environmental pollution.
- Lack of maturation of emerging surface engineering and die material technologies for advanced forging applications. The technical and fiscal risks of implementing them in actual production are very high which limits their use. The market penetration of these technologies is almost non-existent.
- Lack of computational tools for design optimization of both the die and the lubrication systems.

2.2 Project Pathways

It was planned to realize the project objectives through the following strategies in lubricant and die material technologies.

- Strategy #1: Developing a system for optimal design of lubricant spray process which will eliminate pollution, reduce the use of lubricant, and enable net shaping due to reduced die chill. It will also reduce the need for graphite based lubricants.
- Strategy #2: Developing lubricant and die coating enablers for improved die lives and processes for warm forging (billet heating reduced from 1250F to 900F) of ferrous and non-ferrous parts. The reduction of forging temperatures will result in improved tolerances and tremendous savings in energy per part.
- Strategy #3: Eliminate the use of phos-coatings on the cold forging billets by the use of low friction die surface engineering (DLC (non-ferrous) and WC/C coatings).
- Strategy #4: Develop advanced surface cladding (hard facing by LENS and thermal spray) and duplex coating technologies for hot forging dies. Conventional coatings and surface engineering techniques have failed to deliver substantial gains.
- Strategy #5: Develop software for eliminating in-process die failure and predictive die maintenance in cold and hot forging through material and process design. This will have significant impact on scrap reduction and die related downtime.

Many of the technologies being developed are addressing crosscutting R&D enablers such as numerical modeling, lubrication and coolant technologies, surface technologies, rapid prototyping of materials, laser technologies etc. These technologies have been identified as critical technologies in the roadmaps of the Supporting Industries as well as the Industries of the Future. Energy savings of 250 trillion BTUs and 3500 ton pollutants are projected for the IOFs
Since the project did not receive full funding and the project was terminated on September 30, 2004, only Strategies #1, #4 and #5 were pursued. The details of research and implementation are included in Appendices.

3.0 RESEARCH AND WORK PLAN

3.1 Research Objectives

Objectives of the project are: thorough characterization of lubricants, die material and integration of test results into planning software tool. This will be achieved by carrying out the following tasks,

- Characterize several graphite and synthetic lubricants under a objective environment for applicability in forging conditions
- Develop a design and process selection tool to quickly help designers quickly evaluate designs and aid in selection of die materials, coatings and heat treatment
- Develop a knowledge based scheduling software that will prescribe or recommend appropriate intervals for die repair and will suggest appropriate ways of repairing dies

The first goal will be achieved by determination of the interface shear factor and friction coefficient of various water- and oil-based lubricants, and performing trials to establish the best methods for their application during hot forging. Key parameters such as lubricant type, dilution, quantity and frequency will be studied at different die and work-piece temperatures using the ring compression test and spike test for variety of lubricants like Acheson DeltaForge series, Fuchs LN series and synthetic graphite-free grades like Dylon.

Die material used in the study will constitute both commonly used die materials like H-13 and H-10 as well as exotic materials like Nickel Aluminide and Inconel 718. In conventional hot work steels, several working heat treatments (as measured by the insert hardness) will be evaluated. This would provide us a good understanding of heat treatment on wear characteristics of the tool steel. Some inserts will be sent out to have them nitrided, nitrocarburized and Toyota Diffusion Processed. These have been identified, as some of the more promising surface engineering approaches to increasing die life of precision forging dies. Variables that affect the performance of tools are geometry of specimen, process conditions including forging temperature, lubricant used etc. These will be varied to establish working domains for each of these material.

Four types of experiments are planned to screen, evaluate and optimize candidate coating, lubrication and die material systems (Figure 2):

- Ring tests for determining the lubricity of the selected workpiece-lubricant-coating system. Ring tests are well understood and standardized. However, they do not represent the large pressures and surface generation in a typical closed die operation. They will be used for calibrating and initial screening of the candidate systems for both hot and cold forgings. Standard 6:3:2 ring geometry will be used for this test. This test will not only provide the interface behavior but also the flow stress of the workpiece material.
- Spike tests combine the friction sensitivity of the ring tests and the cavity pressures of the closed die system. The friction condition at the interface determines the height of the spike. They will be used mainly for hot forging.
- The backward extrusion tests will primarily used to evaluate self-lubricating die coating systems for cold forging aluminum and steel. These tests, shown in Figure 16, create extreme surface generations. The wear at the punch shoulder in this test which

experiences high pressures and sliding speeds will be used to evaluate the abrasive wear characteristics of the coating-die material system.

- Closed cavity axisymmetric wear tests used to evaluate the abrasive wear, adhesive wear and fracture behavior of lubrication-coating-die material system. Die wear is measured at different locations. For example, abrasive wear in the flash region, plastic deformation in the plug and cracking in fillets.

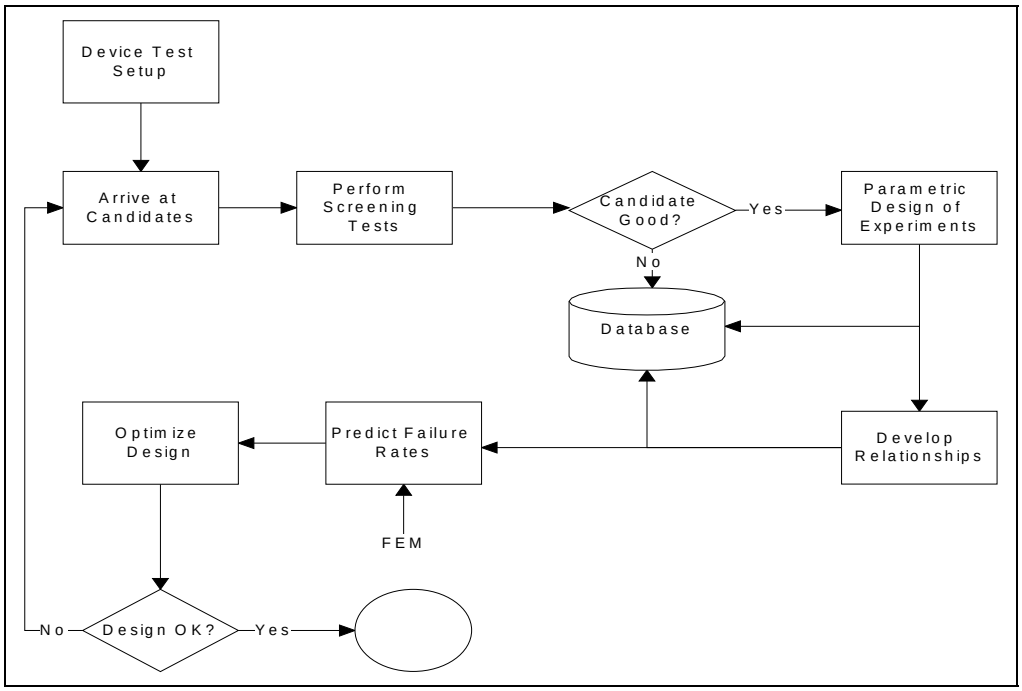

Figure 2: Outline of procedures and methodologies to be employed in the proposed research plan

3.2 Work Breakdown Structure

It is proposed to investigate this concept by using the following approach:

- Identify promising innovative and/or emerging coating and die materials candidates available in the materials field that can be used in the "concept die". Many of these candidates may not have fully matured but hold tremendous promise. Past experience of the OSU group with coating and surface treatments in other manufacturing processes and some applications in forging will be critical to this task. In addition two global leaders in coating technology have been added to the industrial team, Balzers and Ion Bond, to add the innovative and exploration focus.
- Establish program to screen, evaluate and optimize the material and design configurations

in the concept die. The important tasks in this step will be to

- Devise the standardized tests for observing and quantifying the lubrication and wear performance of this "concept die." These tests should be repeatable and represent forging process accurately. Typical tests such as ring test and spike test are discussed in later sections.
- Establish a world class forging cell that comprises a fully instrumented mechanical press with induction heating under environmental control, automatic lubrication spray and automatic loading and unloading system for workpiece and the die set.

Establish procedures and measures of die wear, energy usage and atmospheric contamination.
Establish benchmarks and comparative criteria
Perform extensive parametric studies using the Design of Experiment methodology to develop relationships between the measured wear, energy and pollution parameters to the process variables, die variables and the composite material configuration. Predict and optimize design configuration for the "concept die" through a knowledge base and FEM models. Test the optimized design at OSU and in industry (beta site evaluations).

3.3 Work Schedule (original)

The statement of work for the four years as originally planned is given below. The tasks were planned to enable parallel work to be performed by various teams. Tasks have been defined to indicate specific actions.

Year 2001- 2002: Phase I: Establishing the Program

Task 1: Installation of the "Forging Cell:"
Task 2: Benchmark surveys of Forging Industry for Energy Consumption and Lubricant Pollution
Task 3: Design the Experiments including Selecting the Process Parameters
Task 4: Establish Measures of Energy, Environment and Productivity
Task 5: Comprehensive Review of Opportunities in Die Materials, Coatings and Testing.

Year 2002- 2003: Phase II: Screening & Bench Mark Tests For Innovative Die Material & Coatings

Task 1: Bench Mark Tests with Conventional Die Materials and Lubricants: Ring Tests, Spike Forging Tests; Backward Extrusion tests and Closed Die Test
Task 2 Screening Tests with Innovative Die Materials and Conventional Lubricants: Ring Tests, Spike Forging Tests; Backward Extrusion tests and Closed Die Test
Task 3: Screening Tests with Innovative Die Materials and no Lubricants: Ring Tests, Spike Forging Tests; Backward Extrusion tests and Closed Die Test
Task 4: Develop a Knowledge Base on Lubrication and Wear of Conventional and Innovative Materials

Year 2003- 2004: Phase III: Select Candidates and Optimize the Composite System

Task 1: Select the best candidates from the ones tested in Phase II and design a composite die for OSU Closed Cavity Test Set Up.
Task 2: Conduct DOE on the Optimized die

Task 3: Based on DOE develop predictive models and use them to design dies for Industrial applications

Year 2004- 2005: Phase IV: Industrial Trials/ Calibrate and Verify

Task 1: Evaluate Optimal Design for Applications at Selected Industrial Sites
Task 2: Develop Predictive Maintenance Tool for Die Related Downtime
Task 3: Report Energy, Environmental and Cost Savings
Task 4: Verify Preventive Maintenance Models at Selected Industrial Sites

3.4 Work Schedule (modified)

Due to the truncated research program (basically 2.25 years instead of the original 4 years) and research funding many of these tasks could not be completed. The tasks completed were the following:

Year 2001- 2002: Phase I Establishing the Program (all tasks competed)

Task 1: Installation of the "Forging Cell:"
Task 2: Benchmark surveys of Forging Industry for Energy Consumption and Lubricant Pollution
Task 3: Design the Experiments including Selecting the Process Parameters
Task 4: Establish Measures of Energy, Environment and Productivity
Task 5: Comprehensive Review of Opportunities in Die Materials, Coatings and Testing.

Year 2002- 2003: Phase II: Screening & Bench Mark Tests

Task 1: Tests and procedures were developed for evaluating die materials for their tempering and wear characteristics under thermal fatigue loading during hot upsetting.
Task 2 Single droplet test and procedures were developed for evaluating current lubricants (water based graphite and synthetics for their spreading, dry-off and pollution characteristics.
Task 3: Lubricant spray tests were developed for heat transfer studies on hot die surfaces.
Task 4: Methods were developed for application of nickel-aluminide coatings using the LENS coating system.

Year 2003- 2004: Phase III: Select Candidates and Test in Industry

Task 1: Algorithm for die life estimation under cyclic thermo-mechanical loading was developed.
Task 2: Die life algorithm was calibrated under laboratory conditions and validated by tests at the production set up of participating industry (Sypris Corporation, Marion, OH)
Task 3: LENS deposited NiAlcoating was deposited and characterized for composition and hardness.
Task 4: Model based lubrication design was mainly evaluated in the laboratory environment..

Year 2004- 2005: Phase IV: Was not carried out (some industry tests were done in Phase III)

4.0 ACCOMPLISHMENTS

4.1 Project Accomplishments

The project received full funding support only for the fiscal years 2001 and 2002, and partial support for fiscal year 2003. The work plan and the achievements reflect this reduced support and modified work plan:

- With support from the Forging Industry Association, Forgers and suppliers of US forging Industry, have established CEFT - A Center for Excellence in Forging Technology at the Ohio State University
  - Conducted workshops and seminars attended by over 50 companies
  - Obtained 3 doctoral fellowships to perform research in the area of lubrication and die materials
  - Identified and formed focus groups that represent the several projects under CEFT
  - Established collaborations with the top industries in these areas, who will both help in developing the new technologies as well as commercialize the same.

- Acquired a complete forging cell (including a smaller 350 ton highly controllable hydraulic press and a 1300 ton mechanical press, a 250 KW induction heater and lubrication system) to perform large industrial-scale trials under controlled condition
  - Obtained equipment donations from Industries worth over half a million, state funds ($150k) to complement ITP funds towards purchase of equipment. A cost share larger than 1:1 was achieved through industry, State and OSU contributions for equipment purchase and installation at the Research Center.

    - A 1300 ton Mechanical Press. The press was donated by Sypris Technologies and refurbished by Erie Press Systems, Erie, PA. It was installed at the Ohio State University (OSU) Research Center in 2004. Details are presented in Figure 3 .
    - A 350 ton hydraulic press and forging simulator was especially built to OSU specifications for forging research by Danley Press, Cleveland, OH. This press was installed at OSU Research Center in late 2004. Details of the press including specifications are given in Figure 4.
    - An induction heater with the capability of heating 0.5 to 1.5 inch diameter billets to 2200F. This heater has 30 KW capacity on a 240V, 3 phase supply. It is water cooled at 8 GPM, with 30PSI air used primarily for operation of push cylinders.

  - The project team (Center for Excellence in Forging Technology) was also able to get a grant of $218,000 from the Forging Industry Educational and Research Foundation (FIERF) to support 3 graduate students for 3 years as Forging Fellows. The Graduate

School at OSU matched this grant by paying the tuition and fees for these graduate students.

Specifications for the Ajax 1300 ton Mechanical Press at OSU

Press Specs per Sypris

- Ajax Pitman Mechanical, Year 1950, Tonnage 1300 tons
- Weight 165,000 lbs, Motor: > 5HP, 1200 rpm, 93 Amps, Ram Cycle 70 SPM
- Die space: 44" X 33", Floor space: 11' X 9'4", Height: 16'3" (16' above ground)
- Stroke: 10", Wedge: 1 5/8"

Refurbishing (Rebuild in 2000, Refurbished in 2004(at Erie Press))

- Was used at Sypris technologies until 2000; two similar presses were sold by them for around $250,000 (as is).
- New crank, New Bushings/ Brass, Hydraulic kick, Ram checked
- $103,125 New Data Acquisition & PLC Control System
- $150,310 (Erie Press) repair including lube system, eccentric shafts, journals and pitman assembly, brake assembly, clutch assembly and thermocouple protection.
- Total refurbishing cost ($253,435.00).
- The press was inspected and run at Erie after refurbishing.

Figure 3: Photo and specifications for the 1300 ton mechanical press installed at the Research Center at the Ohio State University

Specifications for the Danly/ Savage 350 ton Hydraulic Press at OSU

Press Specs

- 350 ton Savage Hydraulic Press
- Four column frame with minimum stiffness 8MN/m
- Weight 45,000 lbs, Electric Motor 150HP, 163 FLA, 3 phase, 460 V
- Water inlet and drain 1.25" diameter, temperature not to exceed 55F
- Die space: 44" X 33" (T-slotted), Floor space:15.5' X 15.5', Height: 13'
- Hydraulic fluid, 250-250 SUS, maximum viscosity 1000cSt, 440 gallon reservoir.
- 20" stroke, BDC controllable, position feedback, 5 MN load cell
- Bottom hydraulic kickout that is removable for extrusion experiments
- Velocity maximum 10"/s, velocity-stroke profile programmable
- Multi-stroke cycle 6 Secs between stroke; safety interlock
- Motion control and data acquisition system

Cost of Press Built (2004) by Danly/ Savage

- $445,000.(Danly) + $4,000 (LabView software)

Figure 4*: *Photo and specifications for the 350 ton hydraulic forging press and simulator.

- State of the art reviews
    - Completed benchmark survey of forging industry
    - Established measures of energy and productivity usage
    - Completed comprehensive review of opportunities in lubricants and die materials, coatings and testing procedures for evaluating tribological performance

- Screening and benchmark tests
    - Performed several screening tests for lubricants (graphitic and non-graphitic)
    - Tested feasibility of several coatings (Nickel Aluminide, DLC) on tool steel substrates
    - Designed and completed tests for evaluating die materials, coatings and heat treatments
    - Designed and build test setups for characterizing the heat transfer and lubricity of lubricants sprayed using various methods
- Investigation and Development of new technologies
    - Investigation of lubricants and lubrication systems (Appendix A)
    - Investigation of LENS deposited NiAl coatings for hot forging application (Appendix B)
- Software development
    - Completed material database to assist forgers in selection of tool materials
    - Completed preventive maintenance software to predict tool failure through "hybrid sensor" technology
    - Developed a software for calculating the thermal softening of hot forging die materials.

4.2 Patents, Publications, Presentations

Patents: None

Publications and Presentations

1. Babu, S. and Shivpuri, R., A Test For Valuating Steels And Surface Coatings For Forging Dies, 23rd Forging Industry Technical Conference: 2001--A Shape Odyssey, Reno, Nevada, AZ, 2001.
2. Babu, S. and Shivpuri, R., Characterization and Measurement Of Failure Of Next Generation Material Forging Dies, 24th Forging Industry Technical Conference, Cleveland, Ohio, 2002.
3. Shivpuri, R., Agarwal, K., Mathur, D., Lembo, J. and Harris, W., "Forging of Aluminum Helicopter Parts using Rapidly Prototyped Dies," Aero Mat 2003, Dayton, OH, June 9-12, 2003.
4. Shivpuri, R., "An Integrated Approach to Forging and Forging Die Design: RAPIDTOOL," Forging Defense Manufacturing Consortium, Technology Summit, Cleveland, OH, June 24-25, 2003.
5. Shivpuri, R., "Roadmap to Increased Competitiveness of U.S. Forging Industry," Forging Industry Technology Roadmap Workshop, FIERF, Ann Arbor, MI, October 14, 2003.

6. Wu, Y. and Shivpuri, R., Opti-Lube Report - Review of lubricants in hot forging, Center for Excellence in Forging Technology, The Ohio State University, May 2004
7. Babu, S. and Shivpuri, R. Precision hot spur gear forging, Center for Excellence in Forging Technology, The Ohio State University, August 2004
8. Sheng, Z.Q. Shivpuri, R., Control of Metal Forming Equipment for Improved Part Quality, 25th Forging Industry Technical Conference, Detroit, April 19-21, 2004
9. Shivpuri, R., Innovative Die Material and Lubrication Strategies, 25th Forging Industry Technical Conference, April 2004
10. Shivpuri, R, Babu, S., Wu, Y. and Kini, S., "Investigation of Advanced Die Materials and Gradient Surfaces for Forming Tools," Invited Presentation, 8th International Conference on the Technology of Plasticity (ICTP), Verona, Italy, October, 2005.
11. Yang, L., Liu, C. and Shivpuri, R., "Comprehensive Approach to Film Formation, Pollution and Heat Transfer in Hot Die Lubrication," Keynote Paper, 8th International Conference on the Technology of Plasticity (ICTP), Verona, Italy, October, 2005.
12. Shivpuri, R., "Advances in the Numerical Modeling of Forging Processes," Keynote Presentation, 2006 AMPT, Int. Conf. on Advances in Materials and Processing Technologies, Las Vegas, July 30- Aug 3, 2006.
13. Shivpuri, R. , X. Cheng, K. Agarwal and S. Babu, "Evaluation of 3D Printing for Dies in Low Volume Forging of 7075 Aluminum Helicopter Parts," Accepted for Publication, Rapid Prototyping Journal, 2005.
14. Yang, L, Liu, C. and Shivpuri, R., "Physiothermodynamics of Lubricant Deposition on Hot Surfaces," Annals of the CIRP, Vol 54/1 (2005) 253-256.
15. Shivpuri, R., Agarwal, K., Cheng, X. and Babu, S., "An Evaluation of the RCC process for Aluminum Forging Dies," Rapid Prototyping Journal, Vol. 11, Number 5 (2005), 272-277.
16. Yang, L. and Shivpuri, R., "An Isothermal Finite Difference Model for Droplet Spread in the Spraying of Hot Die Surfaces with Water Based Graphite Surfaces," Accepted for publication in ASME Transactions, Journal of Manufacturing Engineering and Science, 2006.
17. Yang, L. and Shivpuri, R., "Spreading Behavior of Water based Graphite Lubricants on Hot Die Surfaces," Annals of the CIRP, Vol. 55/1, pp 299-302, 2006.
18. Yang, L. and Shivpuri, R., "A Water Evaporation based Model for Lubricant Dryoff on Die Surfaces Heated beyond the Leidenfrost Point," Submitted for publication in ASME Transactions, Journal of Manufacturing Engineering and Science, August 2006.
19. Shivpuri, R., Wu, Y., Farson, D, Choi, H., Laser Texturing Die Surfaces for Reduced Interface Friction in Cold Deformation of Aluminum Alloys, Submitted to the Annals of the CIRP, Vol 56/1, 2007.

5.0 CONCLUSIONS AND RECOMMENDATIONS

5.1 Conclusions

Though the research program was severely restricted and truncated due to the lack of support from DOE for the last two years of the project (FY 2003 and 2004), major findings and accomplishments were:

- A LENS (Laser Enhanced Net Shaping) based technique using Nickel and Aluminum powder was as a cost effective means for depositing Nickel Aluminide thin coating on H-13 hot working steel. Hardness and compositional analysis showed that good metallurgical bond with gradient composition was established between the coating and the steels substrate.
- A thermal softening algorithm was developed that takes into account tempering (loss of hot hardness) of the die steels due thermal cycling during the forging process. This algorithm was validated in industrial experiments and proved to be fairly accurate in predicting die wear.
- An experimental set-up and procedure was developed for evaluating tempering behavior of die steels under cyclic thermal fatigue and softening. In this set up several die materials can be tested simultaneously, thus providing for paired comparisons and quick screening.
- Theoretical models for lubricant spread, dry-off and break-up were developed using single droplet experiments. These models were validated by controlled experiments.
- An approach based on Sauder Mean Diameter was developed to relate the single droplet experiments to multi-droplet lubricant sprays. This approach can be used to optimize the design of lubricant spray systems.

5.2 Recommendations

Based on the innovative die materials and lubricants research the following is recommended:

- The LENS based and other powder based deposition technologies (such as HVOF) be widely used to treat forging dies before they are put in service. DOE together with the Forging and Forming Industry should start a program for these innovative hard facing and coating technologies.
- The tempering based die life estimation and optimization algorithm and the experimental procedures should be incorporated into software that can be used in industry to optimize die materials and processing conditions.
- Models for lubricant evaluation (single droplet) and spray optimization techniques have great potential for reducing the use of lubricants and their effect on the environment. They should be commercialized with DOE support and with the cooperation of participating lubrication suppliers.

APPENDIX - A

HARD WEAR RESISTANT COATING USING LASER ENHANCED NET SHAPING (LENS) TECHNOLOGY

A.1 Introduction to LENS

To understanding the impact of various factors on the properties of the coating, a process model based on underlying physics is necessary. LENS based deposition process can be classified into 4 stages:

- Stage 1. Powder travel from the nozzle to the substrate surface: During this time period, the powder is heated continuously.
- Stage 2. Melting of the substrate: Incident laser heats the surface and melts the skin. There is a possibility of plasma formation that will affect the flow of powder.
- Stage 3. Mixing of semi-heated powder: During this stage, solid or semi-solid powder material splashes on the heated substrate and mixes with the substrate forming a melt pool. The melt pool is subjected to further heating by the laser beam. In some cases, exothermic energy may be released by the powder that will also heat the pool.
- Stage 4. Solidification of the melt pool after it has left the laser zone: The last phase occurs when the table moves away from the beam and energy flow into melt pool stops. Melt pool created in the previous stage solidifies rapidly in the wake of the laser beam path forming a dense adherent layer on top of the substrate.

To understand the effects the control variables will have on the properties of the ensuing coating, underlying physics of the formation needs to be understood. The primary physical phenomena involved in the laser deposition process are: Heat transfer to powder, Trajectory, Plasma formation, Laser heating of substrate, Impact of heated powder on substrate and splat formation, Chemical energy in mixing, Physical mixing of semi-solid powder and substrate (convection) and Heat transfer to substrate mass Solidification.

A.2 Prior Modeling Efforts

Several researchers have either modeled Laser Engineered Net Shaping process or similar processes or have used modeling techniques that can be used in modeling LENS process. These involve the field of physics of materials, thermal analysis, fluid flow and material science. The following section sums up the various work found in the literature in modeling of the 4 stages.

A.2.1 Stage 1: Powder free-fall in laser zone

During this stage the particles fall through the laser focal area and are subjected to heating. Heat infused into the powder depends on the time it spends in the laser zone, laser power and the heat absorption. Also, it depends on the size and shape of the powder. The time powder spends in the laser focus depends on the location of the nozzle with respect to the effect of control variables on

powder pretreatment.

Several researchers have attempted to predict the extent deposited powder heats when it is falling in the laser zone. LENS parameters that influence the powder temperature a distribution are Location and geometry of the nozzle, Flow rate of the powder, Heat absorptivity of the powder, Size distribution of the powder, Laser power, beam diameter and focus Argon flow rate.

Time the powder spends in the laser zone depends on the powder velocity, distance and orientation of the nozzle, size of the powder, back pressure due to plasma and recoil of shroud gas. The heat absorption depends on the absorptivity (a function of laser wavelength and temperature), powder surface to volume ratio. The absorptivity of the powder is temperature dependent and rises with increasing temperature. It also increases with lower wavelengths and hence the higher efficiencies in use Nd-Yag as against Co2 laser.

Fisher and others [Fischer, et al., 2002, Fischer, et al., 2003] have performed numerical simulations in sintering of Ti powder using SLS process factoring in absorption of radiation by metallic powder, plasma formation (function of average laser power, pulsing rate, beam radius) and resulting recoil pressure, and the thermal properties of powder and the binder medium. Numerical simulations were done develop process maps that would help in establishing laser pulse frequency and laser power. Approximate physics-based and empirical-models have been used for this purpose, to relate the laser setting and powder size to temperature distribution in the substrate, plasma recoil pressure and subsequent surface profile. The results have been validated using sintering experiments on Ti powder performed using a 100W Nd-Yag pulsing laser with reasonable results.

Equations used in the model are

$$v_p = \frac{P_0}{\tau_p \pi r_b^2 I_p} \tag{A.1}$$

P_0 is the average power, τ_p is the pulse duration, r_b is the beam radius and I_p is the plasma threshold beyond which plasma can be expected,

$$I_p = 4x10^4 / \sqrt{\tau} \tag{A.2}$$

$$P_{rec} = .54\, p(T_s) \tag{A.3}$$

where P is the recoil pressure and $p(T_s)$ is the vapor pressure at temperature T_s

Maximum temperature at the surface of a powder is approximated by

$$\Delta T_{\max} = \frac{2AI_0}{k}\sqrt{\frac{k_{th}\tau_p}{\pi}} \tag{A.4}$$

where A is the absorptivity, k is the thermal conductivity, k_{th} is the heat diffusivity and I_0 is the intensity defined by

$$I_0 = \frac{P_0}{\pi r_b^{\,2} v_m \tau_p} \tag{A.5}$$

Yevko and others from University of Toronto [Yevko, et al., 1998] have modeled the temperature field in SLS process using FEM (IDEAS) to solve generalized heat transfer problem with prescribed boundary conditions. IDEAS allows laser power source to be modeled as a heat flux that is a function of time. Yevko defines heat load as a function of laser power and beam width and varies the load based on the scan speed. In this exercise, the density and specific heat of the powder were calculated based on law of mixture using properties of stainless steel and argon. The thermal conductivity was calculated based on the assumption that all the powder particles are spherical and compacted (Churchill's work).

$$K = 1 + \frac{3\phi}{1 - \phi - \frac{1.306\phi^{10/3}}{1 - .4072\phi^{7/3}} - .07296\phi^{14/3}} \tag{A.6}$$

where K is the conductivity, and ϕ is defined as

$$\phi = \frac{\frac{k_d}{k_c} - 1}{\frac{k_d}{k_c} + 2} \text{ x volume fraction of dispersed phase} \tag{A.7}$$

where k_c is the thermal conductivity of continuous argon phase k_d is the thermal conductivity of the dispersed phase.

Yevko's thermal simulations yielded temperature profiles that were used to calculate the clad width. The clad height was calculated based on increase in density because of associated melting and densification. It should be notes that this analysis assumes no plasma formation and that the molten powder is spherical in shape. The results of simulation was validated using measurements of weld shape performed using a 1kW Nd-YAG pulsing laser.

Grujicic and others [Miller, et al., 2001] have come up with a simple model for predicting the temperature of a single powder particle propelled through a laser focal zone. Using simple geometric assumptions, they calculate the time a particle spends in the laser t_r as

$$t_r = 2w_0 / v_p \sin(\theta) \tag{A.8}$$

where w_0 is the radius of the laser beam, v_p is the particle velocity and θ is the angle between the trajectory and the laser incident angle. The energy absorbed E is

$$E_p = \alpha(\frac{r_p}{w_0})^2 P_l t_r \tag{A.9}$$

where α is the energy absorption parameter, r_p is the particle radius and P_l is the laser power. The authors calculate the total energy required for melting of the powder by summing the energy required to raise the powder temperature to melting temperature and the energy needed to completely melt it. By incorporating empirical results by Keicher[Grujicic, et al., 2001], authors were able to constrain the problem so that the substrate did not melt. Keicher's study suggests that for Inconel 625, substrate melting does not take place if the laser irradiance is less than 1 W/m2. This can be represented in equation form as

$$I_1 = \frac{C_l P_l}{w_0^2} \tag{A.10}$$

This equation is applicable if the laser beam is focused at the surface. If it is focused at a distance h_0 above the surface,

$$I_1 = \frac{C_l P_l}{w_0 + h_0 \tan(\beta/2)^2} \tag{A.11}$$

The problem was solved as an optimization problem using MATLAB to maximize the powder size for complete in-flight melting.

Fu and others[Fu, et al., 2002] have attempted to calculate the laser beam power attenuation due to absorption of laser photons by the powder particles before it reaches the surface. Their model explains loss of power by laser by taking into account the time the powder particles spend in the laser beam focus, its size and number, its absorptivity and the powder delivery angle. They have focused their efforts on the temperature distribution of the powder particles because they believe that the primary driving force in pool motion in laser cladding is the temperature gradients in the powder fed.

Kathuria and others [Kathuria, 1997] found that the interaction time of laser (Figure A1) with the powder along with the cooling rates is critical in determining the microstructure of the clad layer. They found that the longer the interaction time, the mushier the microstructure is.

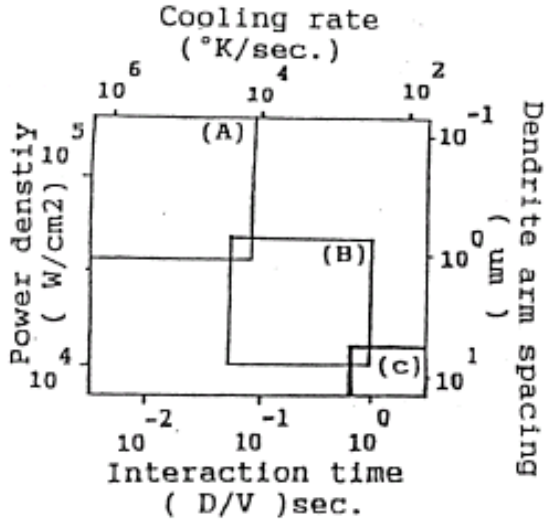

Figure A. 1: Microstructure v/s processing conditions for laser cladding (D = beam diameter in mm, V is the table speed in mm/s)[Kathuria, 1997]

A.2.2. Stage 2: Melting of Substrate and bead formation

Typically, in LENS, the laser beam is focused at the surface. A fraction of the radiant energy goes into melting of the surface and the remaining energy is used to preheat the powder that falls through the focal region. It is believed that almost no melting of powder occurs during this phase. The incident laser beam creates a molten pool of metal on the substrate which captures the feed powder. The pool width could range anywhere from ½ time to 5 times the beam diameter[Lewis and Schlienger, 2000]. The pool geometry and pool superheat dictate the efficiency of the particle catchment, build rate and the bead properties. Overheating increases dilution but flattens the bead by reducing the surface tension. Lewis and Schlienger [Lewis and Schlienger, 2000] indicate that the width of the weld pool created by the laser beam is primarily dependent on the surface tension of the molten material. Also, they indicate that the higher the heat sink is, the smaller is the melt pool width. They indicate that increasing laser power, lowering traverse speed and using thinner layers help achieve better finish. With substrate melting as the primary variable, Grujicic [Miller, et al., 2001] and others have solved a second order heat transfer differential equation to determine the extend of the substrate melting. In their analysis, they have considered the radiative and convective heat loss from the substrate surface and heat flux due to the laser beam, which they have defined as a function of the beam diameter, laser velocity and the power levels. They have defined the peak laser intensity I_0 of a gaussian beam as

$$I_0 = \frac{4P_l}{\sqrt{2}\pi w_0} \tag{A.12}$$

where P is the laser power level and w is the laser beam width.
Gaussian beam power level P(r) at any point r from the center beam is given by

$$P_r = \frac{P_0}{\pi {w_0}^2} \exp\left(-\frac{r^2}{w_0^2}\right) \tag{A.13}$$

For simplicity, molten material is not explicitly considered in their analysis. They solved the thermal conservation equation through finite difference approach to find size of the melt pool.

Vasinonta and others [Vasinonta, et al., 2000] used ABAQUS to model the thermal distribution assuming a point source approximation. They also neglected the effect of convection to air and convection within the melt pool, based on findings of Dobranich and others. They used non-dimensionalized variables (Rosenthal) to model and predict the temperature distribution and develop process maps for LENS. Using their model they predicted melt pool length and compared these to actual lengths that were measured on a LENS system. Their model predicted reasonably well, expected increase in melt pool lengths with increasing power and decreasing velocity. Their model also suggests that substrate preheating has a pronounced effect in reducing residual stress. Ki and Mazumder [Ki, et al., 2001] have modeled and solved the convective heat and mass transfer that occurs in laser material removal process using level set method, to compute the liquid-vapor interface. Their element based mass balance approach accounts for evaporation, melting of substrate and convective flow in the liquid phase. Heat balance in the element is achieved by balancing radiant and convective heat transfer, laser radiation, heat loss in vaporization and heat lost to substrate by conduction. It should be noted that their model is applicable to non-additive processes like laser melting or laser machining. Adapting their model to LENS creates another dimension when one attempts to incorporate powder heating, heat lost to powder and splatter. Although Fu and others [Fu, et al., 2002] have not modeled substrate

heating, they have modeled powder heating. The attenuated laser beam power density given by their calculations can now be used to model how the laser beam heats the substrate. To calculate powder catchment efficiency and clad height in a V-groove of a edge joint, Lin and others [Lin and Hwang, 2001] have performed simulations of the powder stream without laser radiation using fluid dynamic computational software, FLUENT which is based on a specific control-volume approach. Cladding experiments were performed for mild steel substrates with thickness of 2 and 6 mm under 1 kW CO2 laser irradiation for 304L stainless steel powder. They have decoupled flow and heat transfer to first obtain a powder flow distribution which was then transformed to clad height using heat transfer equations. Qian and others [Qian, et al., 1997] have studied the effect of the translation speed of the laser beam and the powder feed rate on the physical and microstructural qualities of the clad layer. This study attempts to experimentally arrive at optimal cladding parameters for maximum hardness. Li and others [Li and Ma, 1997] studied surface finish of blown powder cladding method theoretically and experimentally. Their approach to modeling surface finish was primarily geometry-based. Although the model does not help in understanding the effect of process parameters on surface finish, it gives us a general direction to any approach to improving the texture of clad surfaces. They found that the surface roughness (turbulence) of an overlapped cladding layer decreased with the increase of the overlapping ratio in an oscillating manner (Figure A3). They have modeled each clad layer as a parabolic approximation.

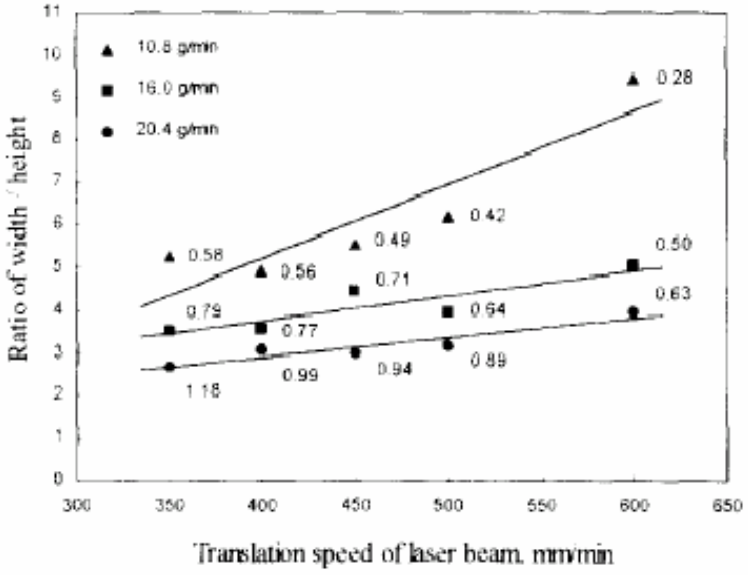

Figure A. 2: Effect of travel speed on aspect ratio of the clad bead [Qian, et al., 1997]

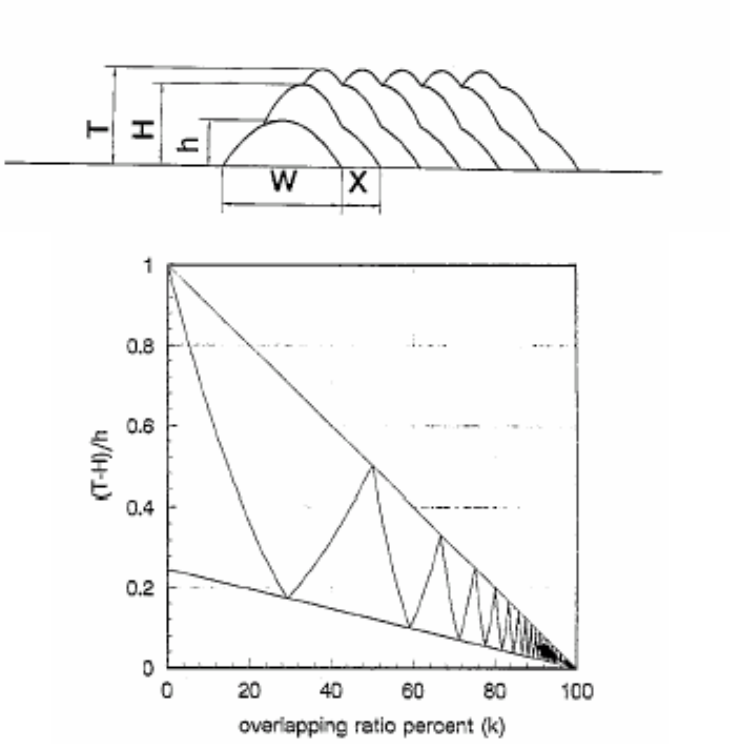

Figure A. 3: Variation of surface finish in powder-based cladding[Li and Ma, 1997]

Several empirical relationships have been suggested that relates the bead height and width to the process variables. Boddu and others[Boddu, et al., 2001] refer to work by Steen and others that relate bead width W to traverse speed v and laser sport size D.

$$W = D(1 - a\nu) \tag{A.14}$$

where a is a constant. Hu and others [Hu, et al., 1998] have also showed that the clad geometry can be approximated by a parabola and that the clad height H(t) can be approximated by

$$H = {}^{3A}\!/_{2W} \tag{A.15}$$

where A is the cross section area of the clad pass and W is the clad width. Hu and others performed several experiments that showed that the clad height increases with increasing powder flow rate, increasing power density or with decreasing traverse speeds.

The dilution of the clad layer into the substrate depends on several factors: the thermal conductivity of the substrate material, the initial temperature of the substrate, the reflectivity of the material, the powder flow rate, the interaction time of the powder in the beam and laser power [Sexton, et al., 2002]. Sexton reports that, for low laser power values, no fusion of the substrate occurred and the coating did not adhere to the substrate, while for larger power values the substrate melted increasingly as the power levels increased causing increased dilution. Ming and others[Ming, et al., 1998] have experimentally verified the effects of laser travel speed on dilution and bead aspect ratio predicted by other researchers. They found that the aspect ratio (width to height) increased with increasing travel speed (Figure A4) and powder feed rates. Also,

the dilution increased with increasing speeds and decreasing powder feed rates. It should be noted that the less the dilution, greater is the wear and oxidation resistance of the coating.

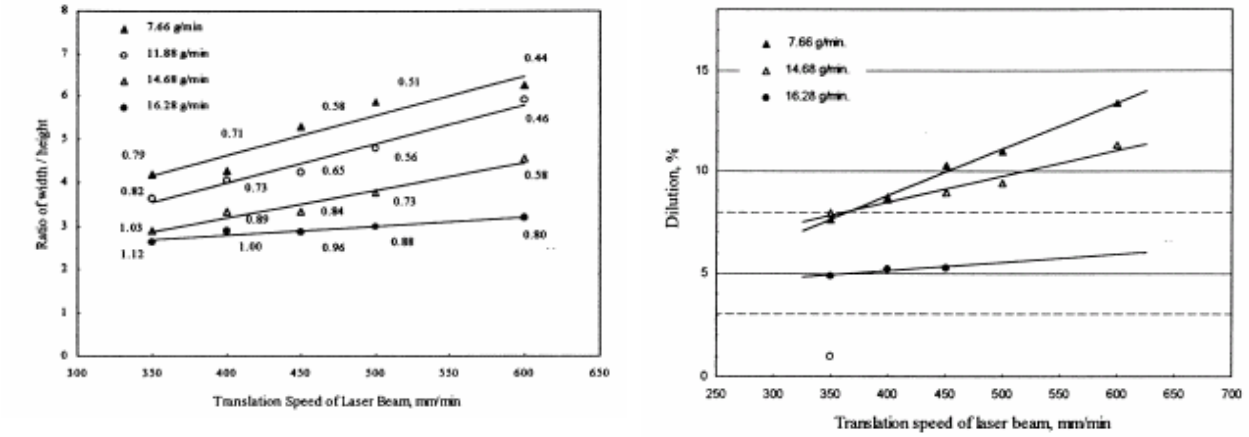

Figure A. 4: Effects of laser traverse speed on aspect ratio of bead and dilution [Ming, et al., 1998]

A.2.3. Stage 3: Mixing of Substrate and Powder

The third stage of the process is mixing of the substrate and the powder captured. The laser beam passing over the substrate or the prior deposit and melts a small region. The size and the superheat of the melt pool controls how effectively the powder fed is captured on to the surface. Higher the surface area, higher is the expected powder capture efficiency. Also, higher the superheat, higher is the ability to melt the powder particles and homogenize the weld matrix. Mahrle and Schmidt [Mahrle and Schmidt, 2002] recognized temperature as the key parameter in welding in affecting the weld properties and have modeled the laser weld process using finite element approach. They have used steady state models and non-dimensional numbers (Prandl, Peclet and Reynolds numbers) to predict flow induced heat transfer, melt temperature, velocities and weld bead shapes.

In some cases, enthalpy plays a big role in the thermal behavior and the ensuing structure. Dupont and others have worked on elemental blends of Nickel Aluminide. However, control of the thermal phenomena, the microstructure and porosity becomes more difficult because of the effect of the additional variable (the enthalpy of mixing). Liu and Dupont [Liu and Huang, 2003] investigated in-situ layering of Nickel Aluminide using Nickel and Aluminum powder and Ti-6-4 using elemental blends. Their study revealed that NiAl produced by this method was rather brittle and exhibited porosity that was attributable to the material as well as the high thermal stresses during the process. Similar work has been done by Fraser and others [Collins, et al., 2003], [Banerjee, et al., 2002, Collins, et al., 2003] that focused primarily on the reaction kinetics in creating Ti and Mo alloys (like Ti-6Al-4V) both from elemental blends as well as premixed alloys. Their study has revealed that it is possible to create alloys in-situ, however, control of compositions is extremely challenging. Kar and Mazumder [Kar and Mazumder, 1996] have analyzed the shape and morphology, of Laser CVD process and have presented a model that allows one to select the appropriate process parameters to obtain a good quality

film. They have found that an optimum condition is found to exist for depositing thin films by using the LCVD technique.

A.2.4. Stage 4: Solidification

The last phase of deposition process is solidification. In this phase, the molten substrate-powder mixture cools to form a rough layer. Modeling of the last phase involves heat transfer, microstructure change and diffusion. Researchers at Sandia Labs [Griffith, et al., 2000, J. A. Brooks, et al., 1999, Schlienger, et al., 1999] have tried to model the thermal effects of the LENS process on the microstructure of H-13 through application of the thermal histories extracted from experiments and phenomenological models of hardening process. They have shown that microstructure of the weld area as well as secondary hardening of the substrate close to the weld can be controlled through the use of appropriate table speeds, power levels and hatch spacing. They found that the peak temperature is the most critical process variable that controls the hardness of the substrate.

A.3 Numerical Model Development

For success of coatings and surface engineered dies, properties that are most critical are the wear, oxidation and thermal fatigue resistance of the clad layer, the adhesion of the clad layer to the substrate and the geometrical integrity of the weld. Local temperatures, weld pool shape, depth of melting and the powder feed rates have the biggest impact on these parameters. Process models created need to address the physical phenomena that affect these. Also, model created should have a way to relate these variables to the control variables (laser power, table speed, laser path, powder size and laser beam diameter), so that the tool developed can be used for design of the process. One approach to modeling these phenomena is through finite element codes. FEM is a robust approach that allows one to model non-linear processes more accurately, taking into account irregular geometries, nonlinear material properties and coupled phenomena. Also, FEM allows one to extract transient thermal and flow behavior, keys to predicting weld properties. For this application, it has been well documented that flow within the melt pool has only a minor effect on the process variables that are of interest. With this assumption, a numerical model of the LENS process has been developed using finite element code DEFORM-3D. For modeling purposes, the physics of the process has been split into 2 phases:

- Heating and melting of the substrate by a laser beam
- Addition of heated powder to the melted weld pool

The first stage of the process is modeled as a heat transfer problem (Figure A5). The power and laser beam absorption were combined into a single simulation control variable called effective power (given by equation A.16). Effective power is defined as the product of the laser power incident on the substrate and the effective absorption of the substrate (A). Effective absorption, as defined above, is not only a function of the surface condition, but also a function of the power absorbed by the powder as it drops through the laser focus.

Heating of the substrate by the laser beam has been modeled using a heat transfer window that is exactly equal to the size of the laser beam.

$$P_e = A.P_l \qquad \text{(A.16)}$$

A preliminary simulation was conducted assuming a rectangular substrate of size 2”x2”x1”. The simulation revealed that the temperatures outside a region of approximately 1” were almost room temperature. Based on the temperature profile obtained from the simulation run, subsequent runs were modeled based on a smaller specimen geometry This allows us to refine the mesh size even more for the same computation times. Also, for reducing computation, one half of the substrate has been modeled.

To develop the model, the following assumptions were made:

- Although the beam power intensity is gaussian in nature, it has been modeled as a beam with uniform power intensity.
- The melt pool and the unmelted substrate is being modeled as a single phase. Thermo-physical properties of melt pool (thermal conductivity, specific heat etc.) has been incorporated in to the model as a temperature depended property
- Effects of convection induced by surface tension, non-uniform densities etc. on local temperature distribution is neglected

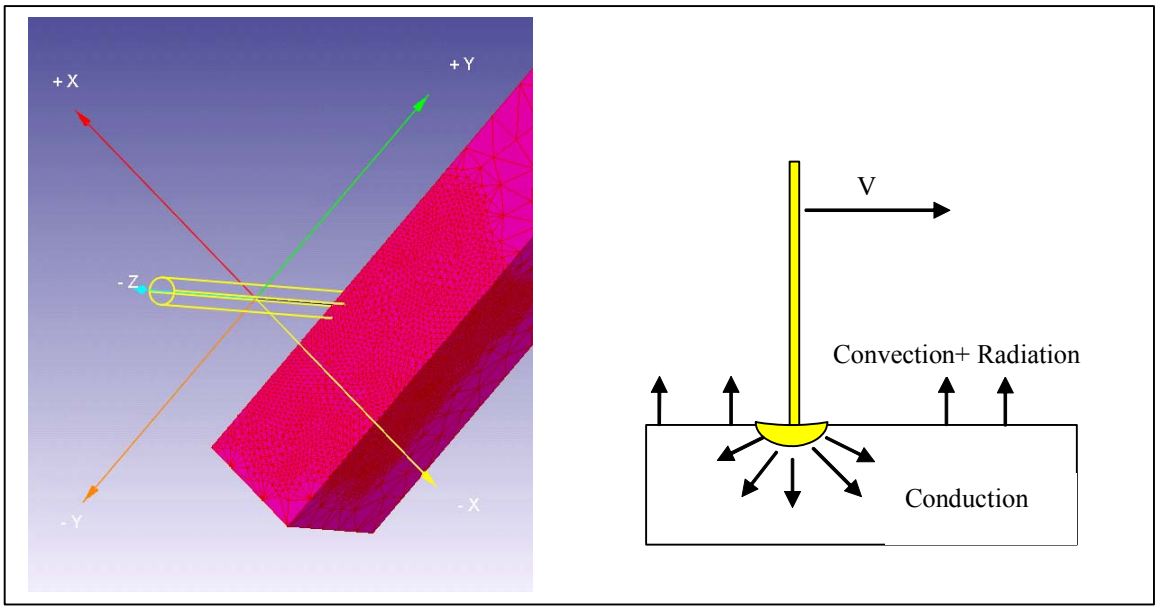

Figure A. 5: Laser beam representation and thermal boundary condition modeled in FEM

A.4 Parametric Numerical Study of LENS Process

To study the effect of the different process variables on the characteristics of the weld bead (width and depth of the weld pool, superheat), several numerical simulations were completed using a 3D explicit FEM code, DEFORM-3D. The process of LENS was simulated as a purely

thermal phenomenon, to study the effect of the process variables on the bead width, bead depth and the post process cooling rates. Process variables that have reportedly large effect on these are the laser power, the powder absorption, table speed, the laser focus/beam diameter and the preheat of the substrate. These have a large effect on the dilution in the weld pool as well as the microstructure of the weldment. These 2 variables are the most critical aspects of the weldment that affects its thermal and mechanical properties. Microstructure with finer grain size results in a stronger structure. Low dilution in the weld pool will ensure the properties of the clad layer are close to the engineered composition. The process variables that were varied in the simulation were the absorbed power, the table speed and the laser beam diameter. Simulation matrix used in this study is shown in Table A.1.

ID	Elements	Nodes	V (mm/sec)	H #	Beam Dia.	Max h
1	55772	12182	12.5	1	1 mm	2109
2	55772	12182	12.5	2	1 mm	1054
3	55772	12182	12.5	3	1 mm	527
4	55772	12182	12.5	4	1 mm	791
5	55772	12182	4	3	1 mm	527*
6	55772	12182	8	3	1 mm	527
7	55772	12182	16	3	1 mm	527
8	55772	12182	20	3	1 mm	527
9	57614	12419	12.5	3	.4 mm	527*
10	55772	12182	12.5	5	.6 mm	1465
11	55772	12182	12.5	3	.8 mm	527
12	55772	12182	12.5	2	.7 mm	1054

Table A. 1: Simulation matrix used for modeling LENS process in DEFORM-3D

It should be noted that the absorbed power being modeled encompasses several phenomena: laser power, absorptions, powder size and emissivity of the powder and the time powder spends under the laser beam.

Simulation ID	Melt width	Melt Length	Melt Depth	Max Temp ° C
1	1.5704	2.9058	.746	5910*
2	1.3807	1.7864	.5209	4780*
3	.98063	1.0547	.2369	2550
4	1.1831	1.4315	.4044	3690
5				2290
6	1.0763	1.1358	.29517	2720
7	.9441	1.0343	.20493	2400
8	.8355	.915	.1631	2270
9	Did not melt substrate			1180
10	.7869	.8783	.2714	4220

11	.6478	.6560	.12545	2130
12	.823	.9138	.254	3620

* Not applicable, outside of property domain

Table A. 2: Simulated maximum melt pool superheat temperatures and melt pool sizes

Figure A.6. show typical plot obtained from the modeling run, showing the isotherms in the substrate. Assuming a liquidus temperature of 1470 °C, melt pool dimensions were calculated. Figure A.7 show the variation of temperature with time. Peak temperatures are seen at locations directly under the laser beam.

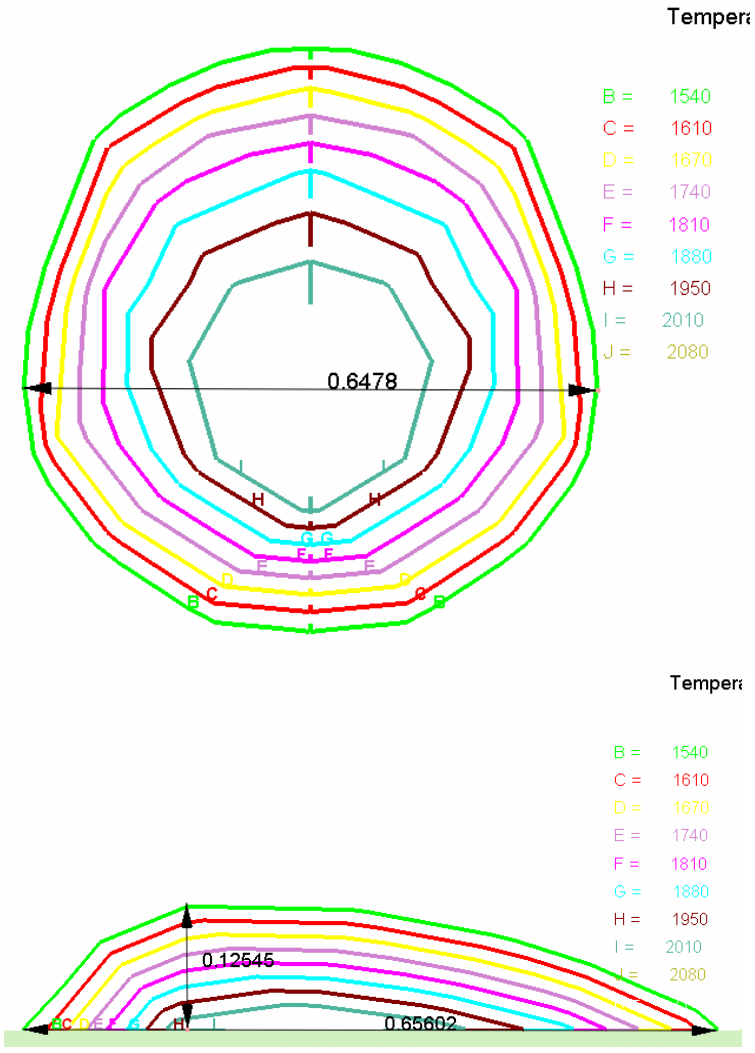

Figure A. 6: Typical thermal profile obtained from the simulation, used to obtain the length, width and height of the melt pool

Also, it was noted that the temperature at locations behind the laser beam was substantially higher than those ahead of the beam. Cooling rates at the wake of the melt pool was of the order of 1000-1500 °C/sec. Simulations were performed at boundary conditions outlined above and the dimensions of weld documented. Care was taken so that the element size was atleast $1/4^{th}$ of the laser beam diameter. The maximum temperature and the bead size were then plotted with respect to absorbed power, table speed and laser beam diameter. It was seen that the melt pool temperature, length of the melt pool and the depth increases with the power absorbed. Of the three parameters, the melt pool depth was least sensitive to the power, as indicated by the lower slope of the curve (Figure A.7).

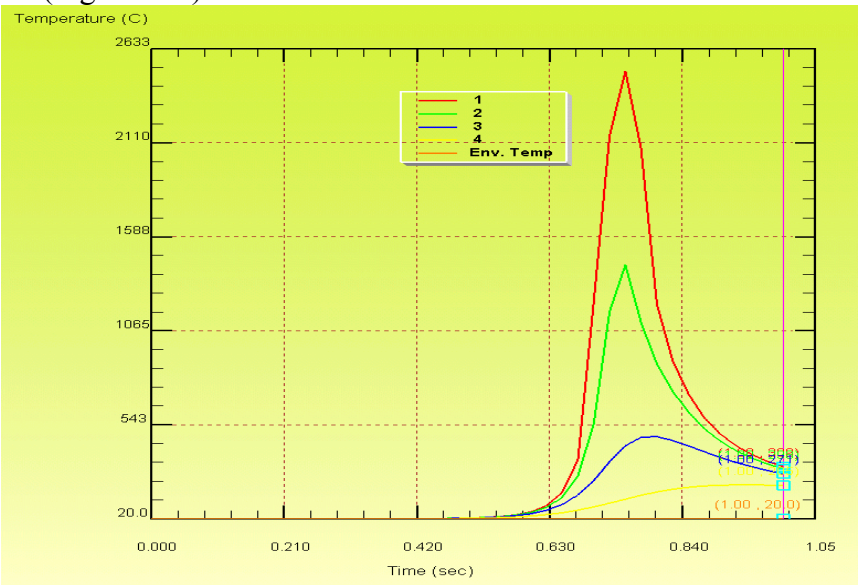

Figure A. 7: Typical thermal profile obtained from DEFORM-3D simulations of LENS process (temperature in °C)

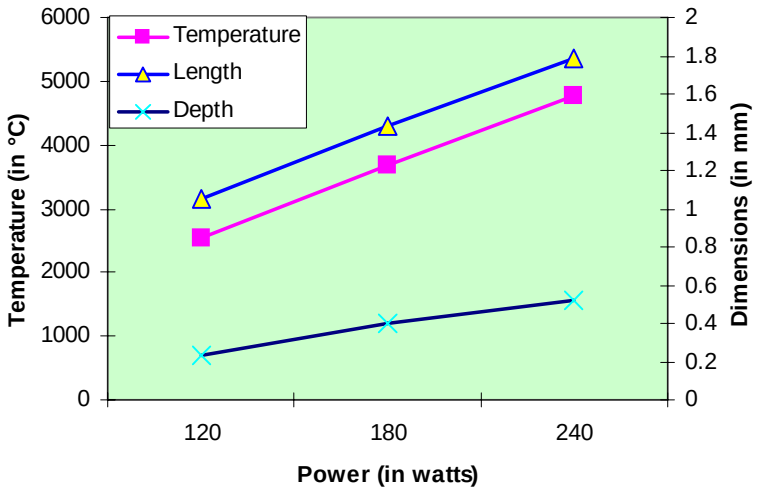

Figure A. 8: Simulated effect of absorbed power on weld superheat (table speed = 12.5 mm / sec, preheat temperature = 20 °C, H13 substrate, laser beam diameter = 1 mm)

All three plotted weld properties decreased with table speed (Figure A8). When the laser beam diameter was increased, for the same power, the superheat dropped. However, the dimensions of the weld bead increased. These trends confirm what has been reported in the literature. However, these need to be validated. Temperatures observed in these simulations are too high, indicating model deficiencies that do not take into account power lost to atmosphere, and power lost in heating the argon stream. Also, it may indicate that latent heat of melting needs to be modeled more accurately.

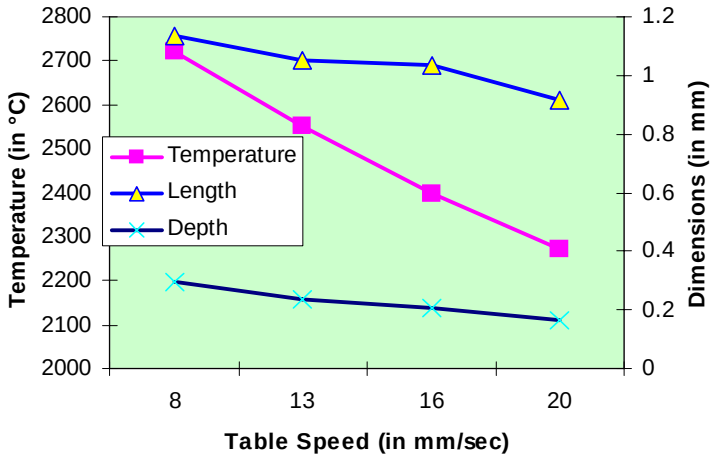

Figure A. 9: Simulated effect of table speed on melt pool superheat (effective power = 120 watts, preheat temperature = 20 °C, H13 substrate, laser beam diameter = 1 mm)

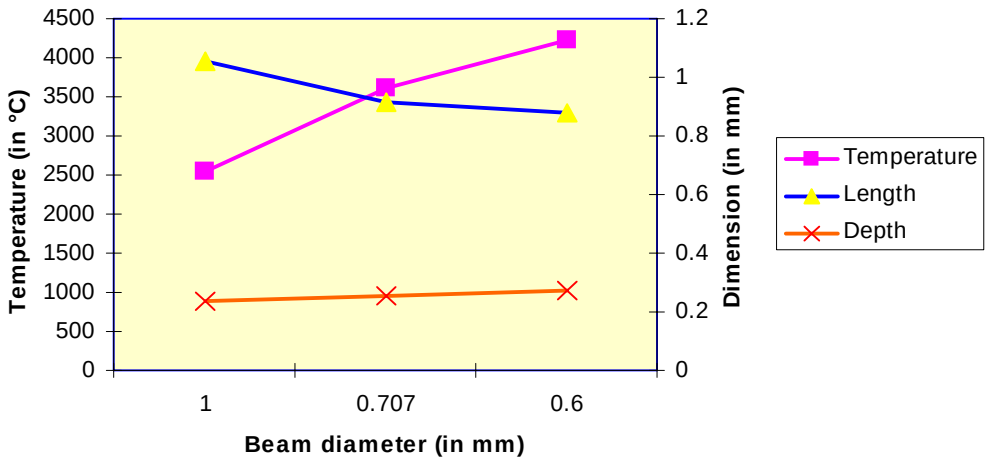

Figure A. 10: Simulated effect of beam diameter on melt pool superheat (effective absorbed power=120 watts, table speed = 12.5 mm/sec, preheat temperature =20 °C, H13 substrate)

A.5 Validation - Experimental Procedure

There are four primary components of the LENS™ assembly: the laser system, the powder delivery system, the controlled environment glove box, and the motion control system. A 760 W Nd:YAG laser, which produced near-infrared laser radiation at a wavelength of 1.064 mm, was used for all the depositions. The energy density used was in the range of 30,000 to 100,000 W/cm^2. The basic LENS™ system 750 used in the tests below consists of a high power Nd:YAG laser, a 3-axis computer controlled positioning system and multiple powder feed units. The positioning stages are mounted inside an argon-filled glove box (nominal oxygen level of 2-3 ppm), while the laser beam enters the glove box through a top mounted window. A powder delivery nozzle is used to inject a metal powder stream directly into the focused laser beam. The lens and powder delivery nozzle move as an integral unit in the z-axis, while the part, positioned under the laser beam, is transitioned in x and y.

Specifications of the LENS 750 system are as follows: Max. build Size: 300mm by 300mm by 300mm (12”x12”x12”); Preferred powder size: 75 microns (- 100 / +325 mesh); Hatch width: .015”, build layer thickness: .010”; Laser power: 270-370 W (1.064 MHz); Laser speed 10-50” / min; and Powder feed units: 2 buckets.

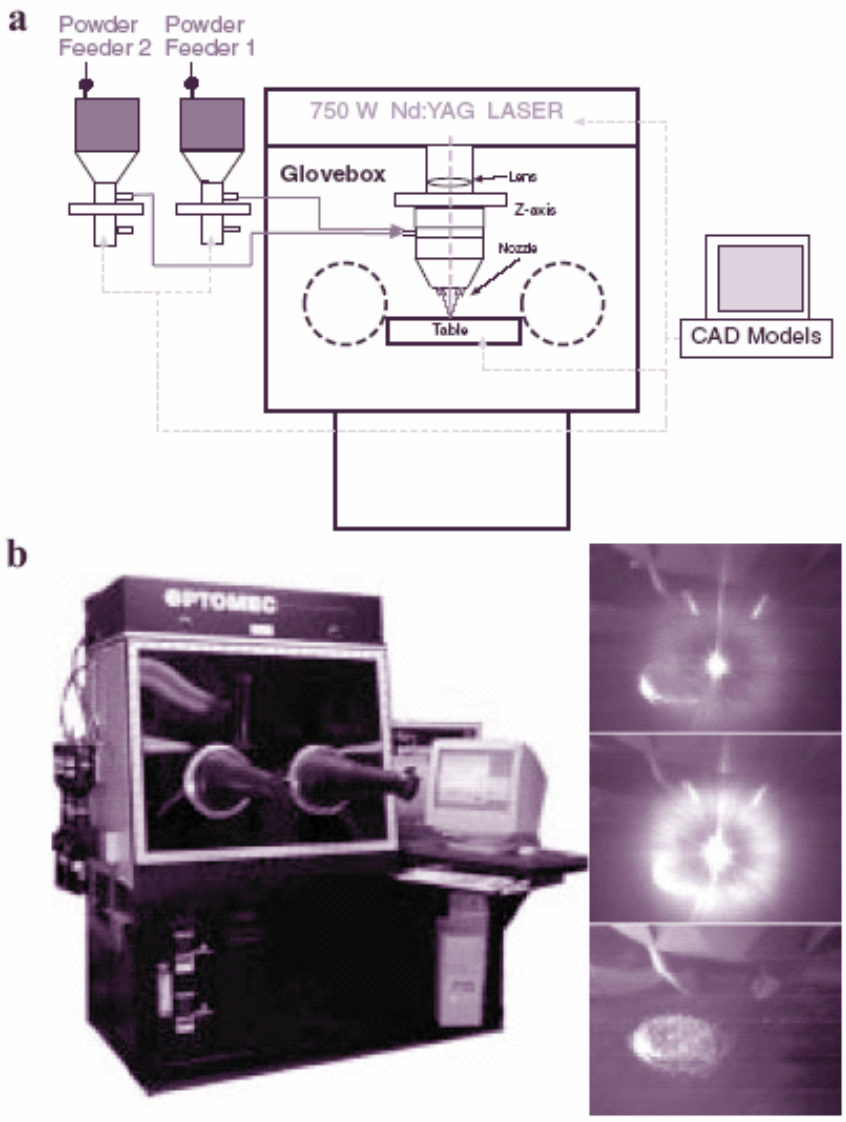

Figure A. 11: LENS system a) schematic and b. experimental facility at the Ohio State University [Banerjee, et al., 2002]

The various components of the LENS system (Figure A.10) are as follows:

- LENS 750 Glove Box and Dri-Train: Chamber where the deposition occurs. It includes the Nd:YAG laser, optics, the motion controlled stage, the anti-chamber, the powder feeders, and the atmosphere control systems

- LENS Workstation Control Console: LENS Workstation Control Console is the interactive computer system for the control of the CAD, Slice, and DMC files, the motion of the stage, and the atmosphere control of the Glove Box, Dri-Train, and Ante-Chamber.

US Laser Power Supply: The system is powered by US Laser Power Supply that supplies and controls the power to the Nd:YAG laser on the 750 Glove Box and Dri-Train assembly. The

system also supplies cooling water to the laser and the laser shutters. The laser used in this LENS system is a YAG-Nd solid-state type. These lasers have a yttrium-aluminum-garnet crystal (YAG) doped with neodymium (Nd). Instead of the usual 'flash-tube pumping', this new laser uses small semiconductor diode lasers to excite the neodymium. This allows much greater efficiency - thus smaller and more powerful lasers than before needed to melt
The table speed, the laser power and the hatch spacing the three primary controls affecting the morphology of the coating and the surface finish. Hence a series of coating trials were performed choosing 2 levels for each factor. It was felt that, increasing the powder feed will have same effect as reducing the travel speed. Hence it was not factored into the first series of experiments.

Several H-13 samples having identical geometry were machined. The samples were heat treated to 46-48 HRC. The head geometry is shown below. To eliminate surface condition from causing any variability, all samples were polished to similar roughness (~ 0.1 microns). A fixture was also fabricated to securely hold the samples at predetermined location. The fixture designed had several "pigeon-hole" type features that allowed the pins top be securely located on to the surface. The plate itself was mounted onto the LENS glove box for processing.

One of the powder reservoirs was loaded with Stellite's Nistelle N13Al (a nickel aluminide grade powder). Powder used was rated at -100/+270 Mesh. The substrate was not preheated. Background oxygen level was kept at 3-4 ppm and the oxygen level during deposition process and the Argon flow rate was kept at 6-8 l/min. Programmed layer thickness was set at 0.008". Powder density was measured to be approximately 7.3 gms/cc.

#	Laser speed (mm/min)	Current (amps)	Hatch Spacing	Powder flow rate	Ra (μm)	Power (watts)	Beam diameter
1	875	34	.010"	2.5 rpm	.1	310	1 mm
2	875	34	.010"	2.5 rpm	.1	310	1 mm
3	875	38	.010"	2.5 rpm	0	380	1 mm
4	500	34	.010"	2.5 rpm	.1	310	1 mm
5	500	38	.010"	2.5 rpm	.1	380	1 mm
6	500	34	.015"	2.5 rpm	.1	310	1 mm
7	500	38	.015"	2.5 rpm	0	380	1 mm
8	875	34	.015"	2.5 rpm	0	310	1 mm
9	875	38	.015	2.5 rpm	.1	380	1 mm

Table A. 3: Measured surface roughness and profile of LENS coated NiAl samples, powder size used was 100-270 ASTM mesh

A.6 Characterization and Results

A.6.1. Effect on surface finish

Surface finish and profile of the coated samples were checked using a Federal Surface Analyzer system 4000 (Figure A.11) – which is capable of measuring the roughness, waviness, form and

profile of surfaces. Table below (Table A.4) shows the surface finish of samples 2 -9 (Figure A.12-A.17). It was noted that the surface was extremely rough (with surface finish ranging from 5 – 15 microns). Surface roughness, however, smoothed out the gross waviness typical in these type of processes because of cyclical deposition of weld beads. For this reason, the surface profile might be a better indicator of the surface condition.

Figure A. 12: Federal Surface Analyzer used in the surface measurement

#	Speed (m/sec)	Power (Watts)	Hatch Spacing (inches)	Pt (μm)	Ra (μm)
2	0.875	310	0.01	101.4	7.3
3	0.875	380	0.01	102.6	10.5
4	0.5	310	0.01	185.5	14.6
5	0.5	380	0.01	183.9	9.7
6	0.5	310	0.015	150	13.3
7	0.5	380	0.015	186.5	14.3
8	0.875	310	0.015	72.9	8.5
9	0.875	380	0.015	98.5	7.2

Table A. 4: Measured surface roughness and profile of LENS coated NiAl samples

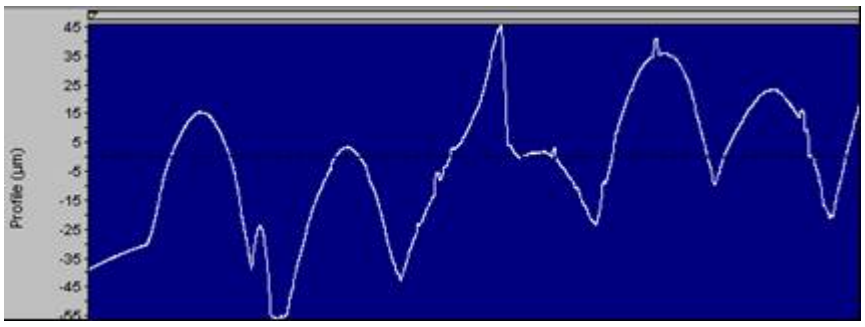

Figure A. 13: Profile – sample 2 (in microns)

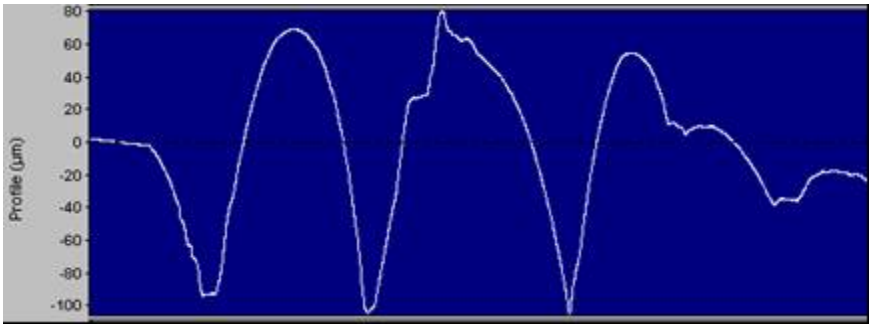

Figure A. 14: Profile – sample 4 (in microns)

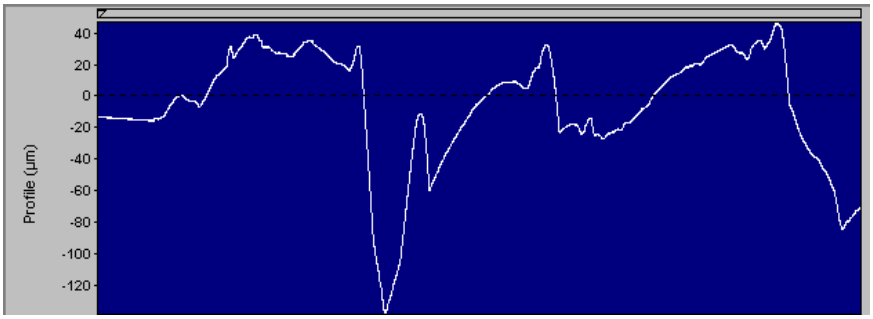

Figure A. 15: Profile – sample 5 (in microns)

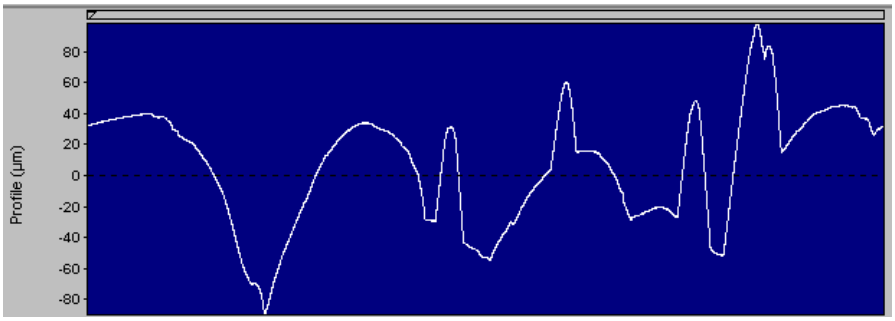

Figure A. 16: Profile – sample 7 (in microns)

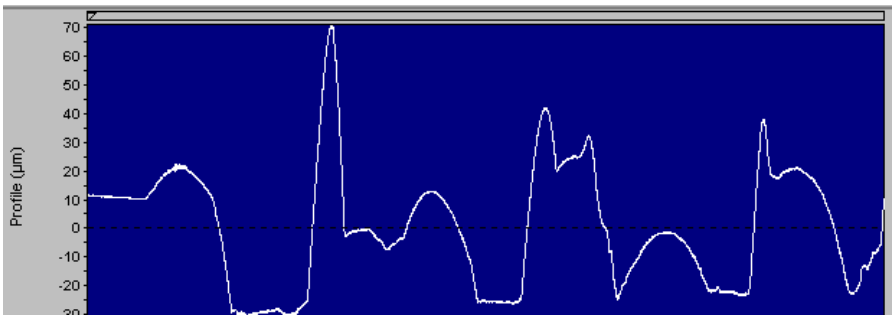

Figure A. 17: Profile – sample 8 (in microns)

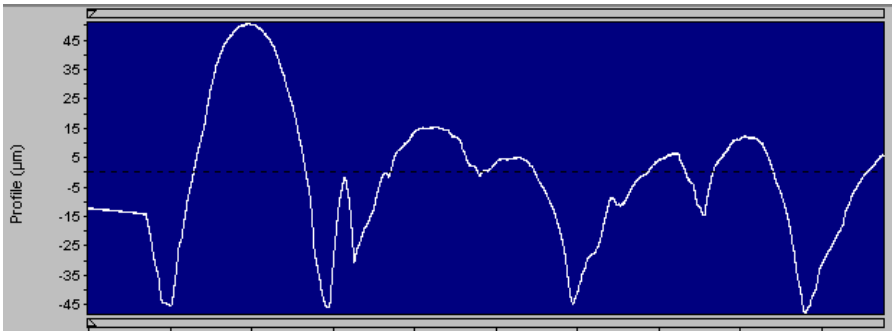

Figure A. 18: Profile – sample 9 (in microns)

The data obtained from the surface roughness measurements was regressed to obtain the following equation. The R-Square value obtained was .965 and the adjusted R-Square value was .94, indicating a good fit. All three variables have an equal effect on the surface profile.
Equation regressed:
Pt = 251.5-220.3 * TS (in m/sec) +.22* Power (watts) - 3275 * Hatch Spacing (in thousandths).

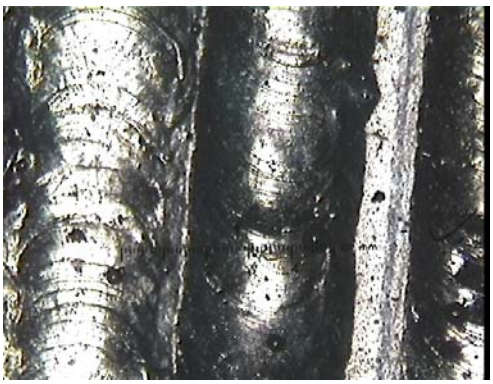

Sample 2

Sample 3

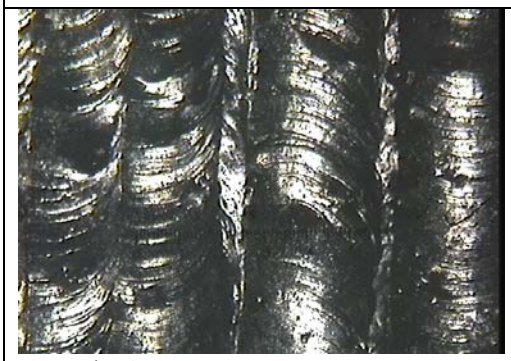

Sample 4

Sample 5

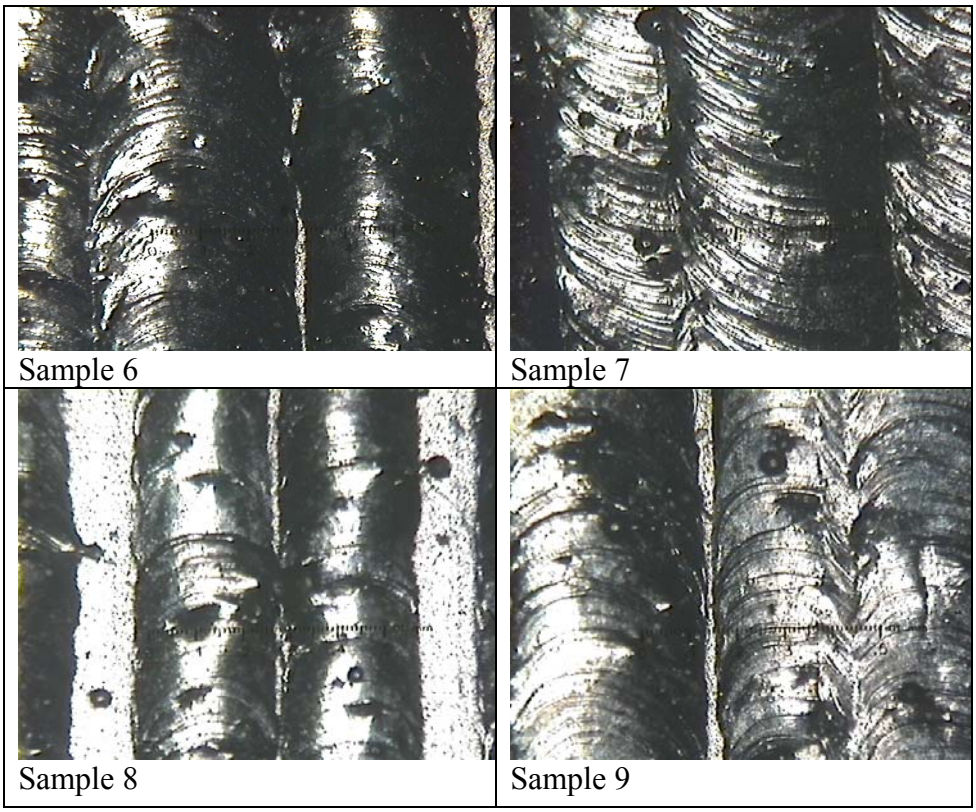

Figure A. 19: Optical images of coated surface at 50X for the samples 2-9. Note: samples 3, 5, 7, and 9 were coated at higher power levels, samples 6,7,8 and 9 have .015 HS

A.6.2. Coating Morphology

To see effect of the process on the microstructure and the interface, all samples were observed under a light microscope at 50X magnification. Figure A.19 shows the results of the optical microscopy. Figure A.20 shows that the bond obtained is relatively pore free, indicating excellent interface quality. Figure A.20 and Figure A.21 shows the SEM performed on sample 4, indicating presence of several partially melted nickel aluminide particles. Further analysis is required to relate the microstructure, the surface quality and bond interface to the process variables.

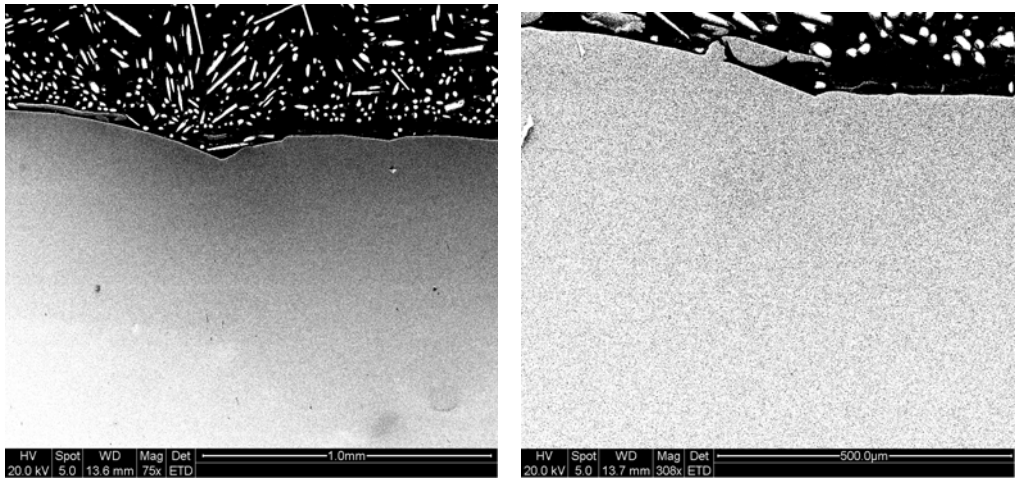

a) b)

Figure A. 20: SEM image showing cross section of sample 7, polished and bakelite mounted. Sample was not etched a) 75X b)300X

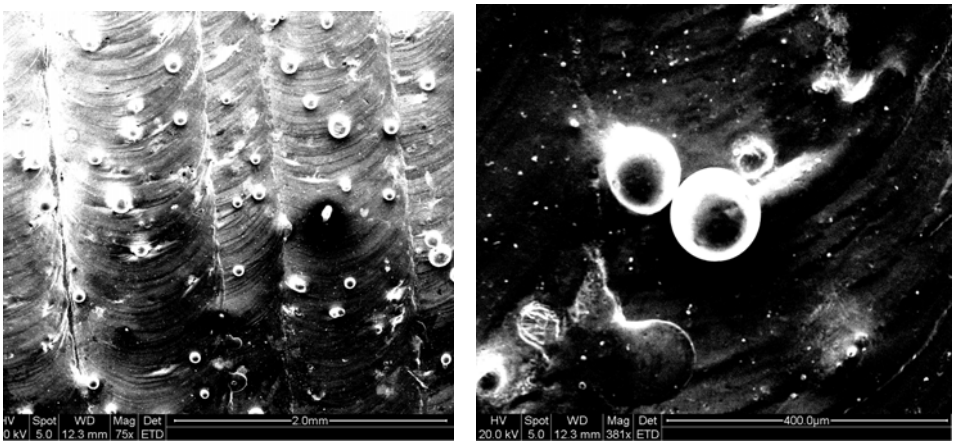

Figure A. 21: SEM image of surface of NiAl coating on H-13 substrate showing random appearance of partly melted powder. Image was taken at 75X and 381X

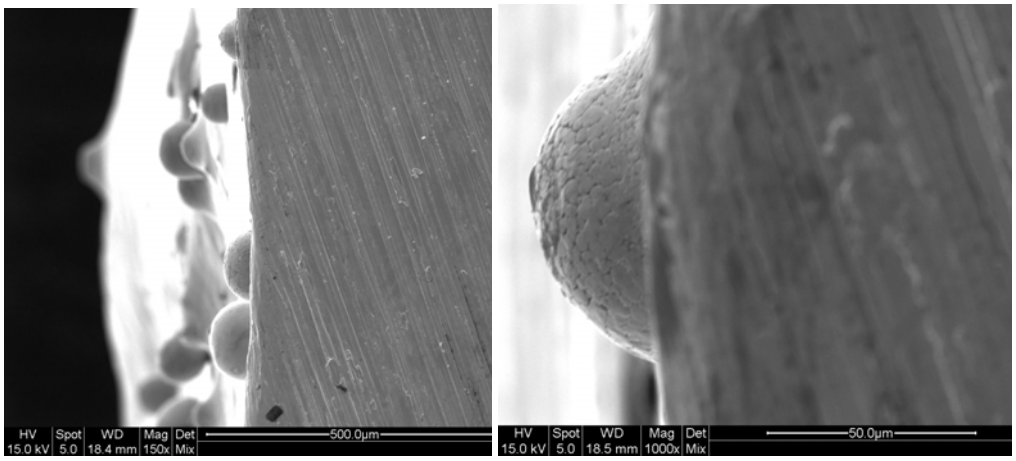

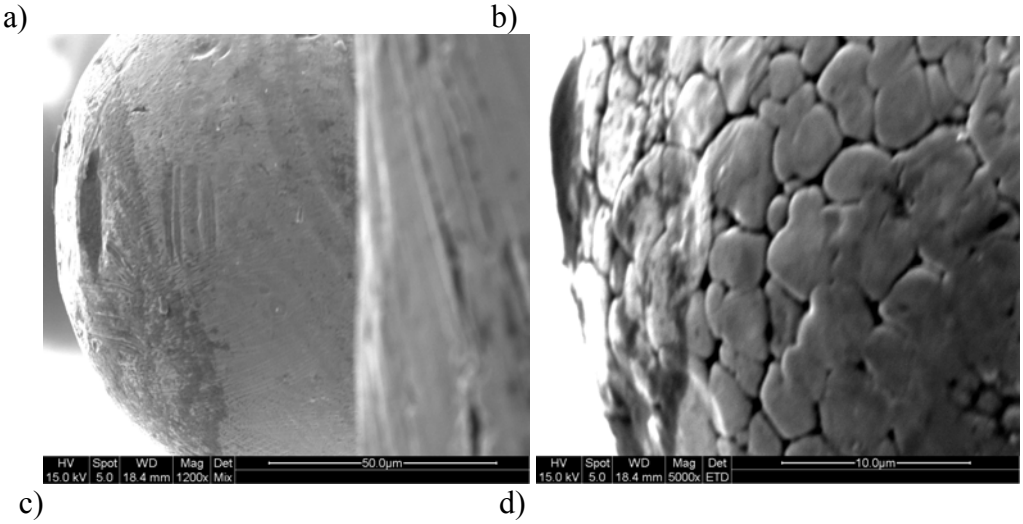

Figure A. 22: SEM Image of sample 7, showing NiAl powder at different stages of melting. Images are at a)150X b)1000X c) 1200X and b) 5000X

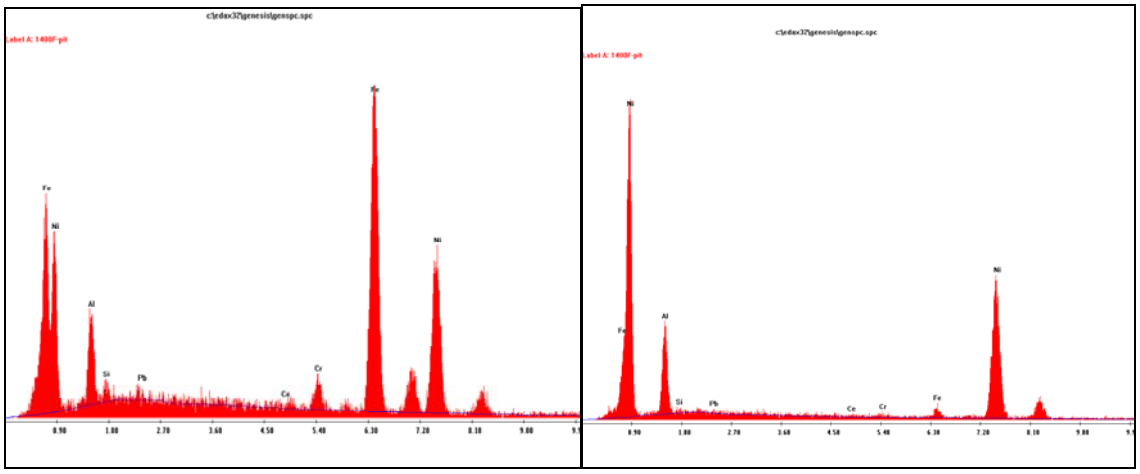

Figure A. 23: EDS analysis of a) Surface of sample 7 and b) NiAl powder

Table A.5 and Figure A.23 indicate the compositional gradient (sample 4) across the H13 /NiAl interface. SEM indicates that the interface is sharp possibly because the extremely high cooling rates. This may restrict the diffusion of Ni and Al into the steel substrate due to lack of time at higher temperatures where diffusion is easier. The dilution in the melt pool, correlated to the depth of melt pool and the table speed, is seen to be uniform in the clad region.

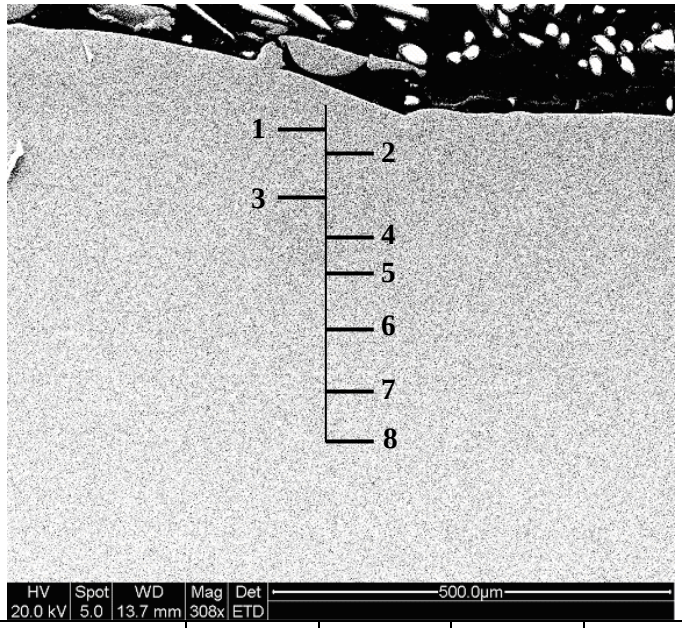

Index	Location from surface(in µm)	Fe (%)	Ni (%)	Al (%)	Pb (%)	Cr (%)
	Surface	46.31	35.86	7.2		
1	15	51.07	32.66	5.49	3.81	3.94
2	30	50.85	33.64	5.4	4.3	3.97
3	45	51.17	32.46	5.24	4.42	3.37
4	60	48.56	32.76	12.42	6.34	3.55
5	90	54.22	33.17	5.26	0	4.51
6	125	51.58	34.09	5.78	3.09	3.78
7	155	83.98	1.19	1.14	2.74	6.1
8	187	83.6	1.17	1	0	7

Table A. 5: Compositional gradient (wt %) from surface to the bulk of substrate, obtained through Energy Dispersive Spectrometric (EDS) analysis

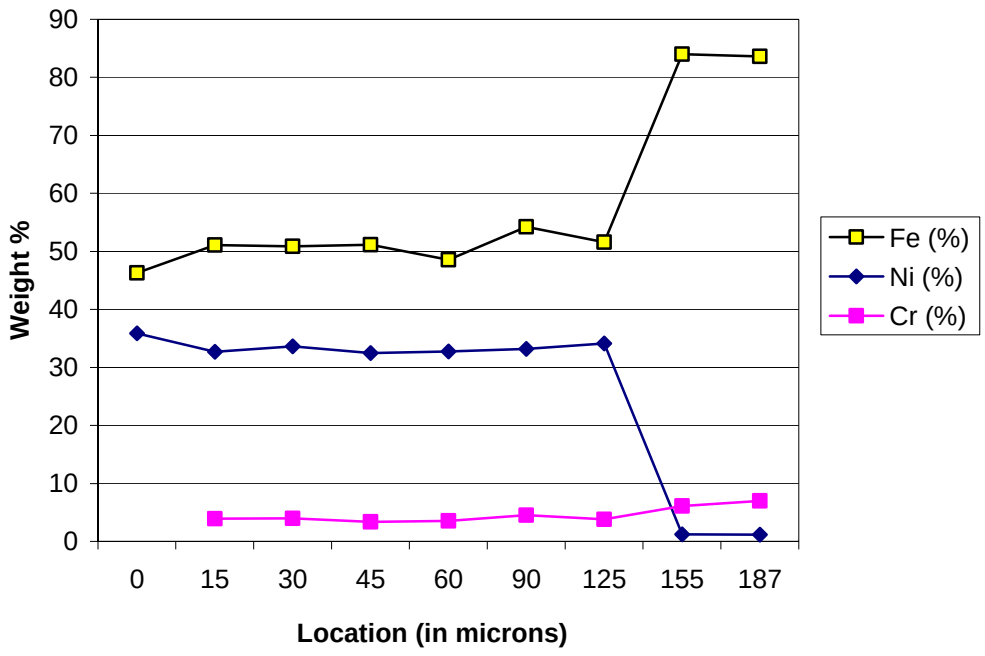

Figure A. 24: Variation of nickel, iron and chromium across the interface

APPENDIX - B

TEST FOR EVALUATING DIE STEELS AND ADVANCED MATERIALS FOR HOT FORGING APPLICATIONS

B.1 Introduction

Chapter 4 outlined the algorithm developed to predict the effects of the thermal cycling, sliding and pressures on the thermal softening of the die subsurface and wear. This algorithm outlines the various inputs to the model and the model outputs. Inputs to the thermal softening model are the tempering parameter of the tool material, the initial hardness and the process information. Inputs to the wear model are the material hardness (at room temperature and elevated temperatures) and the wear coefficient. Another product based input is the tolerances acceptable. The outputs are the tempered layer hardness profile, wear and tool life. The following section describes test setups that are used to validate the thermal softening and wear models.

B.2 Thermal Softening Test Setup

The thermal softening algorithm described in the previous chapter employs finite element approach to calculate effective tempering at various die locations based on tempering parameters similar to ones proposed by Hollomon and Jaffe and modified by Grange and Baughman. After the thermal profile is computed by the FEM engine, the developed module uses the time step information to calculate the *net tempering* of the various die location in the time step, using the relationship 4.3. During the simulation, these incremental "tempering times" are added up to calculate the net tempering time the different die locations are tempered for at a *reference temperature.* Based on the characteristics of the die material, these effective tempering times are translated to hardness loss. For most die materials, the tempering parameters outlined are published. For instance, for H13, the Grange Baughman tempering parameter is 16.44. If the tempering parameters are not easily available, one may be able to calculate these based on isothermal tempering data available as part of the material data sheets.

The thermal tempering model was validated using a test setup that recreates a intermittent thermal cycle seen in forging. During a hot forging cycle, the billet sits on the lower die for duration of 2-3 seconds. This is followed by the forging blow. During this period, the heat transfer into the dies goes up, because the tools come in intimate contact with the hot billet. During this phase the subsurface temperatures could reach in excess of 500 °C, while the bulk of the die remains at the steady state temperature of 200-300 °C. The surface and subsurface temperatures vary depending on the process, the type of press used, the billet temperature, the die bulk temperature and other factors like the presence of scale. Also, features in the die like sharp corners, gear and spline teeth and notches tend to over heat resulting in hot spots. If not careful, die surface temperatures may even exceed the steel transformation temperature. After forging, the part is ejected and removed and lubricant sprayed. Surface cools down sharply, while the substrate remains at a relatively high temperature (close to the steady state temperatures). The next billet is then placed on the bottom die and the cycle continues. Typical thermal cycle found in a hydraulic press and a hammer forging die is shown in Figure 5.1. The thermal spike

typically seen at the surface of these dies is illustrated in Figure 5.2.

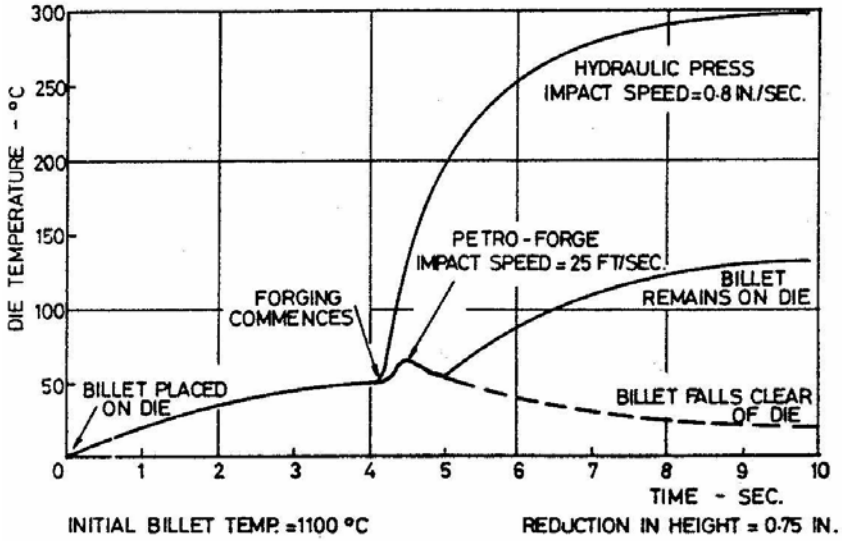

Figure B. 1: Typical thermal cycle in a hydraulic and hammer forging

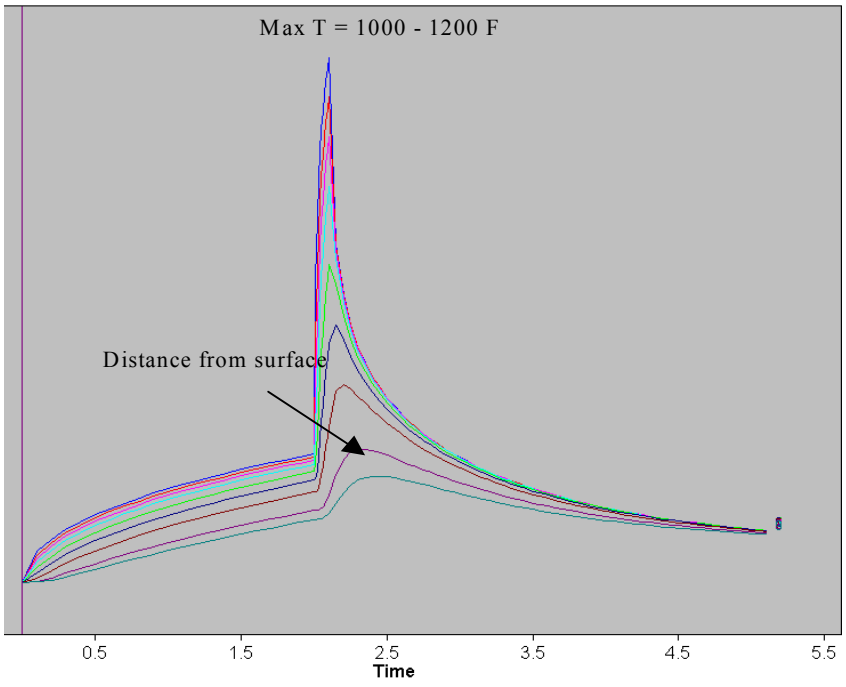

Figure B. 2: Temperatures spike seen at the die surface, in a typical hot forging die. Simulation was performed in DEFORM2D.

To study the effect of this thermal cycle on the subsurface hardness, a simple test setup was used (schematic shown in Figure 5.3). The test relied on cyclically contacting and retracting a die material test specimen onto and from a *hot billet.* By controlling the contact time, the pressures at

the interface and the time the sample cools, thermal cycles very close to a hydraulic press forging was achieved. For this test setup, the billet material was made of Waspaloy. This choice was made so that the billet material did not deform during the forging cycle. Also, this choice ensured that the billet does not oxidize over the duration of the test. These steps were intended to reduce the variability between stroke to stroke, to the maximum extent possible. The 4" diameter, 5" long waspaloy *billet* (Figure 5.4(a)) was heated to a steady state temperature of 1400 °F or 760 °C during the test. Nominal composition of Waspaloy is given in Table 5.1.

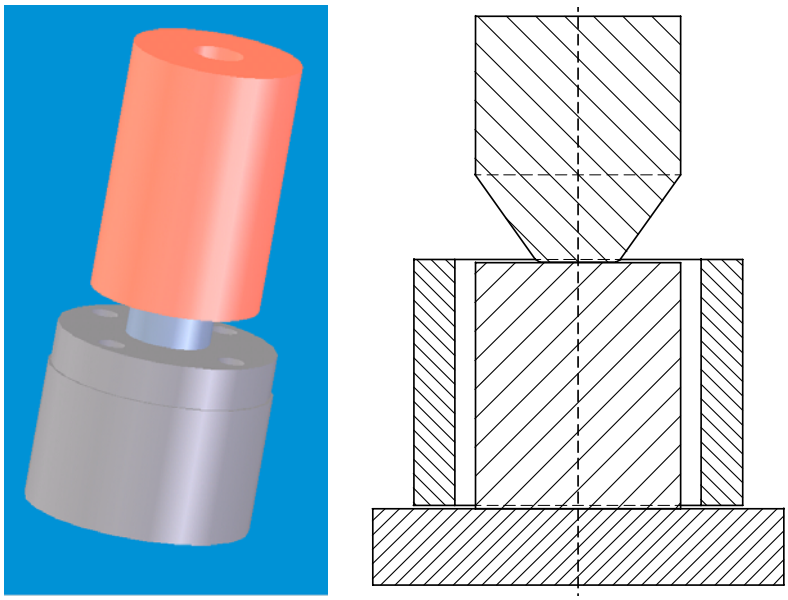

Figure B. 3: Schematics of the test setup to recreate the thermal cycle

(a) (b)

Figure B. 4: a) Waspaloy billet mounted to press top bed b) assembled instrumented test container mounted to the press ram (bottom bed)

Chromium	18.00-21.00
Boron	0.003-0.01
Zirconium	0.02-0.12
Aluminum	1.20-1.60
Titanium	2.75-3.25
Molybdenum	3.50-5.00
Cobalt	12.00-15.00
Copper	0.50 max.
Iron	2.00 max.
Sulfur	0.030 max.
Silicon	0.75 max.
Manganese	1.00 max.
Carbon	0.02-0.10 max.
Phosphorus	0.030 max.
Nickel	Balance[c]

Table B. 1: Nominal composition of Waspaloy

The test *die* was made of H13 heat treated to a hardness of 55 Rockwell C. Heat treatment was done by austenitizing at 1850 °F, followed by gas quenching and 2 cycles of tempering at 1100 °F for 2 hours each. After heat treatment, these samples were wire EDMed into 8 sections, ground to flatness and polished so that the samples are all at the same height when assembled in a container. Photograph of one such sample and assembled container are shown in Figure B.4(b) and B.5.

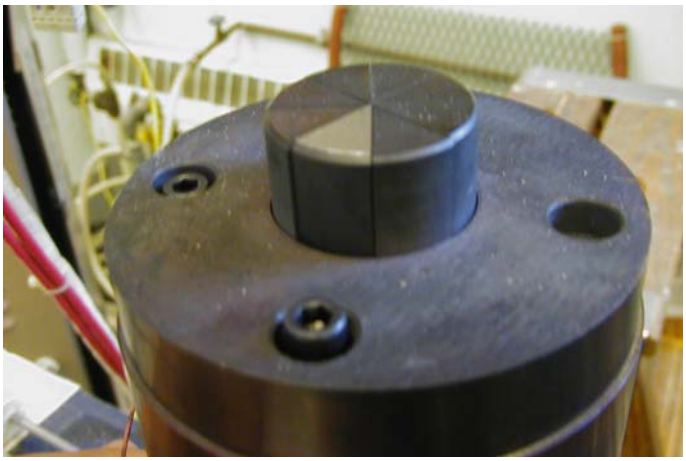

Figure B. 5: Eight H13 die samples assembled in a container

Assembled bottom die and the billet were mounted on an Instron 1322 material tester that is capable of a maximum load of 25 tons and a maximum speed of 2” per second. The billet was mounted such that it is in the hot zone of the inline Applied System Series 3320 electric furnace. A 0.04” diameter hole was drilled on the test die to within .010” of the surface and a J-type thermocouple inserted. Once the thermocouple was inserted, thermal cement was applied at the

base of the die along the wire length, so that the wire does not move during the campaign. Again, this was done to ensure quality of data obtained is acceptable. The entire experimental setup is shown in Figure B.6.

Figure B. 6: Test setup on Instron 1322

B.3 Thermal Softening Test Setup

Once the *billet* reached the set temperature, displacement controlled cycle was programmed so that the subsurface temperature reaches approximately 400-500 °C. The programmed velocity profile is shown in Figure B.7. For the trials, to ensure adequate thermal contact, ram displacements were set so that the loads were approximately 5000 lbs (or a interface pressure of about 4000 psi) The thermocouple leads were connected to a National Instrument DIN-rail mounted terminal block that has 14 unconditioned temperature inputs with cold-junction compensation and auto-zeroing. Data was logged using National Instruments Virtual Bench data logger at maximum allowed logging speed. Once the cycle was programmed, a campaign was started for a 400 piece run. The cycle time was approximately 30 seconds. Between each cycle, the dies were air cooled using pressurized wet shop air. No liquid lubricant spray was used in the test. The thermal cycle from one of the campaign is shown in Figure B.8 and Figure B.9. These two plots show temperatures recorded at a depth of .010" from the surface. The bulk temperature, also measured by a J-type thermocouple, was 300 °C and fluctuated very little. It was noted that the temperature at the surface saw a larger swing in temperature. The swing in the surface temperatures were much higher (of the order of 50 °C) at the start of the campaign and dropped to les than 40°C at steady state because of the substrate heating. Also at the surface, temperature measurements went up and down in a monotonic fashion, during the cycle.

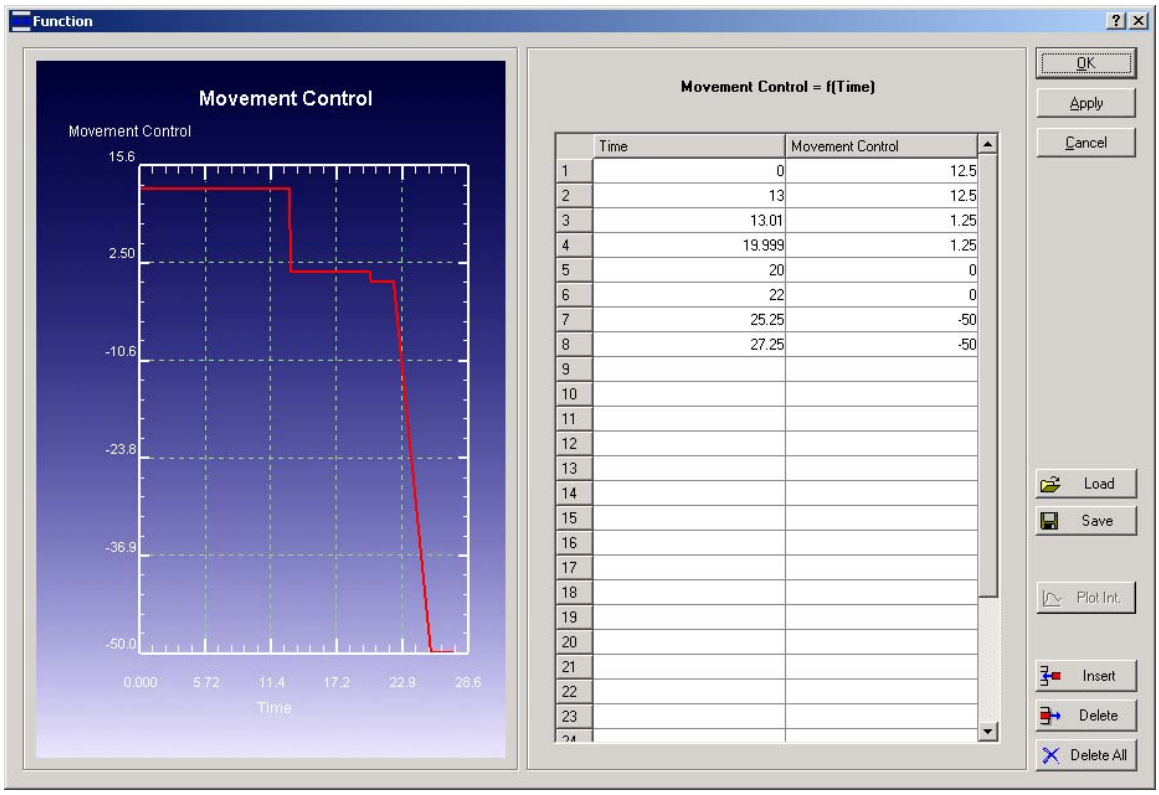

Figure B. 7: Velocity profile used in the tempering test trials, positive indicates motion of ram towards billet and negative is away from billet

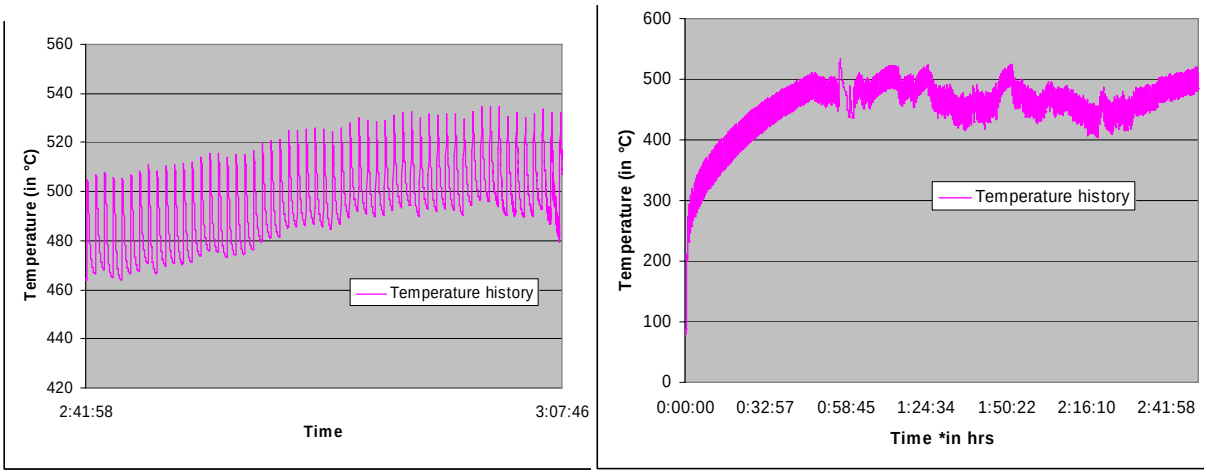

Figure B. 8: Thermal history of 0.010” below surface during contact test campaign

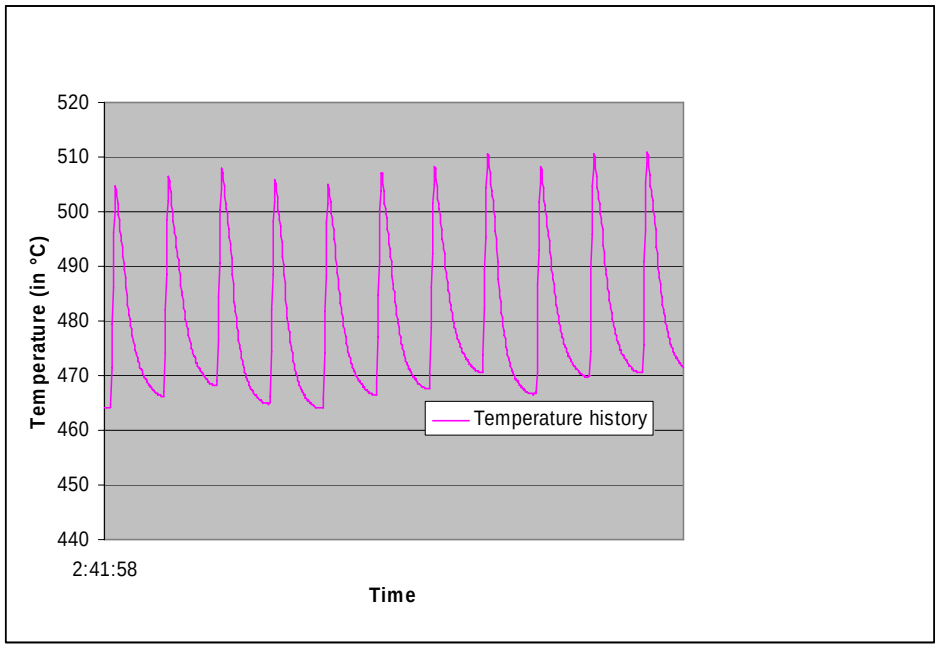

Figure B. 9: Recorded temperature at .010" below the surface (10 cycles)

The recorded temperature was then matched to numerical model to ensure the correct heat transfer coefficient is used.

APPENDIX - C

MODEL FOR ESTIMATING THERMAL SOFTENING

C.1. Proposed Formulation for Thermal Softening and Wear of Hot Forging Tools

To overcome shortcomings of the existing wear and softening model and to correlate the failure characteristics of tools to the process conditions, we need fundamental or phenomenological models that capture: Die softening or over tempering; Abrasive and Oxidation wear; and Thermal fatigue. These three mechanisms play crucial roles in failure of hot and warm forging applications. This chapter presents the tempering model and wears model developed along with methodology to integrate these into FEM.

C.1.1 Intermittent Tempering Model Formulation

As evident, the alloying elements have a strong effect on the dies resistance to thermal softening. It is also obvious from the prior section that tempering of tool steels is a complex diffusion controlled phenomena that is both time and temperature dependent. A subroutine that calculates effective tempering that occurs during a forging cycle has been designed and implemented. The subroutine works with DEFORM-2D, a explicit special purpose finite element for modeling bulk deformation. DEFORM is widely used in forging industry in US and is a suitable platform for application being tried out. A schematic representation of the algorithm used in designing the subroutine is shown in Figure C.1. Calculations to be performed at the end of the computation step (after the die temperatures have been calculated). All tempering temperatures have been normalized to 600 °C or 873 K.

C.1.2 Architecture and Model Development

The following model is used in calculating loss of hardness of dies during thermo-mechanical processing of materials. The equations used are

$$T = \left(\left(\frac{T_i(t) + T_f(t)}{2} \right) + 273 \right) \tag{C.1}$$

$$\delta t_{ET} = 10^{\left(\frac{T(C + \log \delta t_i)}{T(ref)} - C \right)} \tag{C.2}$$

$$T_{ET} = T_{ET} + \delta t_{ET} \tag{C.3}$$

$$H = 1273 \times (C + \log(T_{ET})) \tag{C.4}$$

where δt_i is the incremental time step in seconds, $T_i(t)$ is the temperature at the start of the computational step in C, $T_f(t)$ is the temperature at the end of the computation step in C, T(ref) is the reference temperature in Kelvin, T is the average temperature (in Kelvin) during the time step, C is a material constant (user input, material dependent) and H is the Hollomon-Jaffe parameter. A look-up table is needed to translate this into hardness loss.

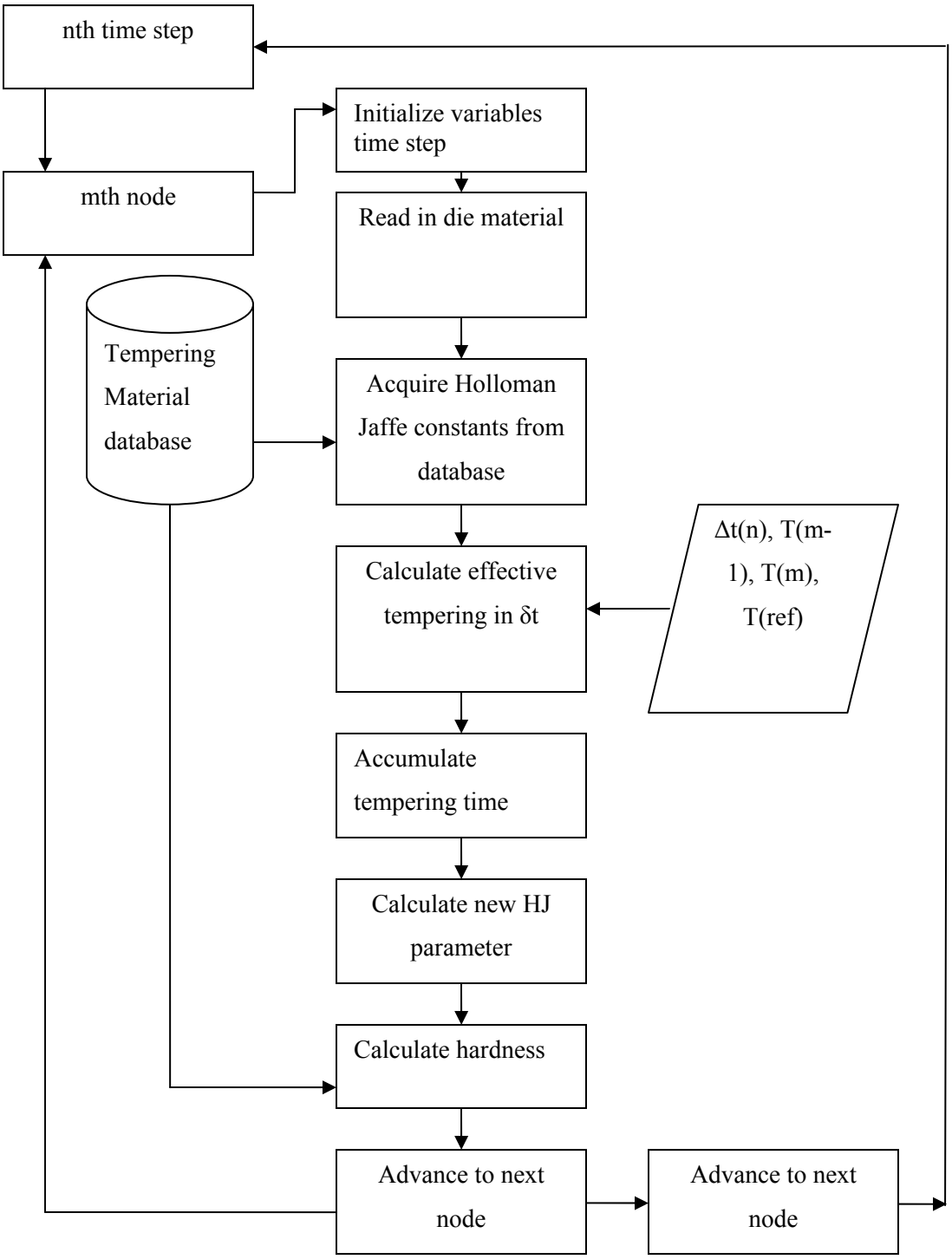

Figure C. 1: Schematics of modeling in-process hardness loss of forging tools

C.1.3. Formulation of Wear Model

As outlined before, several works exists in the literature that tries to characterize and model wear in hot forging. Some of the earlier work focused on characterizing wear as a function of process variables like forging area, weights and energy while some have taken a more fundamental approach to modeling. These models are provided in Table C.1. With advances in finite element models and computing, it is possible to use fundamental material properties and process variables derived from FEM software to model wear more universally. With the technological capabilities in mind, and with available data, it is possible to use Archard's model provided in equation 4.3 to model wear as a function of thermo-mechanical history of dies during a forging process and the working hardness of the die material.

$$wear = k\int \frac{p_i \times V_i}{H_i} dt \tag{C.5}$$

where p is normal pressure at a die location, V is the sliding velocity at any time, H is the hardness of the die location and k is a constant dependent on several factors like billet material and scale formation.

Earlier models that relied on tests to characterize wear coefficients are not fundamentally sound. Although these tests give a rough measure of wear resistance for the specific class of forgings, these cannot be extended to forgings outside the class. Phenomenological models like Archard's model are far more extendable to other applications, provided the mechanism of wear is similar. For instance, models developed or calibrated for abrasive wear can be used for other abrasive wear applications. However, these cannot be used where adhesive and oxidation wear dominates abrasive wear. Also, Archard's model does not take into account the varying softening behavior of different materials, with exposure to high temperature. Low alloy/low carbon steels have a steep drop-off in its strength/hardness with temperature compared to high alloy tool steels. In fact, some materials (like intermetallics) get stronger at higher temperatures. Also, Archard's model does not take into effect the in-service tempering behavior of tool material. The surface hardness of dies exposed to prolonged high temperatures is substantially lower that the core hardness. Also, surface also experiences decarburization. These phenomena make the surface more vulnerable to wear – a mechanism not captured by the simple Archard's relationship suggested earlier. With advent of robust FEM engines, one can now embed these mechanisms into the simplified Archard's model, to extend the model across various processes. Similar effort is being carried out by Kang [Kang, et al., 1999, Kang, et al., 1999], Jeong[Jeong, et al., 2001]and Saiki [Saiki, et al., 2001].

C.2. Demonstration of Thermal Softening Model

Tempering of the surface layers of the forging tools greatly affects the wear resistance of the tool. Process parameters like the equipment choice, forging temperature, lubricant quantity and grade and cycle times greatly affect the thermal history the dies are subjected to. These are well known among the research community, and to some extent understood by the forgers. However, the relative effects of these on the magnitude of tempering and hence wear, have not been looked at, in its complexity. The following section intends to demonstrate, through the use of the developed models, these effects, on the dies used for hot forging a gear blank. Design of tools

and process details have been obtained from Sypris Technologies, Forge Division in Marion, OH.

The modeled process forges a gear blank from AISI 8620, 2" diameter and 4" long. Parts are being forged on a 1600 ton mechanical press with a total stoke of 14" and a speed of 60 spm. Forging temperature was 1100 °C and the forging cycle time was 15 seconds. Between successive parts, the dies are lubricated manually with Acheson's Deltaforge F-31, a fine water based colloidal graphite. The forging is being done in 2 passes: the first pass pancakes the billet to remove scale and oxide layer that is forms during heating, the second pass forges the pancake to the finish size. Dies used were made of H-13, quenched and double tempered to a hardness of 48 to 50 HRC (Rockwell C scale). Before operation, these dies are typically preheated to 200 °C for better fracture toughness. A schematic representation of the 2 pass forging is shown in Figure 4.2. These conditions have been used to model the process to establish a benchmark for prediction of material over-tempering and wear.

Effect of lubricant heat

To evaluate effectiveness of forging lubricants on tempering, wear and tool degradation, several simulations were performed with varying heat transfer coefficients. The values of heat transfer coefficients used in the computer simulation corresponds to the values obtained and in some cases, extrapolated from the tests performed at the Ohio State University by Sridhar and others. Values of the interface heat transfer coefficients used were 12 KW/m^2°C, 24 KW/m^2°C and 33 KW/m^2°C, corresponding to a water based graphite lubricant diluted with 20 parts, 30 parts and 100 parts water (dilution ratio of 1:20, 1:30 and 1:100). The hardness distribution of the top die after 3000 and 5000 shots for each of these dilution ratios, is given in Figures C.3, C.4 and C.5. The hardness distribution along the surface for a dilution ratio of 1:20, is shown in Figure C.6.

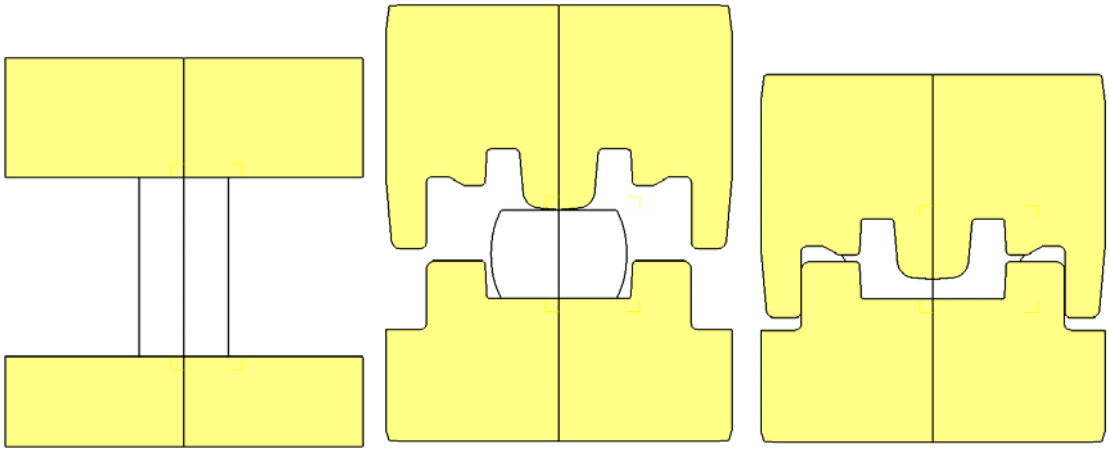

Figure C. 2: stage gear blank forging sequence (Courtesy: Sypris Technologies)

Aston and Barry {Aston, 1972 #247}	Hammer Mean damage ($x10^{-3}$) = 0.00686 x forging area + 0.0272 hammer energy - 0.1855 x forging $wt^{1/3}$ + 0.335 x spread - 0.011 x flash land area + 0.129 x flash metal escape – 0.557
Aston and Barry {Aston, 1972 #247}	Hammer Mean damage ($x10^{-3}$) = 0.000261 x forging area + 0.000763 hammer energy - 0.00265 x forging $wt^{1/3}$ + 0.012 x spread ration - 0.000694 x flash land area – 0.00266
Aston and Barry {Aston, 1972 #247}	Press Mean damage ($x10^{-3}$) = 0.0284 x forging weight – 0.062 x die material - + 0.141 (83%)
Aston and Barry {Aston, 1972 #247}	Mean damage ($x10^{-3}$) = 0.000164 forging area + 0.000712 x flash land/gap - 0.00431
Archard's model	$wear = k\int \frac{p_i \times V_i}{H_i} dt$ for volume k = constant, p = normal pressure V = velocity H = hardness
Budinski {Budinski, 1980 #316}	$w = 0.23 \times 10^{-2e-0.21x10^{-4}A}$ w = abrasion rate cm^3/min A = Structure parameter for a given tool steel (carbide size (μm) x volume fraction x carbide hardness (kg/mm^2))
Thomas {Thomas, 1970 #321}	$R = 204 - (70\ (\%C) - 4\ (\%Si) - 15\ (\%Cr)^{1/2} - 80\ (Mo^*)^{1/3}$ Mo^* = %Mo + 0.5%V + 2%V + %Nb R is the wear rate relative to H13 steel

(*) Model used by Bariani {Bariani, 1996 #342}, Batit {Batit, 1983 #314} includes an exponent to the hardness H^m, Painter {Painter, 1996 #285} uses Archard model with computer simulation.

Table C.1. Various wear models reported in the literature

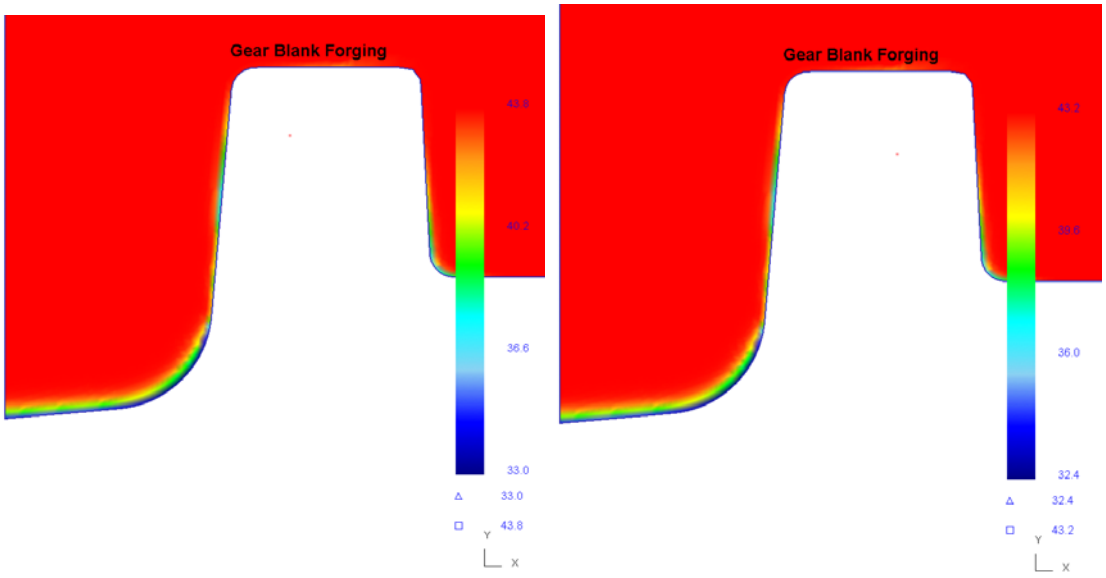

Figure C. 3: Hardness distribution after 3000 and 5000 shots, heat transfer coefficient used = 12 KW/m^2°C, press type: mechanical press

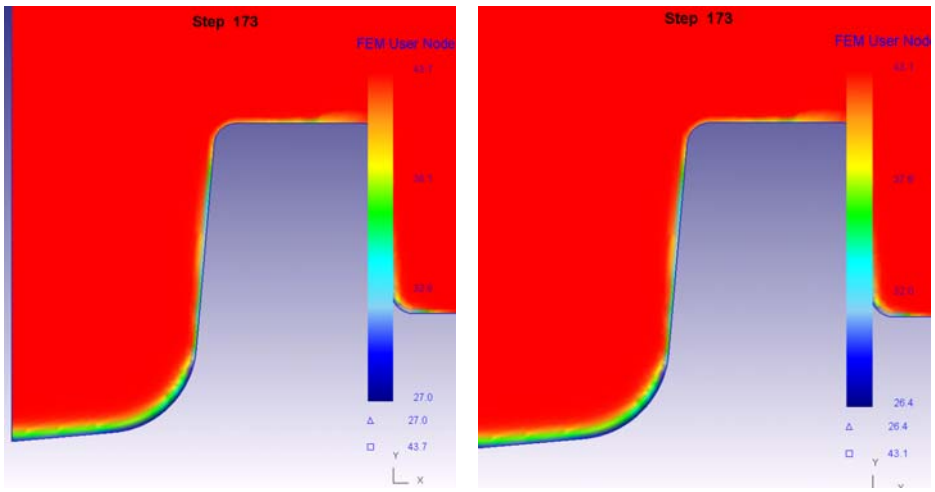

Figure C. 4: Hardness distribution after 3000 and 5000 shots, heat transfer coefficient used = 24 KW/m^2°C, press type: mechanical press

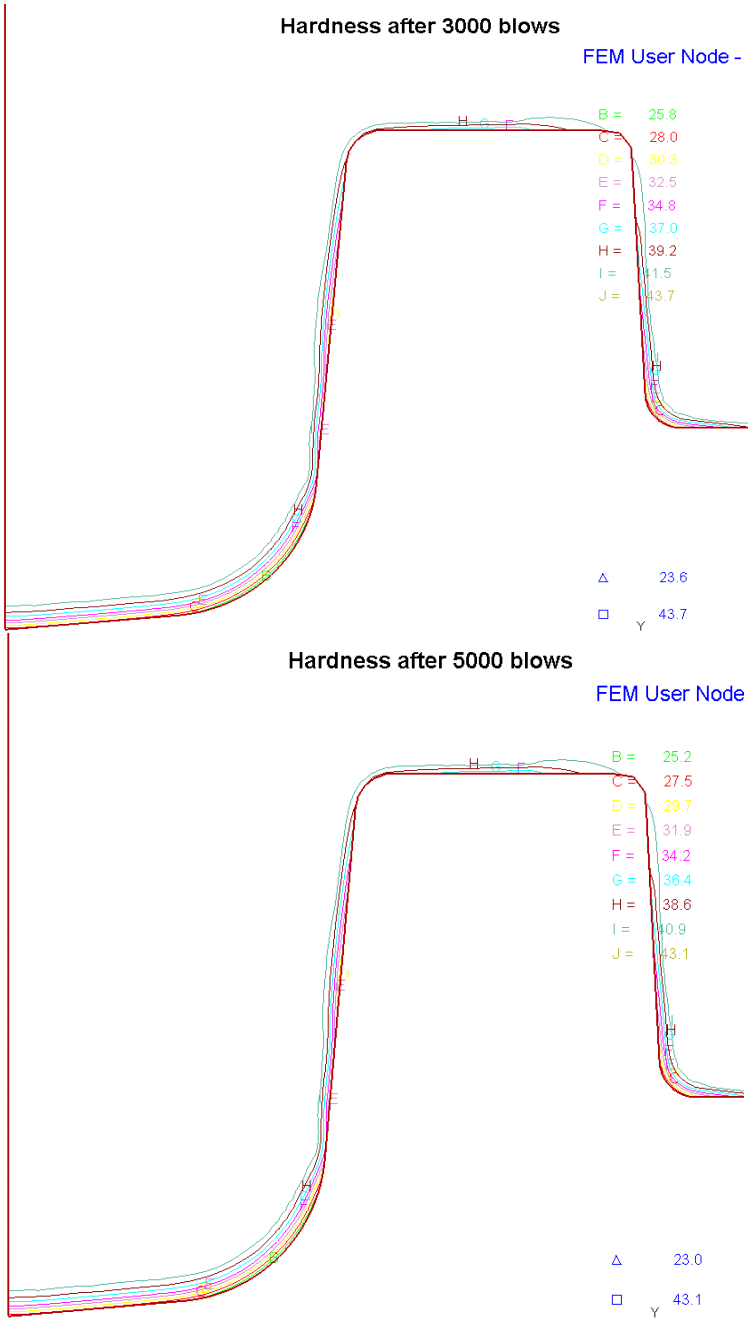

Figure C. 5: Hardness loss of the top die nose and flash areas after 3000 and 5000 strokes, assuming a heat transfer coefficient of 33 KW/m^2°C

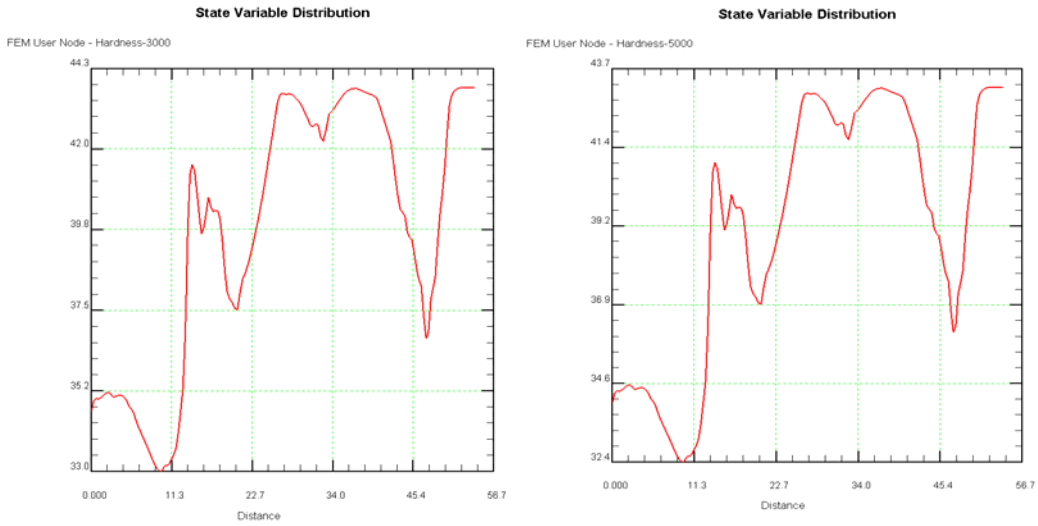

Figure C. 6: Hardness distribution at the surface, after 3000 and 5000 shots, heat transfer coefficient used = 12 KW/m^2°C, press type: mechanical press

From the above plots, the following conclusions can be made.

- Regions in the center are in general, exhibit a more prominent tempering and hardness loss because these regions come in contact with the billet earliest
- As Figures C.3 and C.6 indicate, corners have a more pronounced hardness loss. This may be due to the lower mass content in corners (higher surface to volume ratio) that disproportionately increases the area through which heat is conducted in. Typically the corners are the regions with the highest tangential or sliding velocities. Coupled with the large hardness loss, corners towards the center of the part, could possibly wear the fastest.
- The fillets exhibit the least hardness drop because these are the last areas to fill and come in touch with the hot work piece material

In these computer simulations, heat transfer coefficients are assumed to be independent of pressure. However, some research exists, that show that the lubricant film quality changes substantially with the local pressure and temperature. This in turn will affect the local friction and heat transfer coefficients, which in turn will have a dramatic effect on the local over tempering of the tool surfaces.

Effect of Equipment

To demonstrate the effect of equipment selected and contact time, several simulations have been performed with mechanical press and hydraulic presses with various ram speeds. By changing the press characteristics, we are able to change the duration in which the tools are in contact with the workpiece. In these simulations, the heat transfer coefficient has been kept constant in order to isolate the effect of equipment, on the hardness drop. Figure C.7 and C.8 show hardness distribution in the top punch, if these forgings were made on hydraulic press at a forging speed of 10 mm/sec and 20 mm/sec. The friction factor used in these simulations was 0.3 and the heat transfer coefficient used was 6 KW/m^2°C. It was noted that the softened surface effect was much more predominant in a hydraulic press compared to the mechanical press due to the longer contact times typically found in hydraulic press forgings.

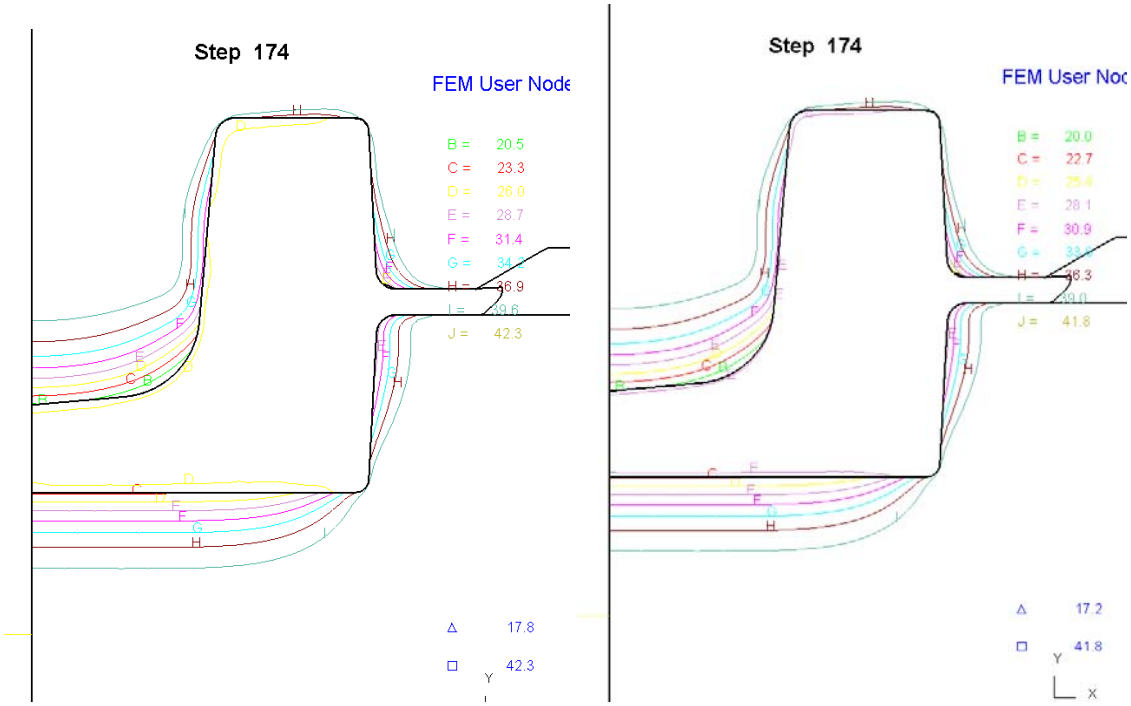

Figure C. 7: Hardness distribution after 3000 and 5000 blows, with a slow hydraulic press (p2) v=10 mm/sec, h = 6 KW/m^2 °C, m=0.3

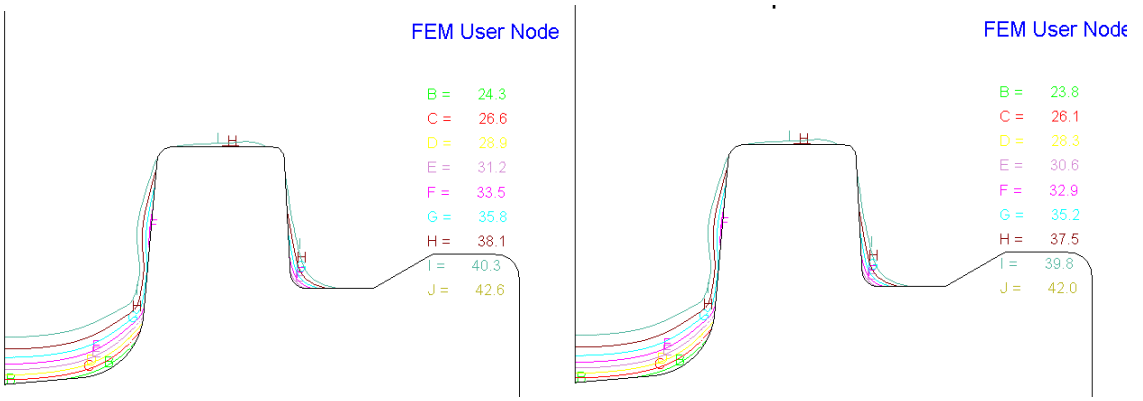

(a) (b)

Figure C. 8: Hardness loss after (a) 3000 and (b) 5000 blows, with forging on a hydraulic press with ram speed v=20 mm/sec, h = 6 KW/m^2 °C, m = 0.3

APPENDIX - D

VALIDATION OF THE THERMAL SOFTENING MODEL

D.1. Finite Element Modeling

The second step in the validation was performing computer simulation of the process. FEM simulation of the contact test was performed using a 2D explicit finite element code DEFORM2D v 8.0. Input to the FEM simulation were thermal properties and flow stress for Waspaloy and H13, interface conditions (heat transfer coefficient) and process information (billet and ambient temperature, velocity profile (Figure B.7) and steady state die temperature). The billet temperature was set at 760 °C and ambient temperature set to the measured 100 °C. Steady state die temperature was set at 250 °C. It should be noted that the flow stress had no relevance to the simulation as both objects were considered to be rigid. Apart from the standard forging simulation inputs, starting hardness (48 HRc) and H13 tempering parameters (C=16.44) were also provided as inputs. After simulation was run, the maximum temperature and peak to valley difference in temperature at the surface was obtained. and matched to what was measured.

A series of simulations were performed with different values for the interface heat transfer coefficient. The maximum temperatures were recorded at .010" below the surface. The maximum subsurface temperatures for the various heat transfer coefficients are shown in Table D.1. Based on the series of simulation, a heat transfer coefficient of 12 was found to be the most appropriate value, to be used in subsequent modeling.

1. Heat transfer coefficient (N/sec/mm/C)	2. Maximum temperature (.010")
3. 4	4. 454 °C
5. 6	6. 464 °C
7. 8	8. 486 °C
9. 10	10. 494 °C
11. 12	12. 500 °C
13.	14.

Table D. 1: Various heat transfer coefficients used in the model and corresponding maximum temperatures at a depth of .010" from surface

Using this value for the interface heat transfer coefficient, for the given thermal cycling, another computer simulation was performed to predict the level of tempering seen at the surface. The algorithm was modified so as provide values for predicted softening after 400, 800, 1200 and 1600 cycles. Table D.2 show the hardness loss after 800, 1200 and 1600 cycles at different depths. Figure D.1, D.2 and D.3 show the predicted thermal softening of the surface layers after 800 pieces, 1200 and 1600 cycles respectively.

15. Depth of measured location from surface (in microns)		16. Hardness loss after					
		17. 800 cycles		18. 1200 cycles		19. 1600 cycles	
20.	100	21.	-2.5	22.	-3.9	23.	-4.4
24.	200	25.	-2.4	26.	-2.2	27.	-3.2
28.	300	29.	-2.1	30.	-1.7	31.	-2.8
32.	400	33.	-1.7	34.	-2.0	35.	-2.1
36.	500	37.	-1.2	38.	-1.6	39.	-1.8
40.	600	41.	-1.3	42.	-1.4	43.	-1.5
44.	700	45.	-0.7	46.	-1.3	47.	-1.9
48.	800	49.	-0.4	50.	-1.0	51.	-1.4
52.	1000	53.	-0.2	54.	-0.7	55.	-0.9
56.	1300	57.	-0.1	58.	-0.4	59.	-0.9

Table D. 2: Measured hardness loss at different depths from the surface. Measurement was made using a microhardness tester under a load of 500 gms

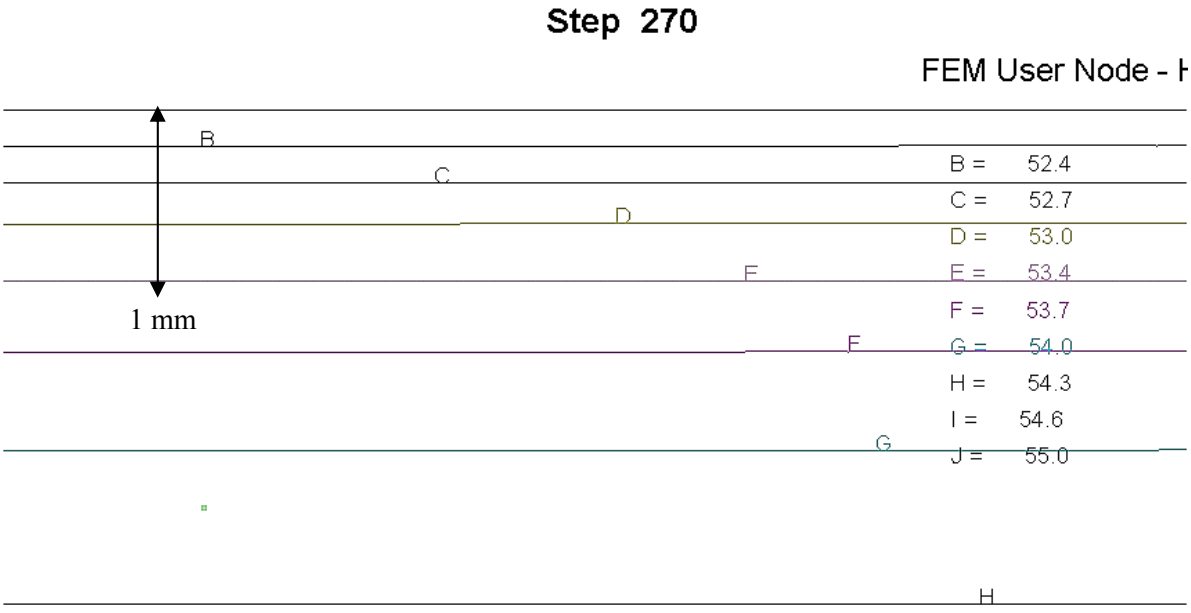

Figure D. 1: Predicted hardness loss at the surface after 800 cycles

Figure D. 2: Predicted hardness distribution at the surface, after 1200 pieces

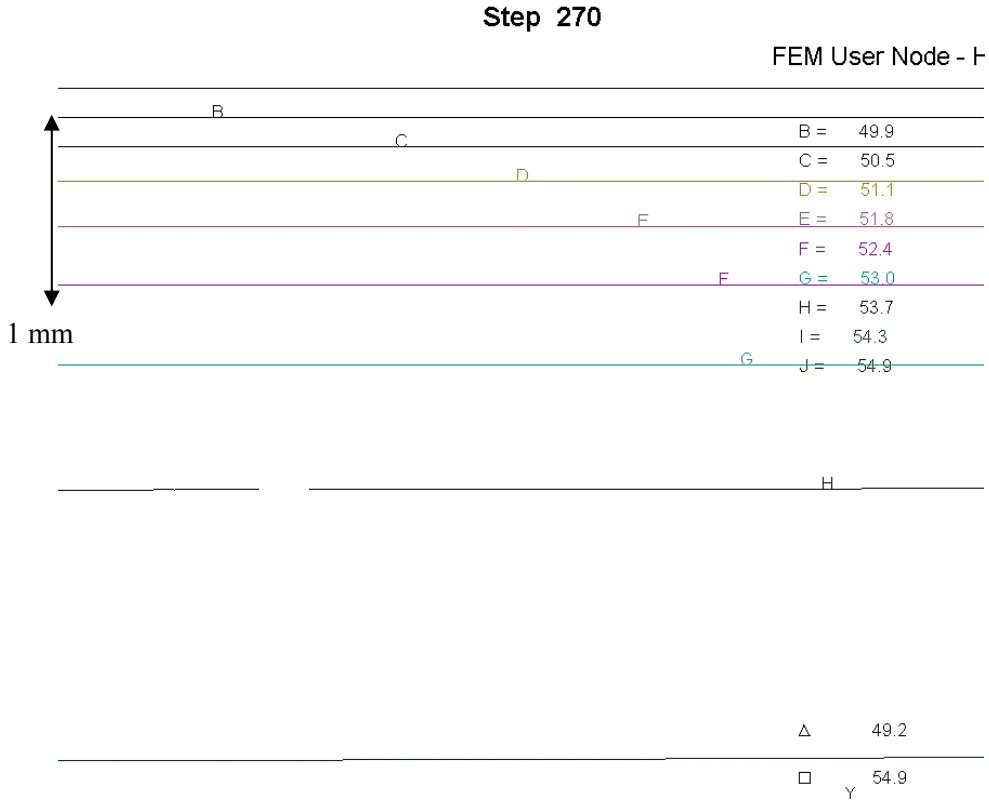

Figure D. 3: Predicted hardness distribution at the surface, after 1600 pieces

It was noted that the hardness dropped by almost 4-5 Rockwell points after 1600 cycles at a depth of 100 microns.

D.2. Characterization

During the contact test campaign, one of the samples was replaced with a brand new "sector" every 400 cycles. This approach was used so that one has a moving history of hardness at increasing number of cycles. Figure D.4 displays the hardness loss in sample runs of 800, 1200 and 1600 cycles, at different depths from the surface. It should be noted that at each depths atleast 3 hardness measurements were made. The values in the table are average values of all hardness values made at the depth. Beyond a depth of 1-1.2 mm, no distinguishable hardness gradient was observed. No hardness measurements were made at locations closer than 100 microns because of the influence of free surface on the hardness measurement. At distance, of at least twice the size of indentation (approx. 80 microns) was maintained above the indented location.

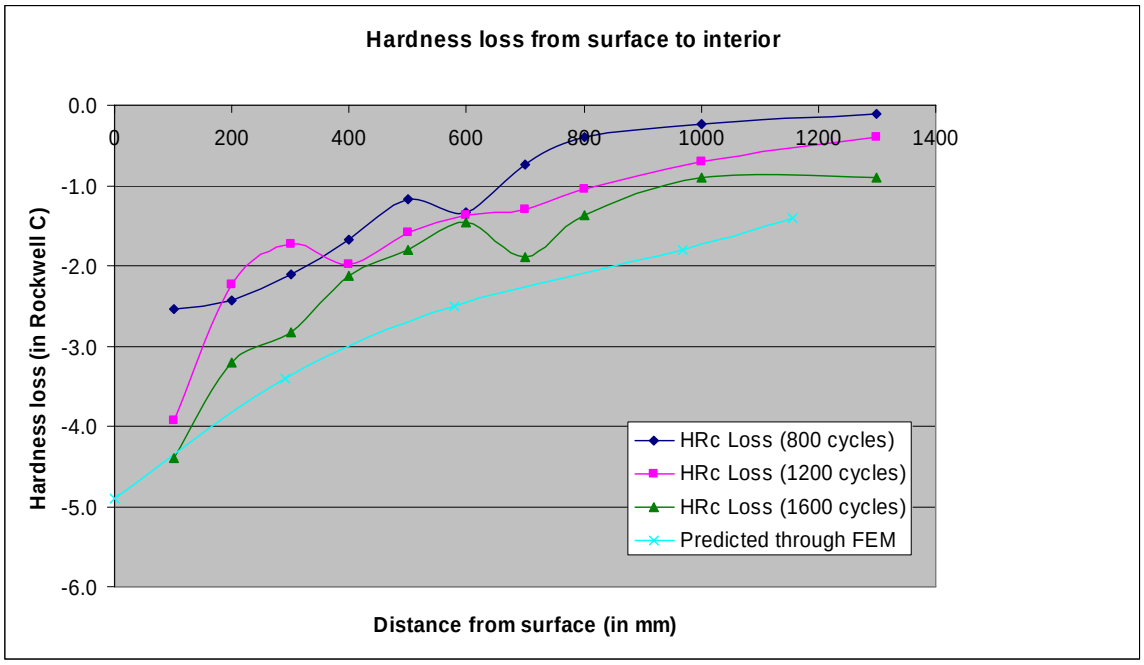

Figure D. 4: Measured micro-hardness measurements from surface to the interior

Figure D.5 compares hardness loss predicted by the model and the observed hardness loss. A fourth degree polynomial was used to get a least square fit of the measured hardness, which is being compared to the predicted hardness loss at the surface. The model predicts the hardness loss within .5-.6 HRc.

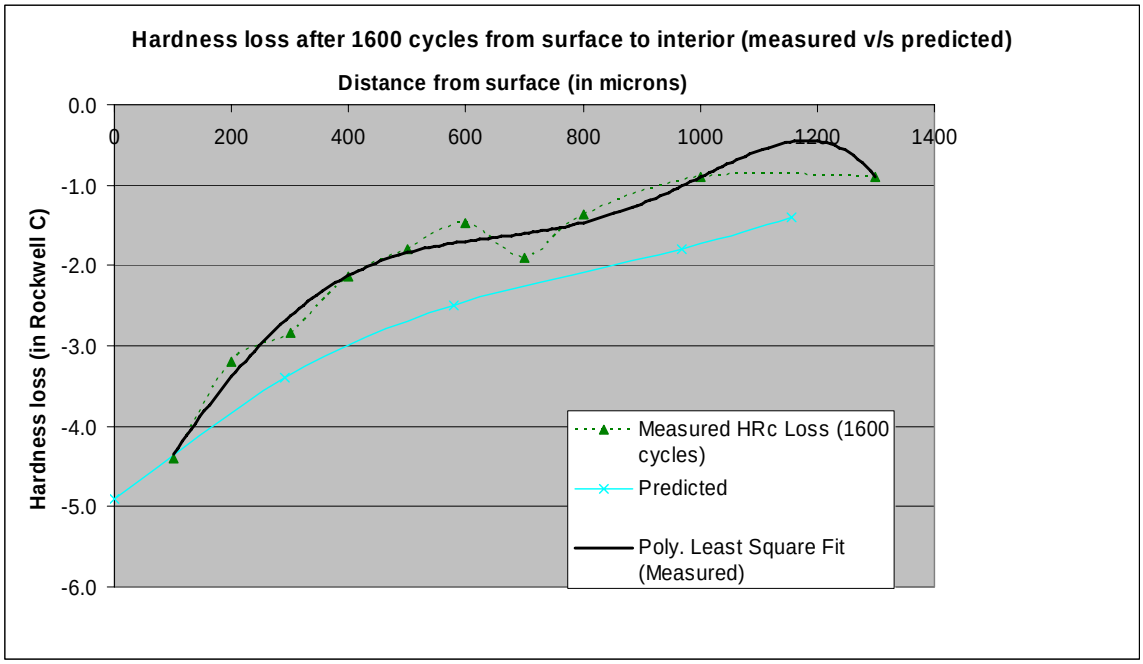

Figure D. 5: Measured value of hardness loss versus predicted hardness loss at different depths from the contact surface

D.3. Industrial Case Study

Wear model developed was tested out to predict the wear characteristics of a blocker die used in flashless precision forging of a gear blank. The following section presents the predicted wear and compares the predicted value to the measured values. The design of tooling and the process along with worn die set was obtained from Eaton Corporation, Forge Division in Marion, OH.

The modeled process forges a gear blank from AISI 4140, 2" diameter and 4" long. Parts are being forged on a 1600 ton mechanical press with a total stoke of 14.4" and a fly wheel speed of 70 spm. Forging temperature was 1010 °C (1850 °F) and the forging cycle time was 12 seconds. Between successive parts, the dies are lubricated manually with fine water based colloidal graphite mix. The forging is being done in 3 passes: the first pass pancakes the billet to remove scale and oxide layer that is forms during heating, the second pass or blocker creates a shape close to the finished part. The finisher forges part to the final size. Dies used were made of H-13, quenched and double tempered to a hardness of 48 to 50 HRC (Rockwell C scale). Before operation, these dies are typically preheated to over 150 °C through the use of flame rings. A schematic representation of the 3 pass forging of the gear blank is shown in Figure D.6. These conditions have been used to model the process to establish a benchmark for prediction of wear. Figure D.7(a) show the worn finish and blocker dies and Figure D.7(b) shows a close-up of the blocker die after a run of 2400 pieces. Although the finish dimensions are more critical, wear in blocker pass is considerably more. This is because, blocker pass, in general, involves a substantial movement of metal. The finish pass is used mainly to ensure the part is finished to the final dimensions. Because of this reason, for validation of the wear model, the blocker stage forging was used.

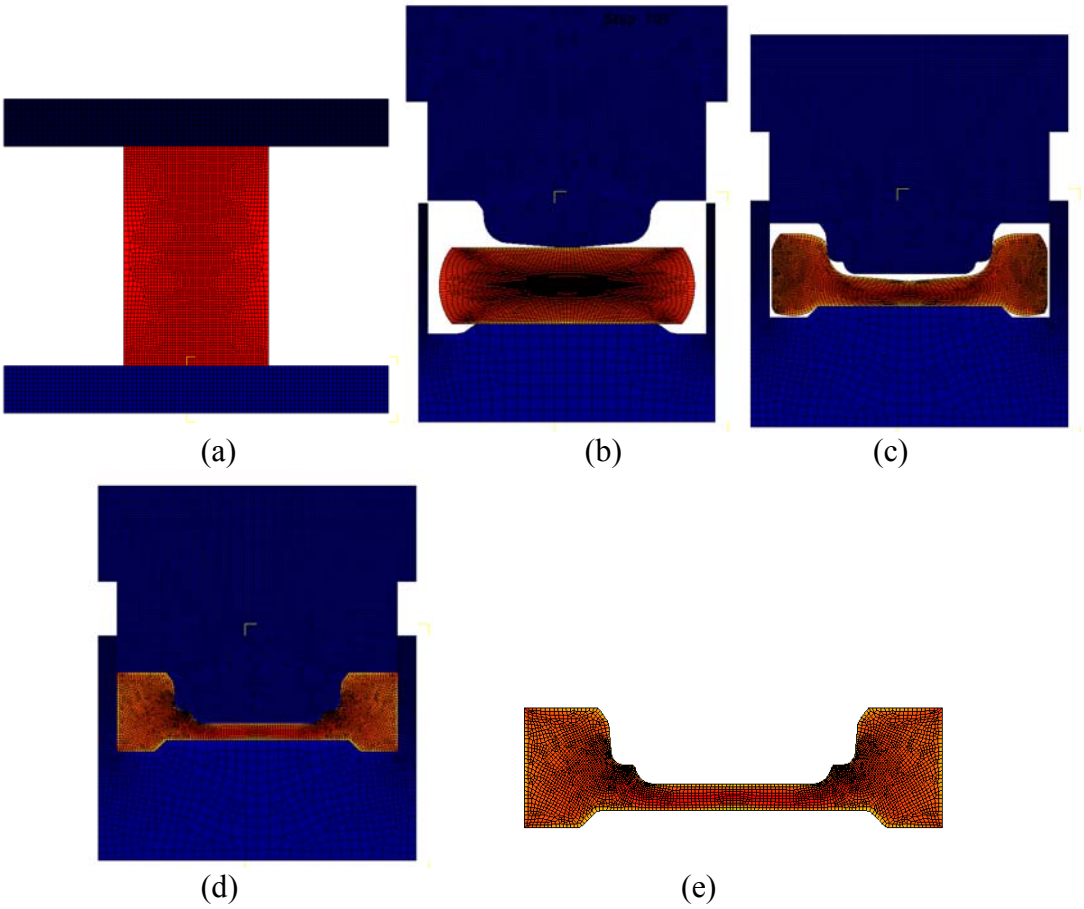

Figure D. 6: Schematics of a) buster, b) blocker c) finisher d) end of stroke and e)gear blank forging (courtesy: Eaton Corp., South bend, Indiana)

Validation of the wear model involves computer modeling of and wear and correlation of the predicted wear to the actual wear profile. Properties that are critical to the use of prediction were the tempering parameter of H13, initial hardness of the dies and the hot hardness of H13. A tempering parameter of 16.44 was used for the model. Starting hardness of the dies ranged from 48-50 (per Eaton Corp). The hot hardness of H13 was obtained from standard data sheet for H13 and sown in Table D.3.

Test Temperature	HRC	Test Temperature	HRC
70°F (21°C)	46	500°F (260°C)	40
200°F (93°C)	43	600°F (316°C)	39.5
300°F (149°C)	42.5	800°F (427°C)	37.5
400°F (204°C)	41	1000°F (538°C)	29

Table D. 3: Hot hardness of H13

(a)

(b)

Figure D. 7: (a) Worn blocker and finish dies (b) Close-up of blocker used in validation

Process information used in the computer simulation corresponded to what was used in the actual forging. Due to lack of data, a standard heat transfer coefficient of 11 KW/m^2 °C was used. This value is generally accepted as a standard heat transfer coefficient where water based graphite is used. Figures D.8, D.9 and D.10 show the wear profile in the top blocker die predicted by the model.

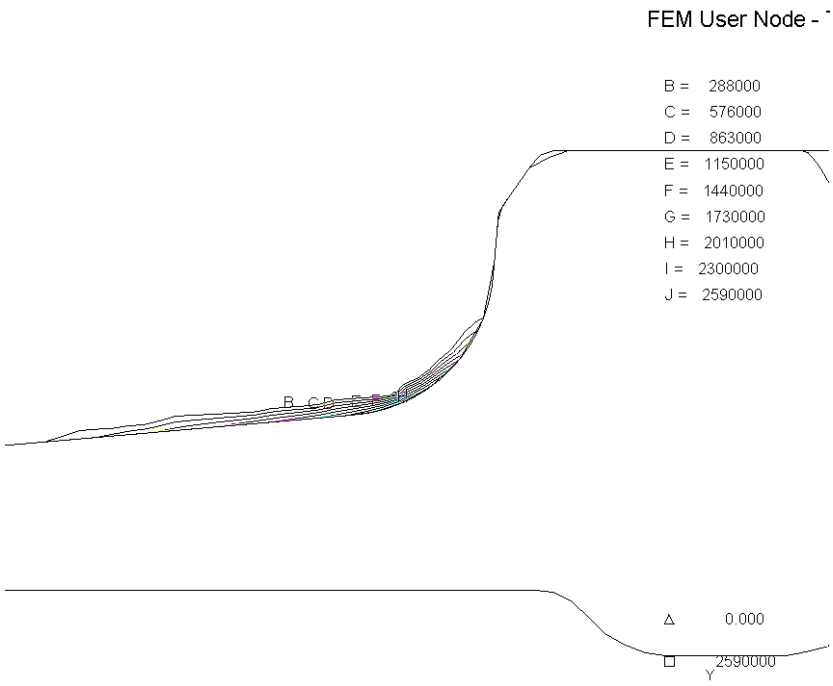

Figure D. 8: Predicted total wear profile in blocker die for the gear blank forging case study

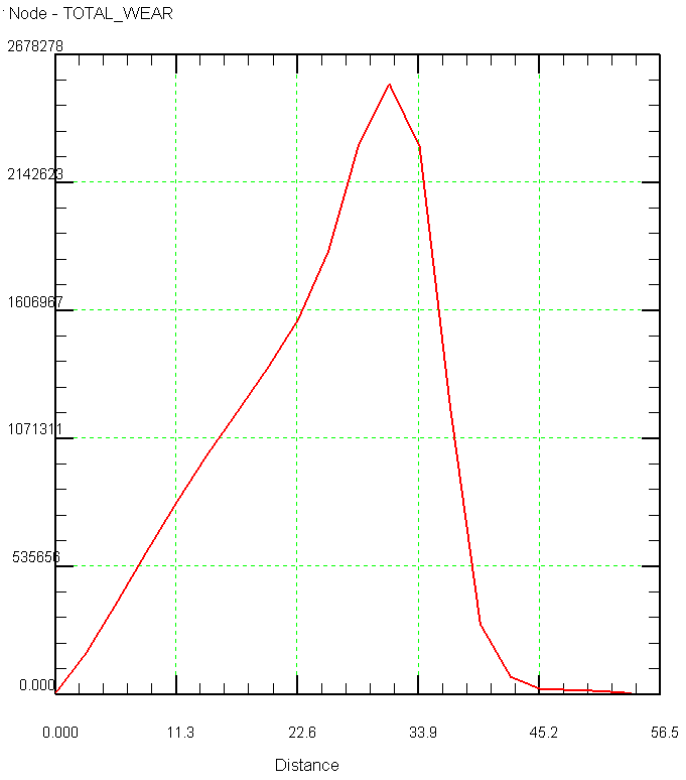

Figure D. 9: Predicted total wear distribution center to outside diameter, in blocker die

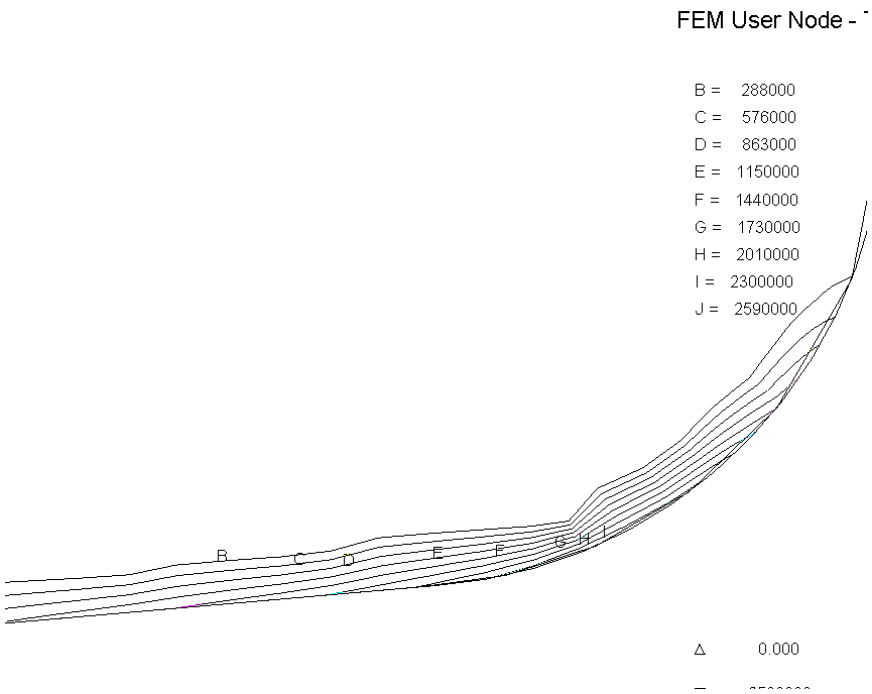

Figure D. 10: Corner wear predicted using modified Archard model

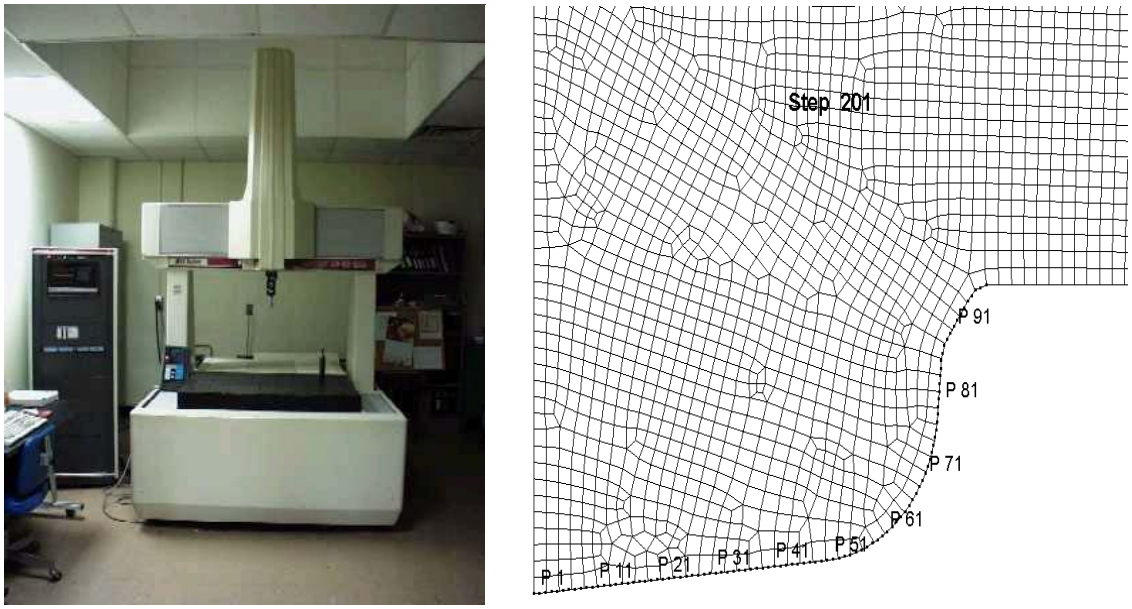

Figure D. 11: Worn die and Sheffield Cordax contact type CMM used to measure the profile of the worn die

Simultaneously, profile of the worn blocker die was measured using a Sheffield Cordax coordinate measuring machine (CMM) with a 1 mm ruby tip (Figure D.11). The CMM has a rated linear accuracy of 0.0003", a volumetric accuracy of 0.00043" and a repeatability of

0.00012". . To ensure consistency of data, measurements were made in 4 different radial directions. This also ensures that the effect of misalignment or mismatch during forging (which is not part of the 2D finite element model) on wear gets smoothed out, to some extent. Once data was collected, the data was converted to a CAD format by converting this data to a IGES file and importing this file into a CAD software Solidedge. This process allowed comparison of the worn profile to the original CAD file. To be consistent, the wear values reported was measured perpendicular to the surface of the die at the measured location. It was assumed that the CAD profile used to evaluate the worn die was a true representation of the shape of the original die. Figure 5.21 shows the graphical approach used to measure wear.

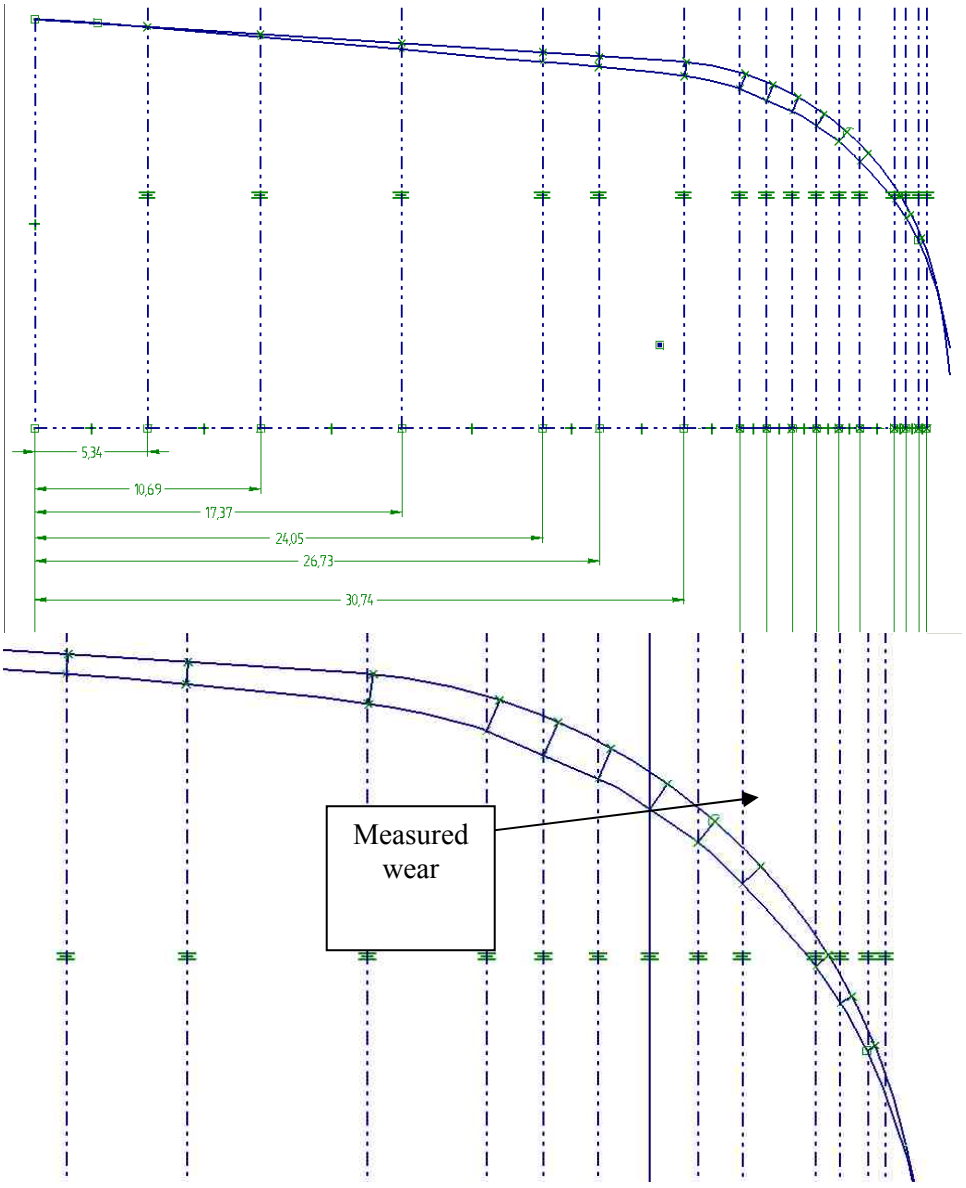

Figure D. 12: CAD approach used to compare the predicted and measured wear profile

Table D.4 shows the results of the wear measured. The table also shows the values obtained for the predicted wear in the blocker stage die. The predicted values have been normalized so that the peak values of the predicted wear and the measured wear are the same. This method, hence, only tests the validity of the wear model in predicting the relative wear at different locations. However, it should also be noted that the absolute values of the wear predicted can be compared across other similar forgings, with reasonable confidence.

X (mm)	Predicted	Normalized	Measured
5.34	293000	0.095	0.02
10.69	636000	0.205	0.14
17.37	1040000	0.336	0.28
24.05	1410000	0.455	0.44
26.73	1580000	0.510	0.5
30.74	2040000	0.659	0.68
33.38	2380000	0.768	0.75
34.65	2470000	0.797	0.82
35.86	2540000	0.820	0.75
37.01	2390000	0.772	0.69
38.08	2240000	0.723	0.6
39.06	1770000	0.571	0.57
40.69	975000	0.315	0.38
41.24	516000	0.167	0.3
41.85	196000	0.063	0.21
42.23	69900	0.023	0.1
42.49	43300	0.014	0
43.33	0	0.000	0

Table D. 4: Predicted, normalized and measured values of the wear in blocker die

Maximum wear is seen at the punch nose radius. Predicted wear and measured (Figure D.13) values show a sharp drop beyond the midpoint of the radius. This is due to the fact that outside the center of the nose radius, the pressures are lower. It was noted that the model predicts the peak of the worn profile within 1 mm in the radial direction. However, the model over predicts the wear near the center by a significant amount. The plot only extends till the base of the central hub. Both the measured and predicted wear beyond this region is negligible, as these regions are subjected to minimal sliding and considerably lower normal pressures and temperatures compared to the center of the punch.

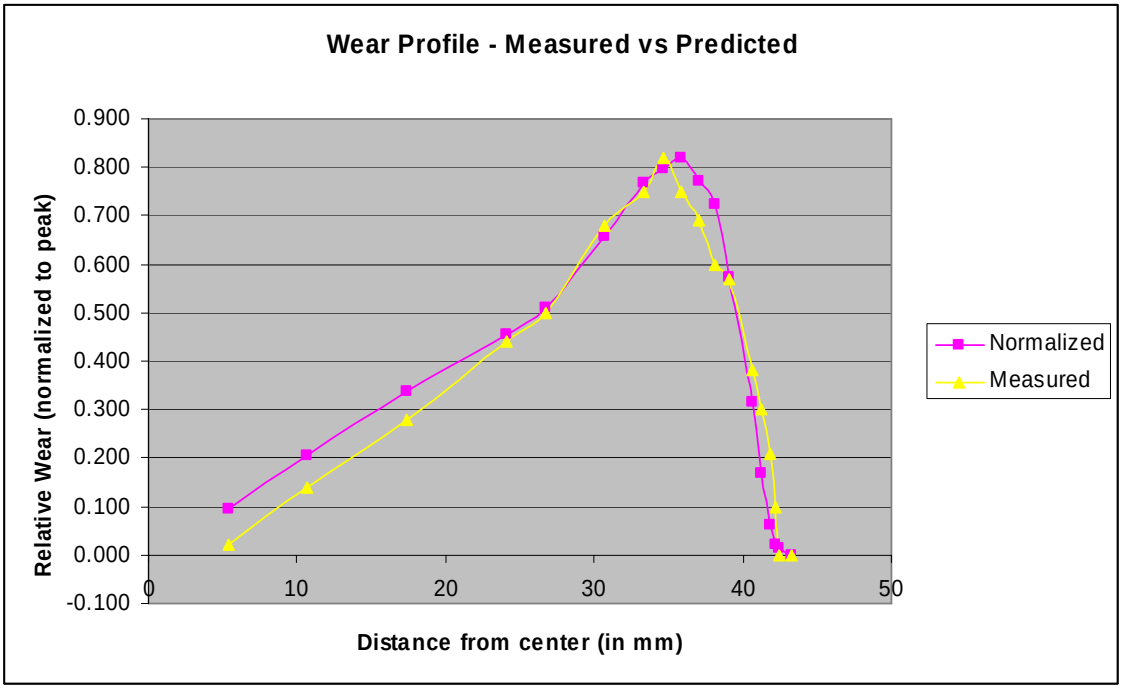

Figure D. 13: Measured and predicted wear profile in blocker die of hot precision gear blank forging case study

APPENDIX - E

STUDY OF POLLUTION AND HEAT TRANSFER IN HOT FORGING LUBRICATION

Lubrication plays a critical role in the efficacy of metal flow, die surface thermal softening, and pollution during hot processing of metals. The lubricant is often applied to the hot die surface between 250 to 600^{o}C by spraying a dilute graphite suspension through high pressure nozzles. This results in the formation of steam, followed by nucleate boiling of the residual liquid, and in the end lubricant spreading and film formation on the hot surface that is continuously loosing heat. This chapter presents a comprehensive approach to study and model the effect of the lubricant properties, dilution ratio, spraying parameters and the transient nature of the thermal and physical phenomena. Results of single the droplet and the spray tests with graphite suspensions in water have been included to demonstrate these effects.

E.1 Introduction

In the hot forging process, lubricant is applied by spraying a dilute water-based graphite suspension on the heated dies during the forging cycle that consists of placing the billet on the preheated dies, forging, ejection and post ejection lubricant spraying. The lubricant spray chills the die surface which may reach a temperature as high as 700^{o}C during forging and about 450^{o}C post ejection spraying. Best operating temperatures for hot working die steels such as H-13 are in the range of 200 to 300^{o}C. Therefore, the spray process effects the deposition of the film and the heat transfer from the die which in turn affect the thermal softening and thermal fatigue of the die surface. A large spray time and slow flow rate increases the forging cycle time, affects productivity and increases thermal softening, while a shorter time (large flow rate, large heat flux) increases thermal fatigue. Current problems like poor lubrication performance, excessive lubricant consumption, and lack of temperature control result from poor design of the spray system or poor selection of spray parameters. Another major problem is air and water pollution during due to the presence of graphite particles in the environment, Fig. E.1. Overexposure to graphite can cause coughing, dyspnea, black sputum, or impairment of the pulmonary function. This is so important that OSHA has set up a TWA permissible exposure limit (PEL) for graphite that is 2.5 mg/ m^{3}. The goal is to completely eliminate aerosol emissions within the forging plants.

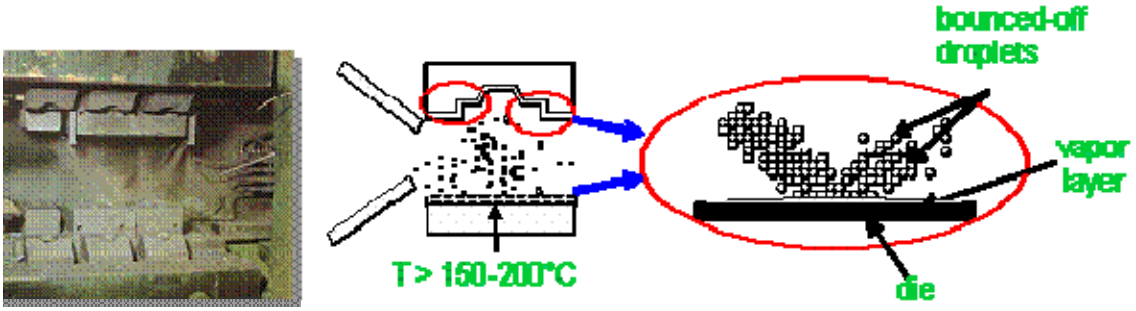

Figure E. 1: Excessive consumption of lubricant and significant pollution from lubrication.

The work by [Bariani et al., 2002] on water sprays in hot forging is amongst the first systematic attempt to study the effect of feed pressure and flow rate on the heat transfer coefficient between heated flat dies and the lubricant. Their experimental work includes results from two different spray configurations: downwards towards the bottom die and upwards towards the top die. They conclude that the increase of the feed pressure and the flow rate increases the heat transfer coefficient for both the spray configurations. Studies reported on lubricant sprays in die casting and rolling processes also conclude that a higher liquid flux density, defined as average liquid flow rate per unit area, provides a higher heat transfer coefficient for a given surface temperature [Tseng, A.A. et al, 1989; Horsky, J. et al., 1994; Liu, G.W. et al., 2000; Aoyama, S. et al., 1991; Reiners, U. et al., 1985]. However, the heat transfer coefficients and the heat flux reported in literature vary by factors of magnitude. Therefore, the recent studies have focused on understanding the fundamental physics underlying the impact of liquid droplets on hot surfaces [Savic, P., 1955; Quiao, Y.M., 1997]. This knowledge will help explain some of the conflicting results not only in liquid sprays in industrial processing but also those in fuel injectors, ink jet printers, painting and mist formation. In addition to experimental studies, numerical simulations models have also been developed to characterize the physics and thermodynamics of the spray process [Pasandideh-Fard, M., 2002]. Many of these studies could be relevant to the forging lubrication field. Consequently, this paper takes a comprehensive look into the modeling of fundamentals phenomena and their applications to hot forging lubrication.

E.2 Factors Affecting Lubrication in Hot Forging

There are several factors unique to spray lubrication in hot forging: The lubricant contains fine particles of graphite (submicron to several microns in diameter) in colloidal suspension in liquids (surfactants, binders, oil or water) that change the droplet surface energy, rheology, physics and thermodynamics. The composition of the lubricant is often a trade secret and cannot be directly determined. Hence, an inverse method must be used to determine the properties of the lubricants relevant to lubricant deposition and the film formation. The lubricant spray consists of extremely fine droplets of varying diameters distributed spatially. It is almost impossible to measure individual droplet size and distribution. A statistical procedure must be used to capture the spray dynamics. The die surface temperature looses heat continuously due to steam formation, nucleate boiling, convention and dryoff. This heat transfer phenomenon is transient and cyclic. The die surfaces have deep cavities with complex geometries, inclined surfaces and varying surface temperatures. Therefore, a strong coupling exists between the geometrical and thermophysical attributes. This relationship is shown schematically in Fig. E.2. The die surface properties, the lubricant dilution ratios (and the thermophysical properties), and the spray parameters determine the "spraying system". The parameters of this system affect the deposition mass of the lubricant on the die surface (and its thickness distribution) and the heat flux (and the die surface temperature) as functions of the lubrication time. Arrows in the plots indicate increasing solid content in the lubricant (reducing dilution ratios).

The interaction between the sprayed lubricant and the heated die surface is so complicated that it is very difficult to optimize the die cooling, with the lubricant deposition and droplet bouncing off simultaneously. Sometimes one can improve the rate of lubricant deposition but may adversely affect die

cooling. Therefore, it is essential to tackle this problem in variety of ways including experiments, mathematical models (deterministic as well as stochastic) and numerical simulations.

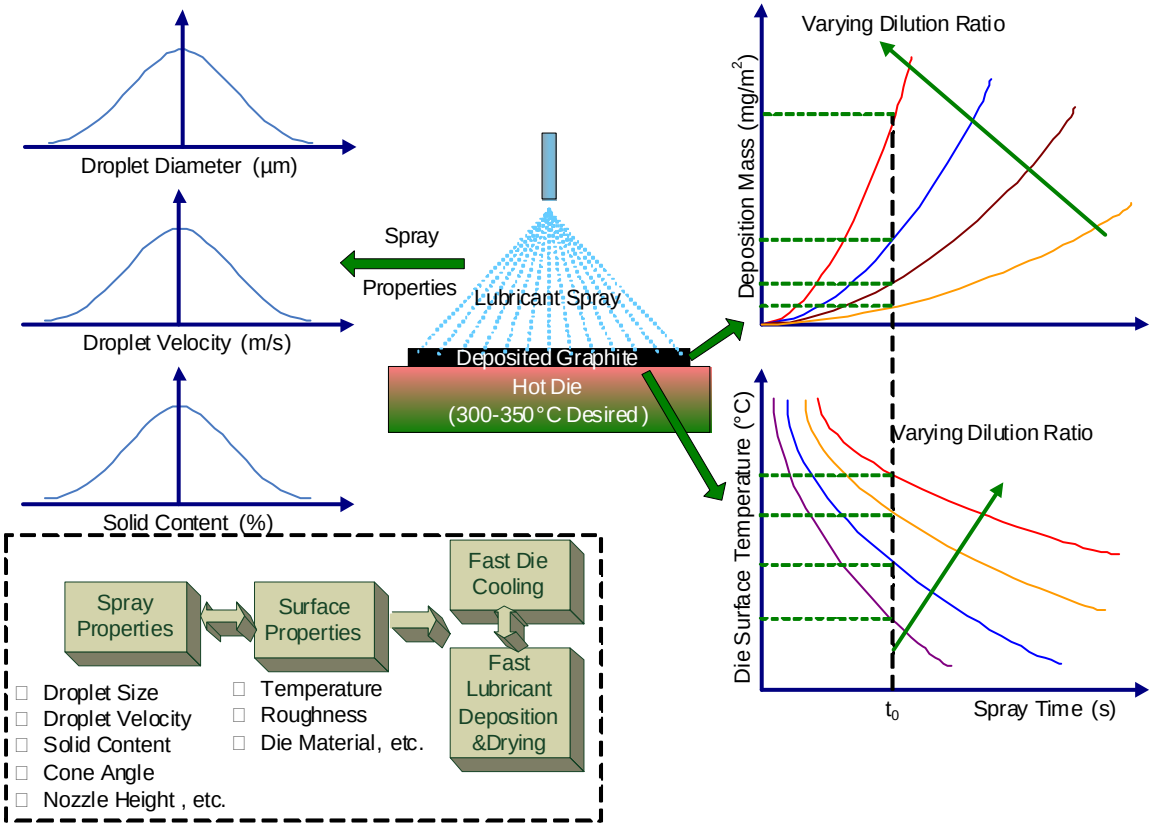

Figure E. 2: Factors influencing lubricant deposition and die cooling.

A comprehensive approach has been adopted at the Center for Excellence in Forging Technology at the Ohio State University in studies that combines continuum mechanics, stochastic modeling and simulation with observations and controlled experiments including:

- Single droplet experiments to investigate the thermo-physics of different phenomena such as steam formation (bounce off), first formation of bubbles on the heated surface (Liedenfrost point, T_{Leid}), nucleate boiling (bubbling and wetting), spreading of the lubricant film and lastly the break up of the film at high impact velocities. These phenomena are best represented through non-dimensional Weber number *We* (ratio of kinetic energy to surface energy) that defines the stability of bubbles in an isothermal system.
- Single droplet numerical modeling and simulations to study the mechanics of different phenomena and to inverse calculate the properties of the lubricants by comparing the numerical predictions to actual observations.
- Spray experiments using industrial lubricant spraying equipment and hot plates to study the thermo-physical phenomena of multiple droplets with spatially and temporarily distributed parameters.
- Stochastic models of the spraying process (multiple-droplet sprays) that capture the mechanics of the spray process and help determine the optimal spraying conditions for

desired deposition and heat transfer.

E.3 Study of Single Droplet Impact on a Hot Surface

In the study of droplet impact on hot surface the following has been observed. At high surface temperatures, steam forms between the droplet and the surface causing the droplet to bounce off. In water based graphite this leads to pollution with graphite particles depositing on the surrounding surfaces and the press structure. As the surface cools due to heat loss, the droplet stays on the surface but is separated from it by a steam blanket. The heat transfer is low in this regime of film boiling in Fig. E.1 (regime IV). The point of least heat flux is called Leidenfrost point.

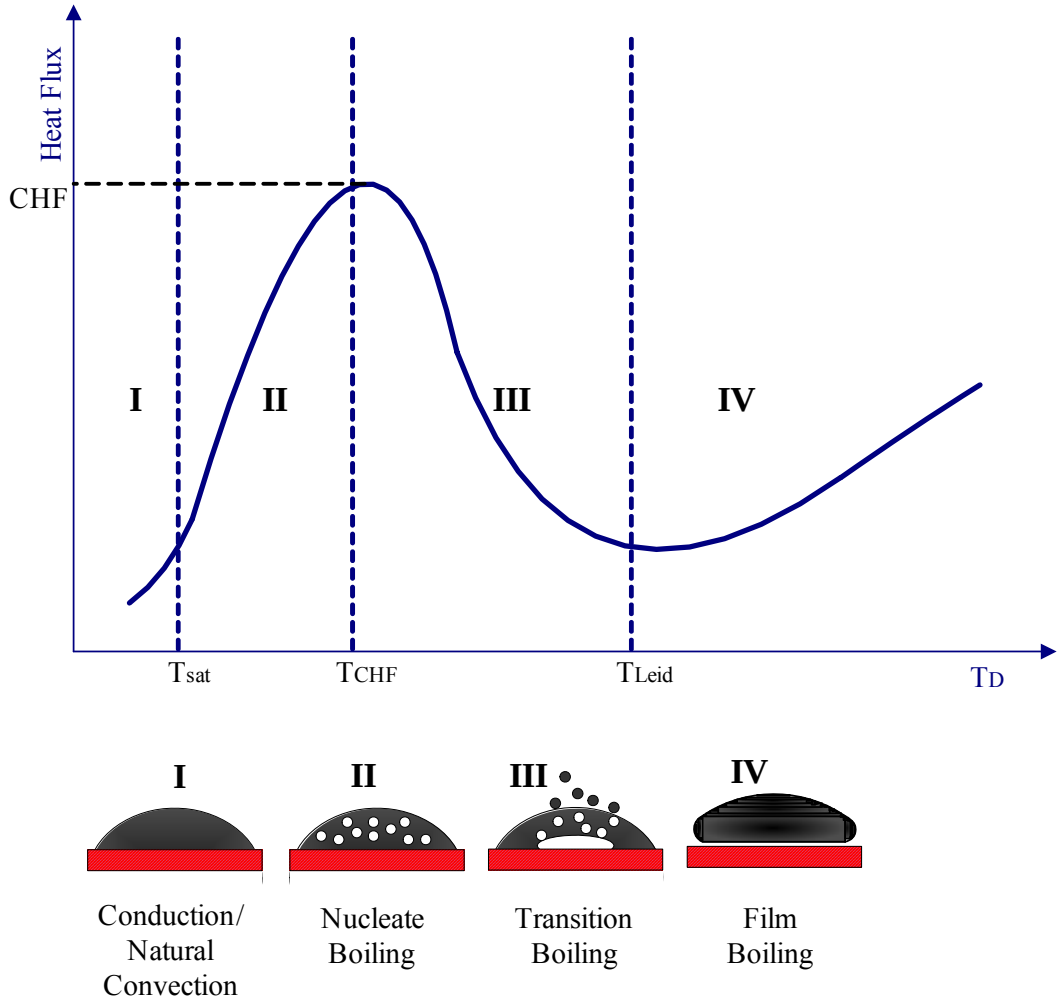

Figure E. 3: Boiling curve of a droplet deposited on a hot solid surface.

On further cooling of the surface, the droplet enters a regime of transition boiling (regime III in Fig. E.2). The heat starts increasing as the steam can escape from the surface. The heat transfer reaches a maximum when nucleate boiling initiates with vigorous convection (regime II in Fig.

E.2). The point of maximum heat transfer is called CHF (critical heat flux). At significantly lower surface temperatures the heat transfer is through natural convection and vapor release (regime I in Fig. E.2).

To study the effect of these phenomena a simple experiment was set up with a syringe mounted on a fixture to create droplets, a hot die steel surface heated by band heaters and a temperature measurement system using thermocouples, Fig. E.3, the same as Fig. E.4. A camcorder and a high speed camera took pictures of the droplet formation and its kinetics during impact on the heated surface. The images were later sent to computer for imaging processing to measure deposition dimensions

E.4 Experimental Results

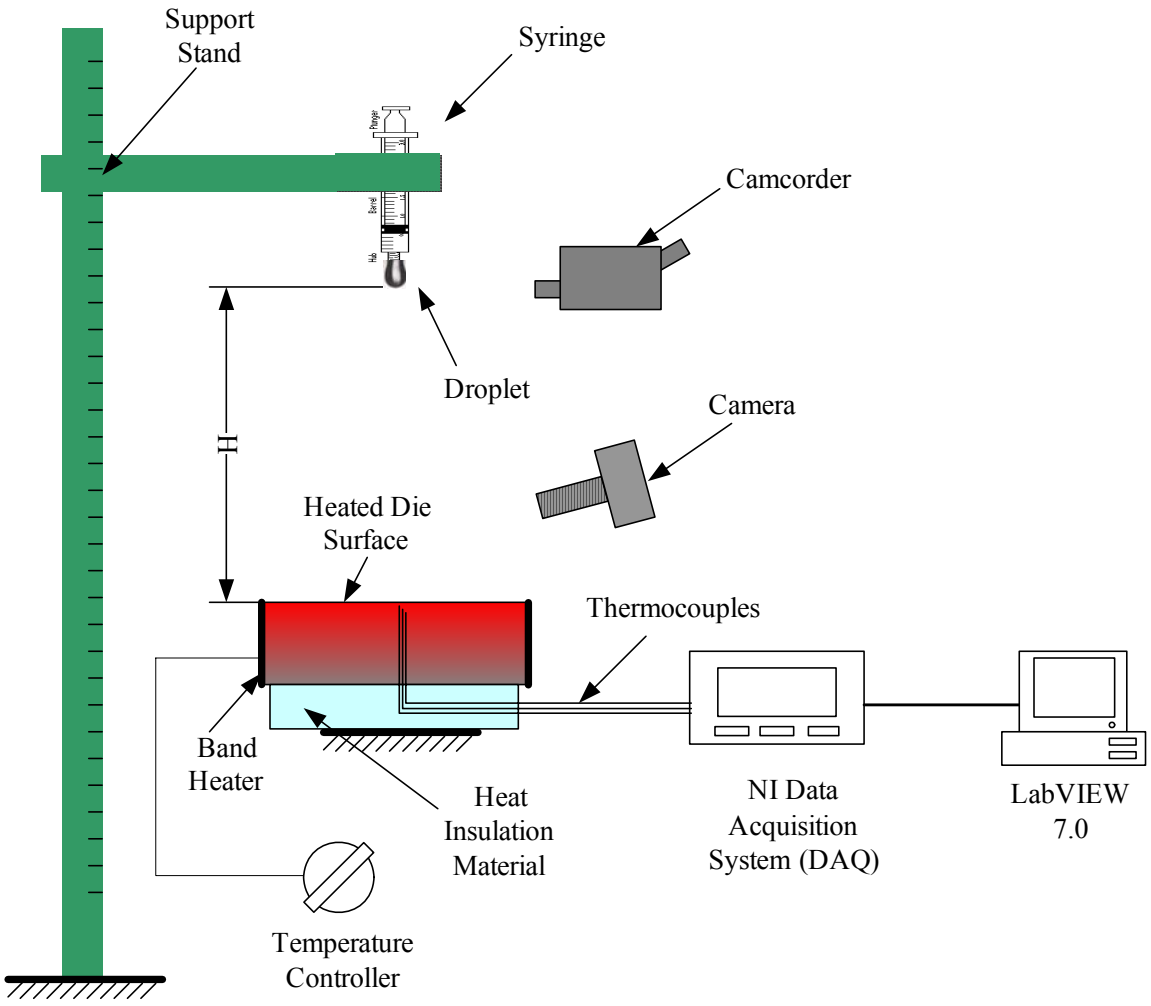

Figure E. 4: Schematic experiment setup.

In the preliminary experiment, 3mm diameter droplets were put on the die surface with zero velocity so that dynamical effects on the boiling behavior were neglected, i.e., quasi-steady state.

The flat H-13 steel surface was finished to roughness Ra 50 micro-inch (or 1.25 μm) and heated by a band heater whose temperature was adjustable from room temperature to 450°C. Temperatures during droplet impact were measured by fast response thermocouples (response time ≤ 2ms) embedded 0.5 mm, 1 mm and 1.2 mm beneath the surface of the die. The voltage signals of thermocouples were recorded on a data acquisition system.

E.4.1 Heat flux

Fig. E.4 shows that lubricants with 1:20 and 1:5 dilution ratios have the best overall cooling performance, highest average heat flux, as compared with water in the convective boiling stage. As the dilution ratios are reduced, the behavior shifts from lubricants-in-water to water-in-lubricant and the heat flux reverses. The reason behind this phenomenon can be explained as the balance of the two opposite effects of suspended graphite particles: helping to nucleating bubbles at low dilution ratios (almost as contaminants) and thwarting of the bubble movement (due to high surface tension) at low dilution ratios.

E.4.2 Critical Heat Flux (CHF) and the Leidenfrost Point

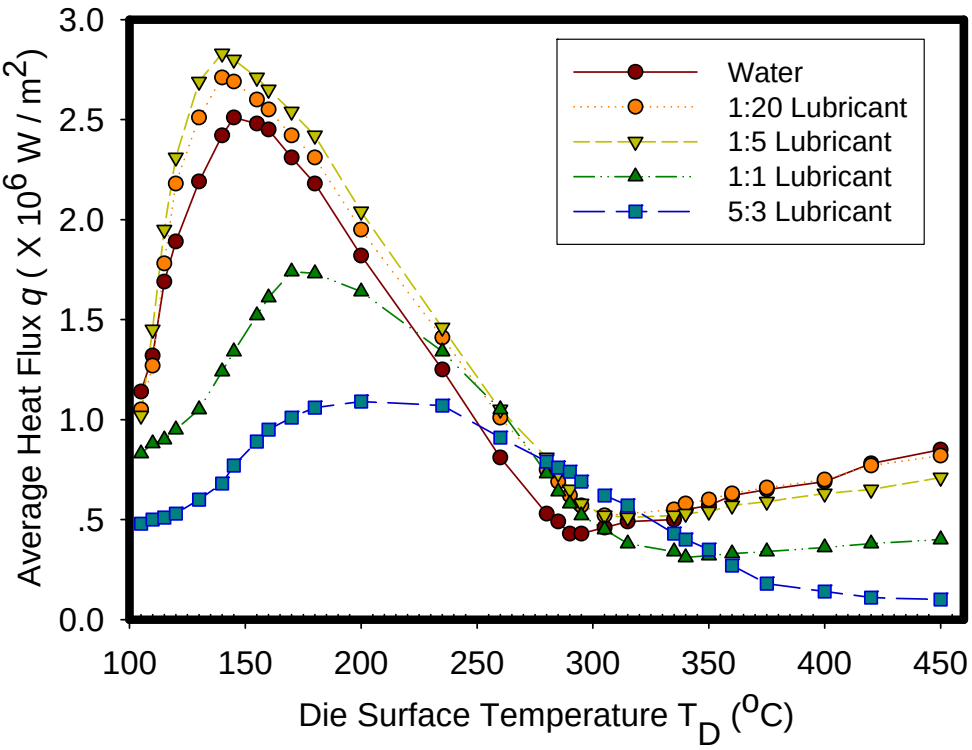

Figure E. 5: Measured average heat flux for water and lubricant with different dilution ratio at quasisteady state.

With a low dilution ratio, such as 1:20 and 1:5, CHF temperature is around 140°C which seems a few degrees lower than that for water. However, CHF temperature increases up to almost 200oC for both 1:1 and 5:3 lubricants (higher solid content). One possible explanation of the phenomena is that the fine

graphite particles in the liquid facilitate the generation of bubbles in the regime of nucleate boiling and enhance the vaporization rate, which lowers the CHF temperature below that of the water. However, when the dilution ration goes up the suspended particles become so dense that they start to retard the movement of the bubbles which bring heat and mass out of the liquid surface, and this effect overcomes the enhanced nucleating process.

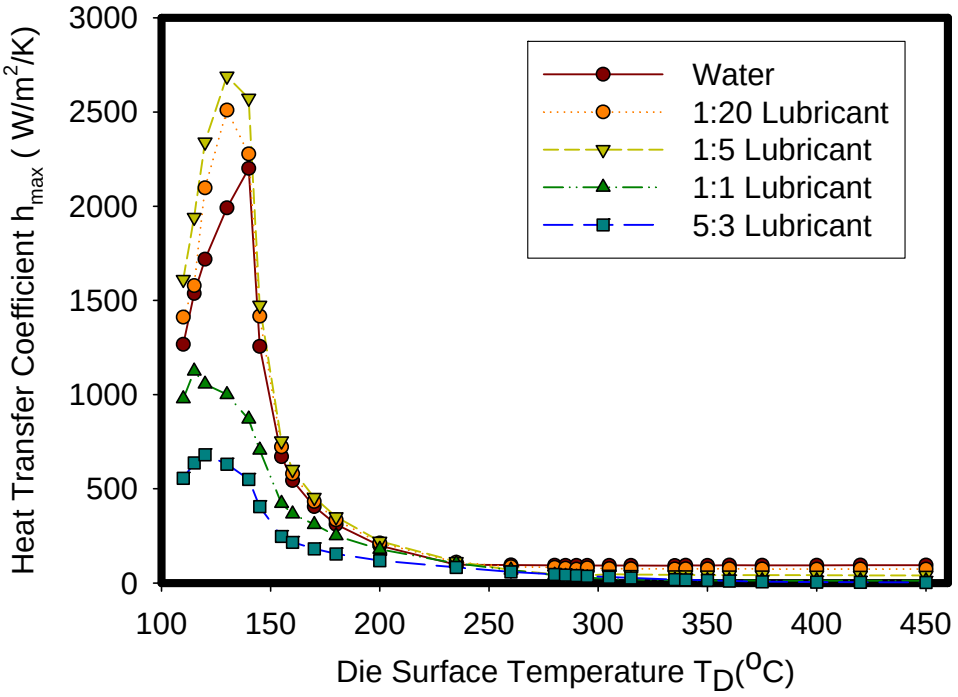

Figure E. 6: Heat transfer coefficient for lubricant mixtures with different dilution ratios.

Leidenfrost temperature increases as the dilution ratio increases from 1:20 to 5:3 while the Leidenfrost temperature of the water, 285^{o}C in the experiment, is lower than those of the all diluted lubricants. The Leidenfrost temperature is defined as the temperature where the droplet becomes completely separated from the heated die surface by an intervening vapor layer. A droplet with higher dilution ratio requires higher surface temperature to produce the critical vaporization rate to overcome the weight of the droplet and lift itself. This means a higher Leidenfrost temperature.

E.4.3 Heat Transfer and Dryoff

Fig. E.5 shows the heat transfer coefficient (HTC) between the heated droplet and the heated die surface. Lubricants with 1:20 and 1:5 dilution ratio present the largest heat transfer coefficient values when the die surface is below 200oC with highly dense lubricants showing relatively low heat transfer. The coefficient in the film boiling region, e.g. 0.34 W/m2/K for lubricant with 5:3 dilution ratio compared with that of the water (9.45 W/m2/K). As the die surface is heated to over Leidenfrost temperature and steam formation dominates, HTC becomes independent to the wall temperature as well as almost independent of dilution ratios and keep almost constant.

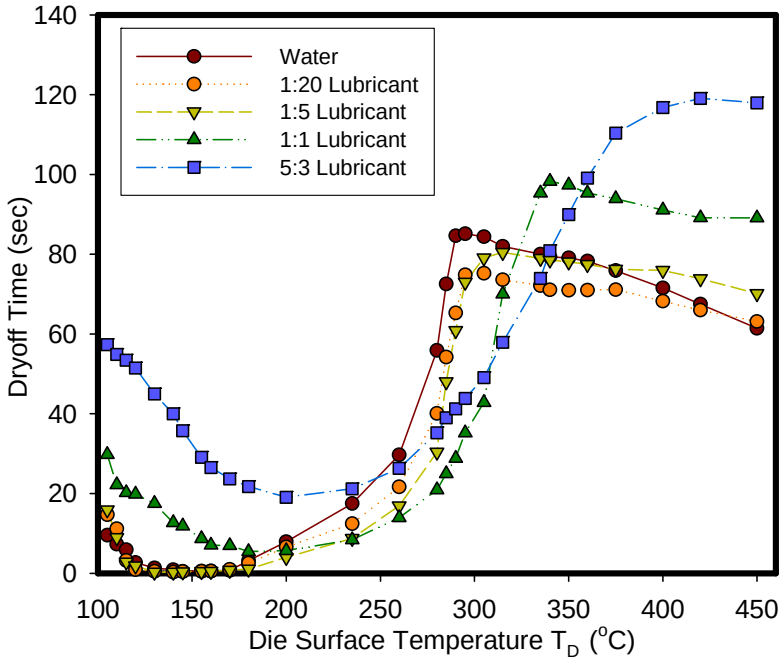

Figure E. 7: Measured dryoff time curves for water and lubricant with different dilution ratios.

The dryoff time, defined as the duration from placing a droplet on the surface to complete solid remained, is averaged from the measurements using stop watch and video image combined. As expected, the dryoff times are higher for lubricants with higher solid content because the overall heat flux is lower for less diluted lubricant than that for high diluted ones, Fig. E.6. It is interesting to note that between 150 to 250°C dryoff time is almost independent of dilution ratio and results based on pure water are sufficient.

E.4.4 Effect of Drop Dynamics on Heat Transfer

Experiments were carried out to quantify the effect of droplet and hot surface parameters such as droplet size, impact velocity and surface temperature were controlled variables in these experiments. Lubricant droplets with the diameters of 2mm, 3mm, and 4 mm were made to fall under their own gravity. Impact velocities were obtained between 10cm/s and 200 cm/s by changing the height "*h*" of the droplet generator. Non dimensional Weber number was used as it would enable the single droplet experiments to be applicable to lubricant sprays.

The following equations were derived from the regression fit of experimental results for the temperature range of 280 to 450 °C and for 100 to 280°C respectively.

$$h_{W1}(T) = 0.5279 We_n^{\,0.691} e^{9.079\times10^{-4} We_n} + h_{quasi}(T) \qquad \text{(E.1)}$$

$$h_{W2}(T) = 1.5347 We_n^{0.35} + h_{quasi}(T) \quad \text{(E.2)}$$

where h_{W1} and h_{W2} are heat transfer coefficients between droplet and die surface for each of the temperature range, We_n the Weber number of the normal velocity element, and h_{quasi} the heat transfer coefficient at quasi-steady state shown in Fig. E.4. The first terms in Equation (E.1) and (E.2) define the contribution of droplet characteristics, while the second terms introduce the effects of surface temperature on the heat transfer. The Weber number is calculated as follows:

$$We_n = \rho v_n^2 D / \gamma \quad \text{(E.3)}$$

where ρ is the density of the water, γ the surface tension of the liquid, v_n the normal velocity of the drop.

E.5 Application of Single Droplet Relations to Sprays

E.5.1 Methodology for Plain-orifice Atomizers

To extend the single droplet approach to more complex spray systems where the droplet sizes and the impact velocities vary in magnitude and also spatially, the following assumptions are made: (a) The spray system is a plain orifice atomizer, most common in liquid spraying, in which the jet break up into droplets is promoted by an increase in flow velocity or air pressure. (b) The results of the large single droplet - low velocity experiments can be applied to the small droplet-high velocity application using the "similarity approach". In this case Weber numbers (We= momentum force/ surface tension force) will be used for this extrapolation. (c) The range of droplet sizes present in the spray can be represented by the Sauter Mean Diameter (SMD). With the above assumptions, the average diameter of the droplet in a spray, or SMD, can be calculated using relation derived by [Pasandideh-Fard, M., 2002]:

$$D = SMD = 3.08 \nu_L^{0.385} (\gamma \rho_L)^{0.737} \rho_A^{0.06} \Delta P_L^{-0.54} \quad \text{(E.4)}$$

where ν_L is the kinematic viscosity of the liquid, ρ_L the density of the liquid, ρ_A the density of the air, and ΔP_L the pressure drop across the nozzle. This relation applies to the plain orifice atomizer in which only pressure drop across the nozzle is used to atomize the liquid jet. The pressure drop ΔP_L in Equation (E.4) can be reversely calculated by:

$$\Delta P_L = \left(\frac{Q}{C} \right)^2 \quad \text{(E.5)}$$

where Q is the flow rate and C a constant representing the nozzle geometry.

The average of normal velocity of the droplets in the spray can be estimated as:

$$\bar{v}_n = \frac{Q}{A} \quad \text{(E.6)}$$

where A is the discharge orifice area. Introducing Equations (E.4), (E.5) and (5.6) into (E.3), the

average Weber number We_n is calculated for the spray and this is used in Equations (E.1) and (E.2) to calculate the heat transfer coefficient and flow rate of a spray at a specific surface temperature.

E.5.2 Case Study: Hot Forging Lubrication

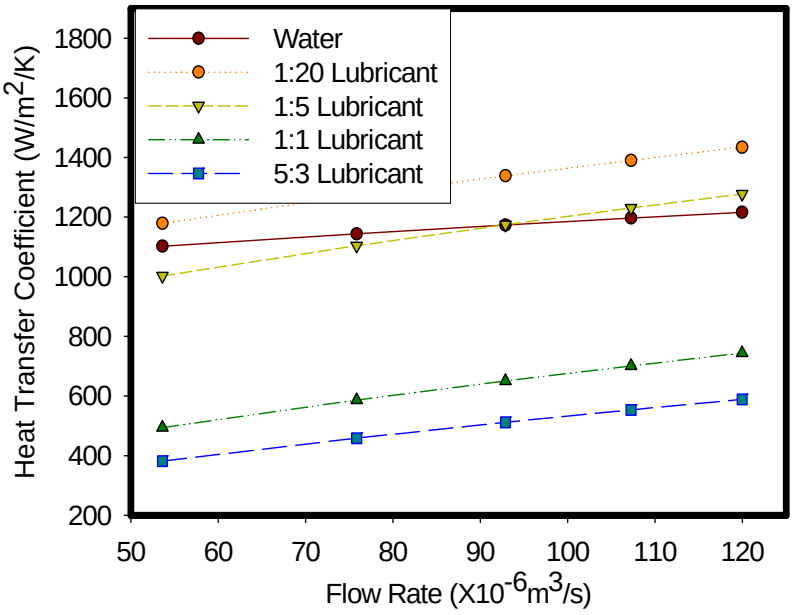

Figure E. 8: Predicted heat transfer coefficient for lubricant sprays with different dilution ratios.

The above relations are used to predict the heat transfer coefficients for the lubricant spray and the die surface temperatures used in the pure water experiments carried out by [Bariani et al., 2002]. In their study, Bariani et al. generated sprays by atomizing water from a plain-orifice atomizer. Three types of nozzles were used in their experiments [Bariani et al., 2002] and their constant C, defined in Equation (E.5), for these are determined as: $3.7378\times10^{-8} m^3 s^{-1} Pa^{-1/2}$, $6.7040\times10^{-8} m^3 s^{-1} Pa^{-1/2}$ and $1.1991\times10^{-7} m^3 s^{-1} Pa^{-1/2}$. Assuming that the droplets do not interact with each other and the impacting area of each droplet on the die surface does not overlap, the transient heat transfer coefficient of the spray can be calculated using Equations (E.1) and (E.2). If it is further assumed the heat transfer coefficient can be averaged over time as the temperature of the die drops from 400°C to 100°C, the overall spray heat transfer coefficient can be predicted. This is plotted for different dilution ratios and flow rates in Fig.E.6. Since the results in[Bariani et al., 2002]] do not distinguish the nozzles types, one can only compare the magnitude and the trend of the calculated heat transfer coefficient. [Bariani et al., 2002] report heat transfer coefficients for Zone 2 to 4 in the range of 1800 to 1107 W/m2K for pure water. This agrees well with results in Fig. E.6 for water spray. Zone 1 directly under the spray in [Bariani et al., 2002] has high water accumulation and hence cannot be modeled by the proposed single droplet methodology.

E.6 Bouncing, Wetting and Breaking up (single Droplets)

The experimental set up for single droplet experiments consisted of a droplet generator mounted on a fixture to create droplets, a hot die steel surface heated by band heaters and a temperature measurement system using thermocouples. The setup is shown in Fig. E.2. A camcorder and a high speed camera took pictures of the droplet formation and its kinetics during impact on the heated surface. The images were later sent to computer for imaging processing to measure deposited film dimensions. Before the experiment, graphite-based lubricant with 54% solid content (weight %) was diluted by distilled water to 5:3, 1:1, 1:5, and 1:20 dilution ratios, which are volume ratio of lubricant to water. Lubricant droplets were generated in diameters of 2 to 4 mm, and made to fall under their own gravity. Impact velocities were obtained between 10 and 200 cm/s by changing the height of the droplet generator. The flat H-13 steel surface was finished to roughness Ra 50 micro-inch (or 1.25 μm) and heated by a band heater whose temperature was adjustable from room temperature to 450^{o}C. Temperatures during droplet impact were measured by fast response thermocouples (response times≤2ms) embedded 0.5, 1.0 and 1.2 mm beneath the surface of the die.

When a droplet impinging on a heated die surface with an initial velocity, it can spread on the surface, break up to smaller droplets, or be rebounded from the surface [Bernardin J.D., 1997; Rein, M., 1993; Ko Y.S., 1996; Bolle L., 1981; Doege, E., 2004], similarly as in droplet impacts occurring under conditions without phase-change. Not only dynamical parameters, particularly nondimensional Weber number ($We = \rho v^2 d_0 / \gamma$), but also thermal characteristics determine which result of the impact will be. Weber number *We* is considered as the ratio of inertia force to the surface force, where ρ is the density of the droplet liquid, v the normal component of impact velocity, d_0 the initial diameter of the droplet before impact, and γ the surface tension of the droplet liquid. Without phase-change taking place, droplets will spread, and sometimes rebound when the Weber number is small. Above a critical Weber number an impact results in a disintegration of the drop, i.e., in a splash. The critical Weber number of splashing depends on the roughness of the surface and also on the Reynolds number. Actually, limiting conditions of splashing without phase-change are often expressed in terms of the Ohnesorge number instead of the Weber number. However, in studies on the interaction of droplets with hot walls normally a dependence on the Weber number is considered. We will therefore stay with the Weber number in the following.

When drops impinge on a wall having a temperature that is above the saturation temperature of the liquid, the wall temperature becomes another important variable - in addition to the Weber number. The importance of further thermal parameters or of other nondimensional numbers relating to thermal aspects has rarely been considered.

Therefore, in our experimental study of droplet impact on hot die surfaces both the Weber number and the wall temperature have been changed with the other variable at a fixed value. Waters and also lubricant with different dilution ratios were used in the experiments. The experimental setup remained the same illustrated in Fig. E.2.

In this study, regimes characteristic of droplets with different dilution ratio were mapped in a

Weber number (*We*) versus die surface temperature plots. As shown in Fig. E.7 the safe lubricant zone (constrained by bubbling, bounce off, Leidenfrost temperature and spreading) increases as the solid content (less dilution) increases. The experimental results are summarized in Fig. E.7 (a), (b), (c) and (d) for lubricants with four different dilution ratios. These characteristics are compared with those of water. When Weber number is larger than a critical number, the droplet will always breakup to smaller droplets. It is observed that all critical Weber numbers of the lubricants are larger than that of the water. The more diluted the lubricant is, the closer the critical Weber number to that of the water. This may be caused by the high viscosity of the lubricant which decreases another important nondimensional parameter, Reynolds number $\mathrm{Re} = \rho V d_0 / \mu$, where μ is the dynamic viscosity of the droplet liquid. For E:7 lubricant, the Reynolds number drops below the order of 10, which means the viscous dissipation effect cannot be neglected. Part of the kinetic energy of the impacting droplet has to be used to overcome the viscous shear force. Therefore, larger Weber number is expected to contribute to the increased surface energy due to breakup and viscous dissipation than that of the water droplet.

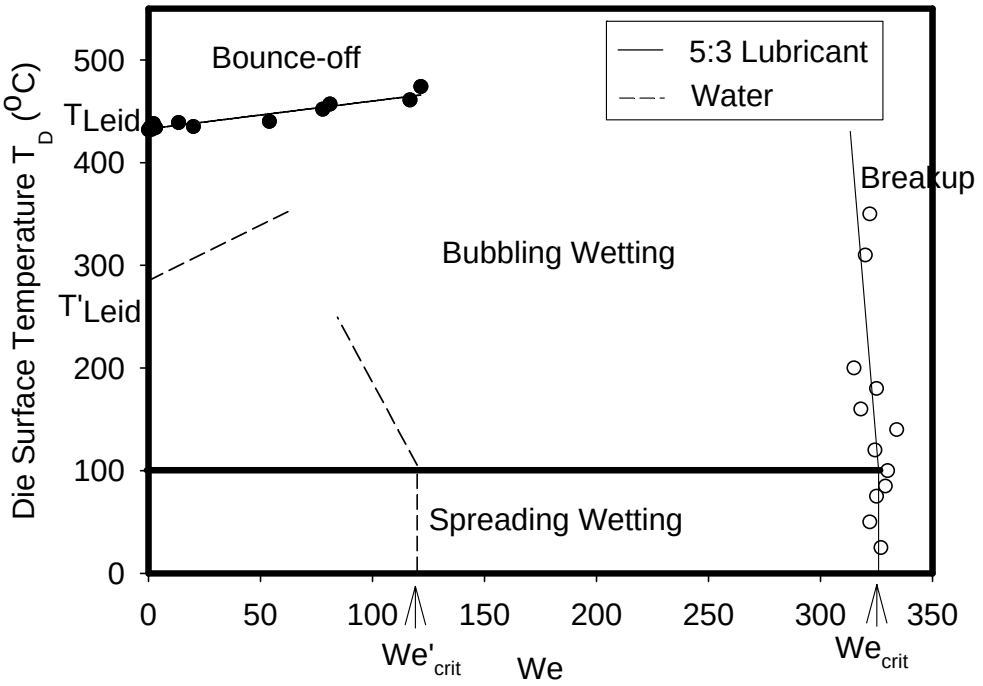

(a)

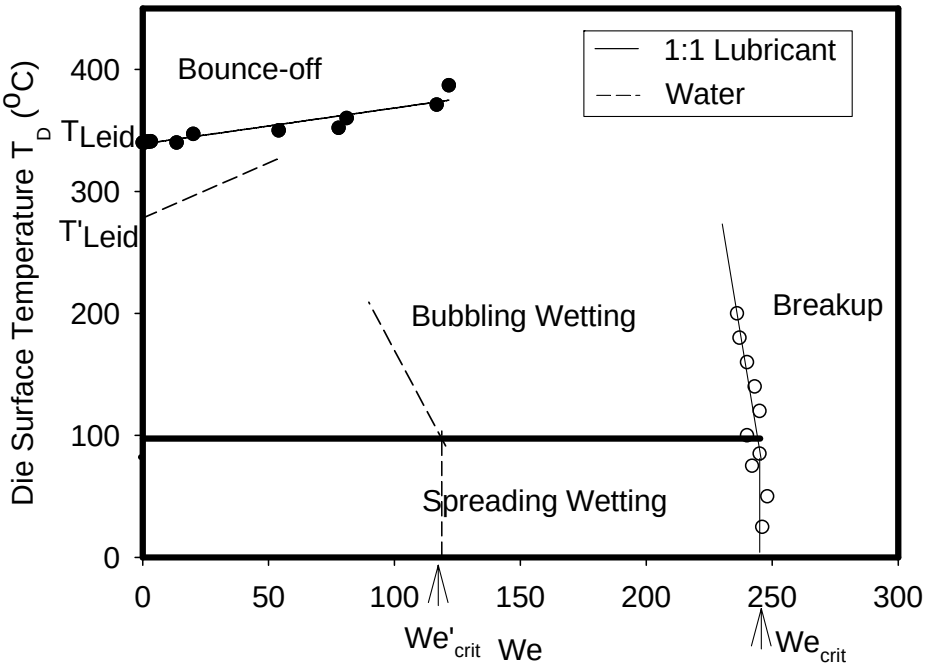
1:1 Lubricant
Water
Bounce-off
Bubbling Wetting
Breakup
Spreading Wetting
Die Surface Temperature T_D (^oC)
T_{Leid}
T'_{Leid}
400
300
200
100
0
0
50
100
150
200
250
300
We'_{crit}
We
We_{crit}

(b)

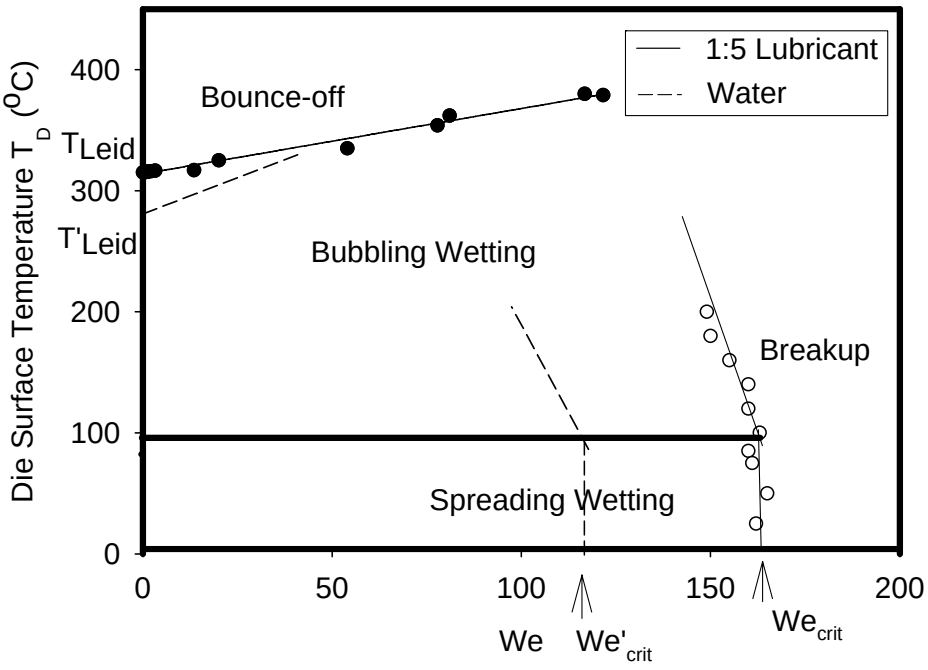
1:5 Lubricant
Water
Bounce-off
Bubbling Wetting
Breakup
Spreading Wetting
Die Surface Temperature T_D (^oC)
T_{Leid}
T'_{Leid}
400
300
200
100
0
0
50
100
150
200
We
We'_{crit}
We_{crit}

(c)

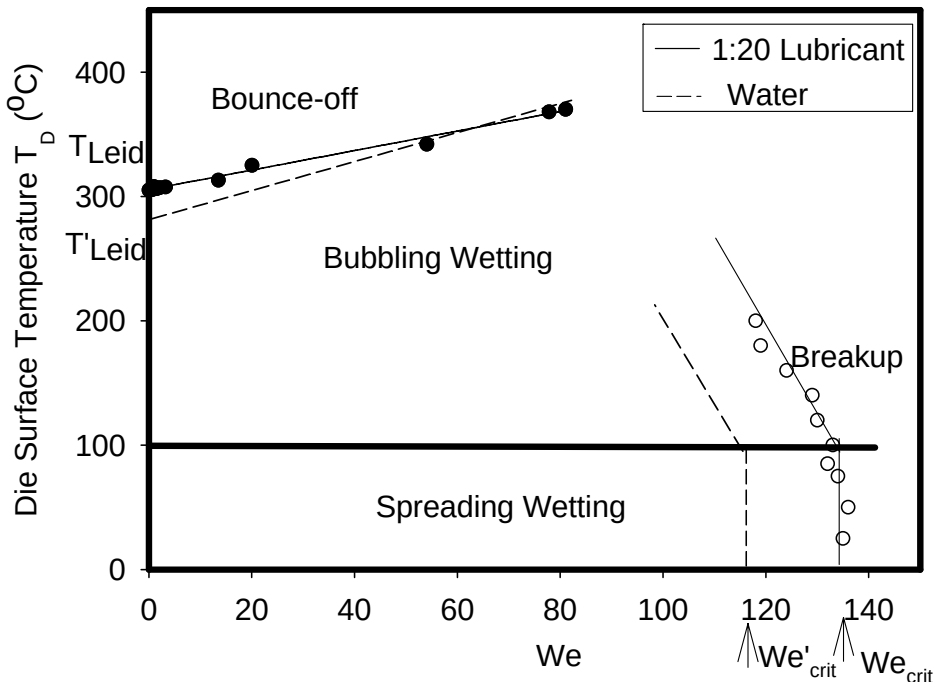

Figure E. 9: Regimes of different phenomena of a lubricant droplet impinging on heat die surface comparing with water. (a). 1:20 Lubricant, (b). 1:5 Lubricant, (c). 1:1 Lubricant, (d). 5:3 Lubricant.

It is observed in Fig. E.7 that the Leidenfrost temperature relating to a droplet with an impacting velocity is greater than the quasi-state Leidenfrost point shown in Fig. E.7 i.e., the Leidenfrost point rises with the increasing of the velocity for a given droplet. This is because the bounce-off is caused by the high pressure of the vapor generated between the droplet and die surface. Now, in addition to balancing the gravity of the droplet, the direction of its momentum also needs to be changed, and this requires high surface temperature to generate faster evaporation rate. This phenomenon is the dynamic analogue to film boiling and has therefore been called a dynamic Leidenfrost phenomenon. Fig. E.7 also shows that the breakup is enhanced with decreased critical Weber number when the die surface is heated above boiling temperature. The reason behind is obvious that the fast boiling initiated by the contact of the droplet and die surface generates dynamic pressure which helps to blow apart the droplet. However, this effect is not evident for the lubricants with high dilution ratio. The stable evaporation rate of the lubricant which is independent of temperature may contribute to this phenomenon.

E.7 Heat Flux During Lubricant Spraying

The spray cooling test was carried on a 20” diameter, 2” thick hot plate of H13 steel with the aid of Acheson fix nozzle 682 spray system. A straight nozzle pipe with the inner diameter 0.375” is chosen for spray. A 7100W ceramic radiant heater supported by paralleled frame was used to heat up this steel plate to temperatures as high as 350^{o}C. Fifteen thermocouples were installed 0.02” beneath the hot plate surface at different horizontal locations from the center of the hot

plate. Temperature was measured at various spray heights H (14, 17 and 20”), liquid pressures P_l (45, 60 and 75psi), and dilution ratios (water and 1:20 dilution). Temperatures were measured at selected positions (P1=0.0”, P2=1.5”, P3=2.5” and P4= 3.5”).

Temperature history data was continuously recorded and logged into computer through data acquisition system. Selected results from these experiments are included in Fig. 6.4. From the plots in this figure, the following is observed:

- The instant heat transfer coefficient (HTC) peak happens after spray starts (0.5s to 1.0s), reaches around 30000 W/m^{2}K and drops to 10000 W/m^{2}K gradually for the location closest to the center of the spray. This drop off may be due to the heat conduction from the neighboring locations at longer times. The temperature drop at this location is also the highest. However as the spraying continues to 2s the heat transfer at farther locations catch up with an average HTC around 10 to 15 KW/m^{2}K for most points for 1:20 dilution ratio and 60psi air pressure, Fig. 6.4(a).
- For liquid pressure at 45psi, 60psi, and 75psi, the mass flow rates of water are rated at 0.618GPM, 0.736GPM, and 0.830GPM respectively, when air pressure is fixed at 75psi. At 45 and 60 psi HTC increases with water flow rate but at higher 75 psi the water atomizes and lower heat transfer is observed, Fig. 6.4(b). The reasons behind this anomaly needs further study.

- Plots of temperature history and HTCs for different spray height imply the opposite effects of droplets velocity on HTC, Fig. 6.4(c). At higher heights the impact velocities are high and the droplets quickly fly away hot plate when they hit the hot plate. This bouncing off phenomenon is also observed in the single droplet experiments. After 0.5 seconds the HTC for 20” height catch up as a liquid layer is now present and the droplets are plashing into this.

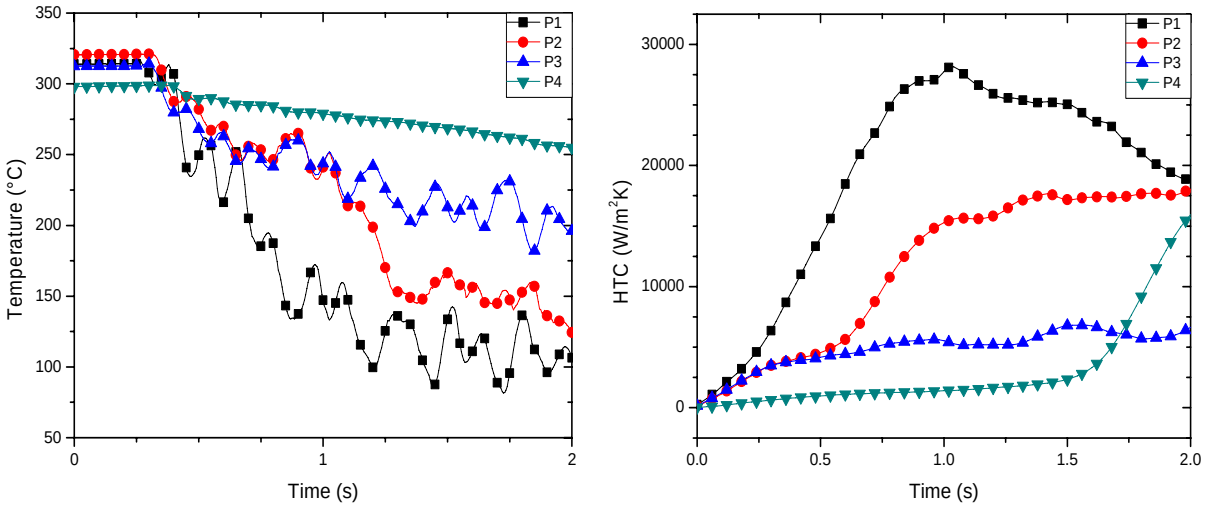

(a). Different thermocouple locations: 1:20 dilution ratio, Pl = 60 psi, H = 14”.

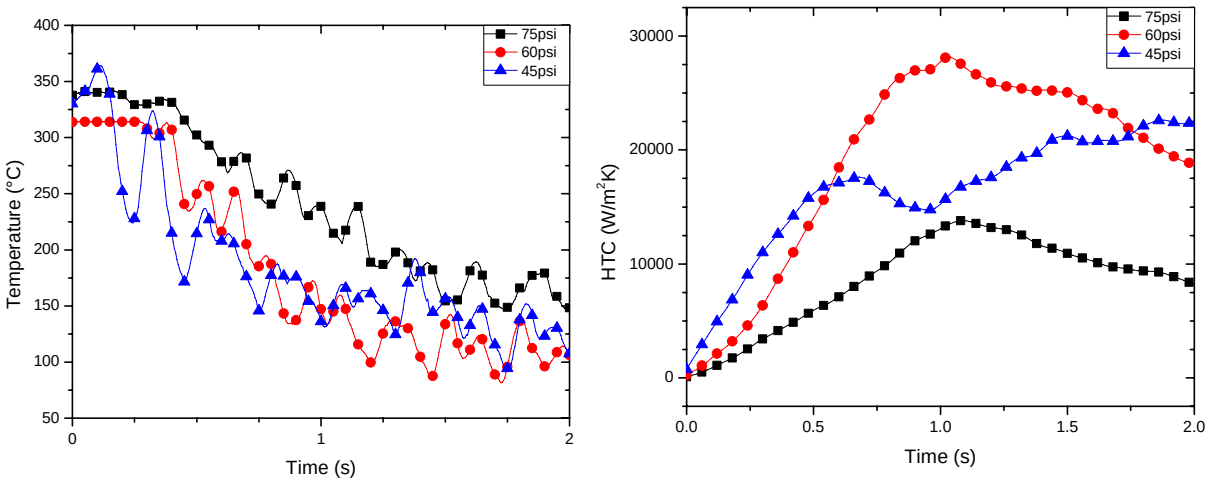

(b). Different liquid pressures: 1:20 dilution ratio, at Point P0 (H = 14").

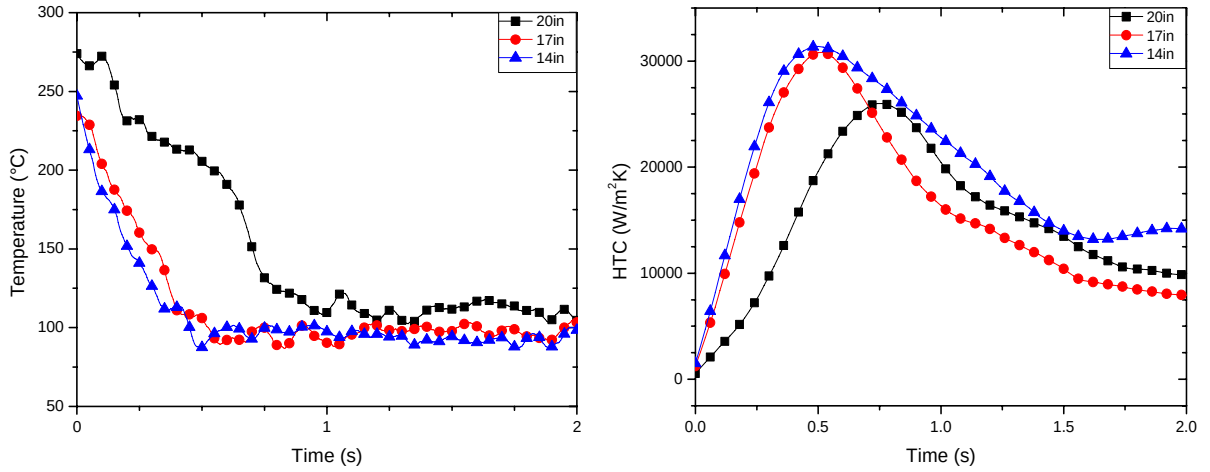

(c). Different heights: 1:20 dilution ratio, at Point P0 (Pl = 45psi)

Figure E. 10: Temperature history and heat transfer coefficients in the first 2 seconds.

E.8 Summary of Investigation

This chapter first outlines the problem of forging spray lubrication and the relations between the spray parameters and the forging process parameters. Then it describes the comprehensive research approach adopted at CEFT to model, predict and control the phenomena of pollution, heat transfer and lubricant deposition. This approach includes single droplet experiments to investigate fundamentals of the deposition process, and the spray experiments to investigate the relationship between spray parameters and the heat transfer coefficients. Based on the preliminary results the following conclusions can be reached:

- Results from single droplet test show that both Weber number *We* and die surface temperature play important role on the lubricant wetting on the die.

- Low dilution ratios (with higher solid contents) provide for greater lubricant process

window. However, it is possible that lower dilution my also provide lower graphite air pollution due to higher Leidenfrost temperature (die surfaces below 430^{o}C) may not experience bounce off. Also the lower dilution ratios delay the break-up of the lubricant film to higher Weber numbers (We > 325) due to higher viscous energy that stabilizes the bubbles.

- The spray test results show that both liquid pressure and spray height increase kinetic energy, cause droplets bouncing off from the hot plate, and hinder spray cooling. This is a reverse of the role of flow flux density (flow rate) in increasing the heat flux. This indicates that for lubricant sprays, the nozzle design and atomization will play a major role in controlling the different physical ad thermal phenomena. This is the goal of the ongoing study.

APPENDIX - F

LUBRICANT SPREAD ON HOT DIE SURFACES: MODEL DEVELOPMENT AND VALIDATION

This chapter proposes an isothermal numerical model based on the VOF finite difference approach for investigating the dynamics and spread of lubricant droplet on hot die surface. The lubricant properties for this model are calculated in simple capillary experiments. This model is validated by comparing with spreading results from single droplet experiments at different lubricant dilution ratios (lubricant properties) and droplet kinetics. It is found that the isothermal assumption is valid for surface temperatures where no-steam forms, less than the Leidenfrost temperatures. It is also found that a simple linear relationship exists in the logarithmic scale between the spread factor and the Weber number for dilution ratios less than equal to unity (for dilute suspensions).

F.1 Introduction

In the hot forging processes, the dies are lubricated and cooled by spraying dilute water based lubricants on the heated die surfaces. This spray is produced by atomizing lubricants into small droplets using spray devices with pressurized air. The lubricant is often a fine suspension of fine graphite particles in water, with surfactants and binders added to aid in the spreading and formation of adherent lubricant films. In addition, this lubricant spray is used to maintain the thermal conditions of the die surface suitable for metal flow in deep cavities. As the phenomena of spraying, spreading and film formation are poorly understood, the lubricant is often applied in large quantities resulting in excessive cooling of the surface, and excess graphite in the die cavities, and the atmosphere. While excessive chilling of die surfaces causes poor metal flow and filling of die cavities, excess graphite leads to air and ground water pollution. Consequently, understanding the ideal spraying conditions for lubricant spread and film formation has become critical to both the manufacturing and lubrication community.

The important factors governing the mechanics and thermodynamics of the spray deposition can be categorized into three groups: those related to the hot die surface, those related to the lubricant properties, and those related to the spray characteristics. The factors related to die surface include the initial surface temperature, its roughness, its geometry (cavity design) and surface treatments (such as diffusion treatments or coatings). Important lubricant properties include surface tension and viscosity. Lastly, the spray characteristics involve droplet size, droplet velocity, dilution ratio (or solid content) and, spray cone angle and nozzle height. Composition of the lubricant and the selection of the spray parameters are often determined by the lubrication and cooling needs of the intended application.

The primary objective of this study is to develop a model that captures the mechanics of lubricant spread as the spray droplets impact the hot die surface. This spread governs the thickness of the resultant film and the heat transfer from the hot die surface. Such a model would

enable optimal design of the lubrication process and consequently, significant reduction in the graphite related pollution.

This phenomenon of wetting and spreading in spray lubrication in hot forging is difficult to study and model due to the following reasons:

- The spray consists of very fine droplets with random distribution of size (tens to hundreds of microns in diameter) and velocity (several to tens meters per second). A methodology must be adopted to quantify the spray characteristics.
- The lubricant properties and dilution ratios (amount of water added to dilute the liquid) affect the physics of the droplet mechanics. They vary considerably from application to application. This model must include these properties and parameters.
- The physics and thermodynamics of the spreading phenomenon are complicated by its transient and evolving nature. The lubricant droplet impacts the hot die surface at temperatures between 250 to 450^{o}C. At these temperatures steam forms first, followed by nucleate boiling, convective cooling and dry-off (evaporation). It may be very difficult, if not impossible, to develop a single model that can represent all these phenomena.

In order to make the problem solvable, it was decided to make several assumptions and limit the scope of the model. First, it was decided to represent the spray by the Sauder Mean Diameter (an average diameter for log-normal distribution). This assumption will permit the spray to be represented by single droplet experiments. Second, it was decided to use non-dimensional numbers, using the similarity principle, to quantify the physics of the process. These numbers will enable the simple model to represent many physical conditions (lubricant properties, droplet diameters, impact velocities etc.). Third, it was decided to limit this study to lower surface temperatures where two phase flow is not present. Finally, it was decided to develop a numerical model that will permit application of the governing equations to complicated geometries and boundary conditions.

The phenomenon of a droplet impact on hot surface has been studied by many researchers since the classical work of Leindenfrost. Most of the previous work is on water droplets and the heat transfer resulting from the evaporation and boiling of the liquid. The study of the droplet spread during impact has applications to painting, thermal spray coatings, rapid solidification, lubrication etc. Earlier studies were mainly experimental with high speed or flash photography used to capture droplet dynamics [Engel, O.G., 1955; Savic, P., 1955, 1958; Inada, S., 1983; Toda, S.1974; Akao, F., 1980]. An interesting study was carried out by Makino and Michiyoshi [Makino, K., 1984] with water droplets on heated surfaces (350^{o}C). They found that for temperatures below Liedenfrost (<200^{o}C), the droplet spread factor became independent of surface temperature. In 1991, Chandra and Avedisian [Chandra, S., 1991] used flash photography to capture dynamics of n-heptane droplet (about 1.5 mm) on heated (24 to 260^{o}C) stainless steel surface at. Weber numbers kept fixed at 43. They also found that for lower temperatures, below Leidenfrost point, the spread factor became independent of surface temperature. Recently, Manzello and Yang [Manzello, S.L., 2002] studied the impact dynamics of water diluted sodium acetate trihydrate

droplet (diameter 2.7 mm) on a stainless steel heated surface (from 20 to 340^{o}C). They confirmed the previous findings that below 230 ^{o}C (below Leidenfrost point) the droplet spread did not depend on the surface temperature. From these studies with water and other liquids it can be concluded that in the nucleate boiling and convection boiling regimes, the droplet spread is mainly governed by the droplet dynamics and independent of surface temperature and heat transfer. This may be due to small dry-off times (high heat transfer) at these temperatures with no-steam formation. This results in inertia and viscous forces to dominate the droplet spread.

Development of numerical models for droplet impact on a solid surface has also received much attention. For example, Harlow and Shannon [Harlow, F.H., 1965] were the first to use Marker-and-Cell (MAC), a finite differential method, to solve momentum equations for droplet impact on a surface. They neglected surface tension and viscous effects for the simple of the problem. However, this assumption only applies at the early stage of impact when inertial effects dominate. Trapaga and Szekely [Trapaga, G., 1991] numerically modeled the deformation process of a liquid-metal droplet on impact with a solid plate using combined MAC and Volume of Fluid (VOF) methods to track the droplet surface changes. Bussmann et al. [Bussmann, M, 1999] developed a three-dimensional fluid flow model to simulate water droplet impact on an inclined substrate and a geometrical step; not considering heat transfer and phase change during droplet impact. Their model was based on RIPPLE, a 2D fixed-grid Eulerian code developed specifically for free surface flows with surface tension. They modeled surface tension as a volume force exerted on the fluid near the free surface. The temporal variation of contact angles at the leading and trailing edges of the droplet was considered in their studies. Their simulation results agreed with their photographic data. Fluid dynamic and solidification of the molten tin droplet impact on a flat stainless plate was modeled by Pasandideh-Fard et al [Pasandideh-Fard, M., 2002]. They applied the numerical solution of Navier-Stokes and energy equations to model the droplet deformation and solidification, and heat transfer in the substrate. The heat transfer coefficient at the droplet-surface interaction was evaluated by matching the temperature calculated numerically from the model with measurements. They concluded that the effect of solidification on droplet impact dynamics was negligible if the factor $\sqrt{Ste/\Pr} << 1$, where Ste is Stefan number ($Ste = C_p(T_m - T_{w,0})/H_f$), and Pr is Prandtl number ($\Pr = \nu/\alpha$). Pasandideh-Fard et al. [Pasandideh-Fard, M., 2001] also studied the impact of droplet on a stainless steel surface which was heated from 50^{o}C to 120^{o}C, a controlled temperature range low enough to prevent boiling in the droplet. VOF code was applied to calculate the shape of droplet and substrate temperature during impact. The results of experiments and numerical calculations agreed well. According to their results, they concluded that for fixed Reynolds number Re cooling effectiveness increases with Weber number *We*.

Other researchers utilized deforming meshes instead of fixed-grid techniques to numerically solve their models. Fukai et al. [Fukai, J., 1993] presented a finite element technique to model the droplet spreading process. All the factors in momentum conservation equations, such as inertia, viscosity, gravity and surface tension, were considered in their model. Two liquids, water and liquid tin, were utilized in their simulation based on the Lagarangian description. Significant differences of the flow field were observed for droplets of these two liquid. Zhao et al. [Zhao, Z., 1996] extended Fukai's study to model both fluid dynamics and heat transfer during the impact of

liquid droplet on a substrate. However, only heat transfer of convection and conduction were included and phase change phenomena were ignored to facilitate the modeling of heat transfer. They concluded that the maximum splat thickness might occur at the periphery of the splat where mass accumulation was observed. The heat transfer results showed that temperature at the spreading front is substantially lower than the temperature at the splat center in a molten metal droplet.

In this chapter, an isothermal finite difference VOF based numerical model is proposed for studying droplet dynamics and spread. The isothermal assumption is based on the demonstration by previous researchers that for temperatures lower than Leidenfrost, the droplet spread is independent of surface temperature. Hence, heat transfer plays a minor role in the mechanics of spread in this temperature range where the heat transfer is very high and dry-off times short. The physical constants for this model are determined by simple single droplet experiments. The model is applied to different lubricant dilution ratios, surface temperatures and range droplet kinetics (Weber numbers). The predictions of the model are validated by comparing with results of single droplet experiments.

F.2 Theoretical Analysis

The complexity of the fluid dynamical aspects of droplet impact on a solid surface is exemplified by the extreme deformation of the droplet surface occurring within very short time scale. The model presented here simulates the impact of a liquid droplet on a solid from the moment that the lubricant droplet comes into contact with the die surface and proceeding until the droplet becomes rest after the spreading process is completed or it is terminated at any desired time. The numerical solution based on VOF method is subsequently presented.

F.2.1 Governing Equations

As shown in the Fig. 3.1, for the ease of problem description and boundary condition writing, the cylindrical coordinates are used to define the conservation equations. Any point of the droplet can be described by *r, z,* and θ, which are the radial, axial and azimuthal coordinates.

- **Conservation of Mass**

The equation of mass balance for cylindrical coordinates can be written as:

$$\frac{\partial \rho}{\partial t} + \frac{1}{r}\frac{\partial}{\partial r}(\rho r v_r) + \frac{\partial}{\partial \theta}(\rho v_\theta) + \frac{\partial}{\partial z}(\rho v_z) = 0 \qquad \text{(F.1)}$$

For an isothermal condition, the following assumptions can be taken for a initially spherical droplet impact on a solid surface:

I. Constant liquid density ρ.
II. The velocity at the azimuthal direction v_θ is always zero.

Then Equation (F.1) reduces to:

$$\frac{1}{r}\frac{\partial}{\partial r}(rv_r)+\frac{\partial v_z}{\partial z}=0 \tag{F.2}$$

where v_r is the velocity at the radial direction, v_z the velocity at the axial direction.

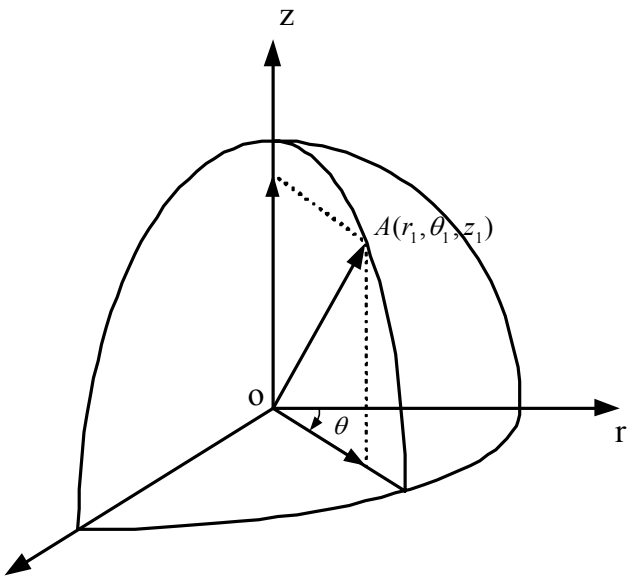

Figure F. 1: The Cylindrical Coordinate description of lubricant droplet on a solid surface.

- **Conservation of Momentum**

The general form of linear momentum equations in cylindrical coordinates is shown as follows.

$$\begin{aligned}&\rho\left(\frac{\partial v_r}{\partial t}+v_r\frac{\partial v_r}{\partial r}+\frac{v_\theta}{r}\frac{\partial v_r}{\partial \theta}-\frac{v_\theta^2}{r}+v_z\frac{\partial v_r}{\partial z}\right)\\&=-\frac{\partial p}{\partial r}+\left(\frac{1}{r}\frac{\partial}{\partial r}(r\tau_{rr})+\frac{1}{r}\frac{\partial \tau_{r\theta}}{\partial \theta}-\frac{\tau_{\theta\theta}}{r}+\frac{\partial \tau_{rz}}{\partial z}\right)+\rho b_r\end{aligned} \tag{F.3a}$$

$$\begin{aligned}&\rho\left(\frac{\partial v_\theta}{\partial t}+v_r\frac{\partial v_\theta}{\partial r}+\frac{v_\theta}{r}\frac{\partial v_\theta}{\partial \theta}+\frac{v_r v_\theta}{r}+v_z\frac{\partial v_\theta}{\partial z}\right)\\&=-\frac{1}{r}\frac{\partial p}{\partial \theta}+\left(\frac{1}{r^2}\frac{\partial}{\partial r}(r^2\tau_{r\theta})+\frac{1}{r}\frac{\partial \tau_{\theta\theta}}{\partial \theta}+\frac{\partial \tau_{\theta z}}{\partial z}\right)+\rho b_\theta\end{aligned} \tag{F.3b}$$

$$\rho\left(\frac{\partial v_z}{\partial t}+v_r\frac{\partial v_z}{\partial r}+\frac{v_\theta}{r}\frac{\partial v_z}{\partial \theta}+v_z\frac{\partial v_z}{\partial z}\right)$$
$$=-\frac{\partial p}{\partial z}+\left(\frac{1}{r}\frac{\partial}{\partial r}\left(r\tau_{rz}\right)+\frac{1}{r}\frac{\partial \tau_{\theta z}}{\partial \theta}+\frac{\partial \tau_{zz}}{\partial z}\right)+\rho b_z \qquad \text{(F.3c)}$$

Dropping the terms including azimuthal direction and considering only gravity as the body force, we can rewrite the momentum equations as:

$$\rho\left(\frac{\partial v_r}{\partial t}+v_r\frac{\partial v_r}{\partial r}+v_z\frac{\partial v_r}{\partial z}\right)=-\frac{\partial p}{\partial r}+\left(\frac{1}{r}\frac{\partial}{\partial r}\left(r\tau_{rr}\right)+\frac{\partial \tau_{rz}}{\partial z}\right) \qquad \text{(F.4a)}$$

$$\rho\left(\frac{\partial v_z}{\partial t}+v_r\frac{\partial v_z}{\partial r}+v_z\frac{\partial v_z}{\partial z}\right)=-\frac{\partial p}{\partial z}+\left(\frac{1}{r}\frac{\partial}{\partial r}\left(r\tau_{rz}\right)+\frac{\partial \tau_{zz}}{\partial z}\right)+\rho g \qquad \text{(F.4b)}$$

where p is the pressure, τ_{ij} the stress normal to i direction and pointing to j direction.

F.2.2 Initial and Boundary Conditions

It is very important to correctly define the initial and boundary conditions before we go further to numerically solve the equations listed above.

When $t=0$, $v_r=0, v_z=V_0, and\ p=p_0+\frac{2\gamma}{R_0}$, (F.5)

where V_0 is initial impact velocity, p_0 the ambient air pressure, γ the surface tension of the lubricant, and R_0 the initial radius of the droplet.

When $t=0$, $\left(z-R_0\right)^2+r^2=R_0^2$, or $r=\sqrt{2zR_0-z^2}$, $0\le z\le 2R_0$ (F.6)

At $r=0, v_r=0, \frac{\partial v_z}{\partial r}=0$ (F.7)

At $z=0, v_r=0$ and $v_z=0$, (F.8)

Considering the viscosity of the ambient air is much lower than that of the lubricant liquid, the tangential stresses at the free surface can be neglected and set to zero at the free moving surface, that is:

$$\tilde{\tilde{\tau}}=0 \qquad \text{(F.9)}$$

This means that all velocity derivatives that involve velocity components outside the surface are set to zero.

$$\frac{\partial v_r}{\partial r} = 0 \; ; \; \frac{\partial v_z}{\partial z} = 0 \; ; \; \frac{\partial v_r}{\partial z} = 0 \; ; \text{ and } \frac{\partial v_z}{\partial r} = 0 \qquad \text{(F.10)}$$

Thus, the boundary condition should only represent the balance between the pressures and the surface tension stresses. The force exerted on the moving surface is sketched in the Fig. F.2. In Fig. F.2, $\hat{n}$ is the unit vector normal to the droplet surface, p_0 the ambient pressure, p the pressure inside the droplet surface, γ the surface tension, $\hat{t}$ unit vector tangent to the droplet surface. At the free moving surface, the boundary condition should represent the balance between the viscous and the surface tension stresses. The force exerted on the moving surface is sketched in the Fig. F.2. As shown in the figure, the position along the surface is measured by the arc length *s*, and the forces acted on a small increment *ds* on the surface are considered. The depth in the direction perpendicular to the paper is taken as unit length for convenience of analysis. Then, the total force acting on this area must be zero. The pressure in the droplet provides a force of $-p\hat{n}\,ds$, the negative sign occurring because the force acts opposite to the direction of $\hat{n}$. The contribution of the ambient air to the droplet surface, the interface of the liquid and air, is due to its pressure, $-p_0\hat{n}ds$. By introducing the unit vector $\hat{t}$ that is tangent to the droplet surface, we have the surface tension on the right side of the *ds* to be $-\gamma\hat{t}\big|_s$, the negative sign occurring because the force acts opposite to the direction of $\hat{t}$. On the left side, the surface tension contribution is $\gamma\hat{t}\big|_s + \frac{d(\gamma\hat{t})}{ds}ds$.

Thus, this force balance can be written as:

$$-p\hat{n}\,ds - p_0\hat{n}ds - \gamma\hat{t}\big|_s + \left(\gamma\hat{t}\big|_s + \frac{d(\gamma\hat{t})}{ds}ds\right) = 0 \qquad \text{(F.11)}$$

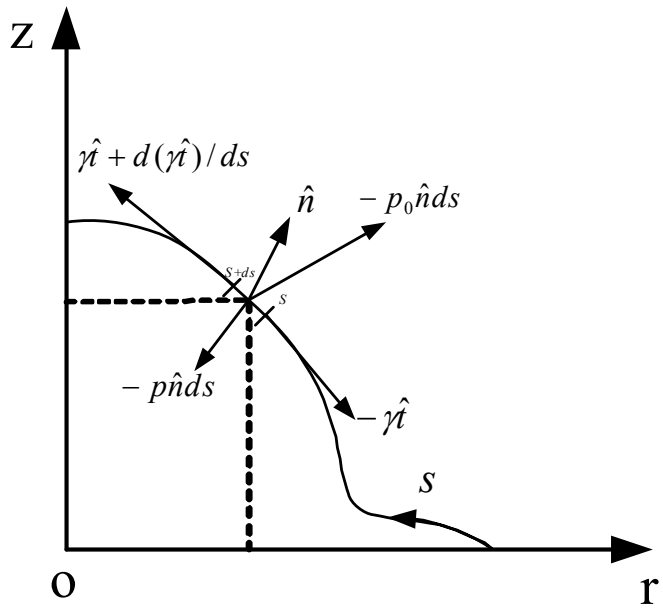

Figure F. 2: The boundary condition of free moving surface.

Considering:

$$\frac{d(\gamma\hat{t})}{ds} = \gamma\frac{d\hat{t}}{ds} + \frac{d\gamma}{ds}\hat{t} = \gamma\kappa\hat{n} + \frac{d\gamma}{ds}\hat{t} \qquad \text{(F.12)}$$

where κ is the curvature of the surface. Then Equation (F.11) reduces to:

$$-p\hat{n} = -(p_0 + \gamma\kappa)\hat{n} + \frac{d(\gamma)}{ds}\hat{t} \qquad \text{(F.13)}$$

The second term includes the derivative of γ with the respect to position along the surface. Because here we consider only fluid dynamic of the droplet and no temperature changes along the surface, we can assume that surface tension γ is a constant and drop out the derivative term in Equation (F.13). Introducing the mean curvature $\kappa_m = \frac{1}{2}(\kappa_1 + \kappa_2)$, where, κ_1 and κ_2 are the largest and smallest normal curvatures respectively, we finally obtain the boundary condition at the droplet surface as:

$$p = p_0 + 2\gamma\kappa_m \qquad \text{(F.14)}$$

Because each point on the free surface can be uniquely defined by a position vector $\tilde{s} = \tilde{s}[r(s), z(s)]$, where s is the coordinate measured along the free surface of the deforming droplet, as shown in Fig. F.2. It has been shown by Lass [Lass H., 1950] that

$$\kappa_m = \frac{r^2(r'z''-z'r'')+[(r')^2+(z')^2]rz'}{2r^2[(r')^2+(z')^2]^{3/2}} \tag{F.15}$$

Because the position of the droplet surface is part of the solution and we do not know where the surface is, we need one more equation. Considering the normal velocity of the surface will be the velocity of the surface itself, we obtain another boundary condition:

$$\tilde{v}_{surface} = (\tilde{v} \cdot \hat{n})\hat{n} \tag{F.16}$$

This boundary condition can be used to find the droplet surface velocity and governs its motion in time.

If the density ρ and viscosity μ of the lubricant is assumed to be constant, and the liquid is regarded as Newtonian fluid, then the constitutive equation that describes the response of the material to applied stresses is:

$$\tilde{\tilde{\tau}} = 2\mu\tilde{\tilde{D}} \tag{F.17}$$

where $\tilde{\tilde{D}}$ is the rate of deformation tensor: $\tilde{\tilde{D}} = \frac{1}{2}\left(\tilde{\tilde{L}} + \tilde{\tilde{L}}^T\right)$, in which $\tilde{\tilde{L}}$ is the velocity gradient tensor and $\tilde{\tilde{L}} = (\nabla\tilde{v})^T$. If Equation (F.17) is applied to Equations (F.2) and (F.3), the balance equations turn out to be Navier-Stokes equations.

F.2.3 Scaling

Before proceeding to the scaling of the equations, we make a summary of what we have obtained. The governing equations for the droplet impact on a solid surface include the continuity balance equation (F.2), and momentum balance equation 3.4(a) and 3.4(b), whereas the initial and boundary conditions are equations (F.5), (F.6), (F.7), (F.8), (F.10) and (F.14), in which equations (F.10) and (F.14) are conditions for the moving free surface of the deforming droplet surface.

In order to learn the characteristic values of all the problem variables, we use the scaling analysis by introducing the following non-dimensional parameters:

$$r^* = \frac{r}{R_0} \tag{F.18}$$

$$z^* = \frac{z}{R_0} \tag{F.19}$$

$$v_z^* = \frac{v_z}{v_0} \tag{F.20}$$

$$v_r^* = \frac{v_r}{v_{rc}} \tag{F.21}$$

$$t^* = \frac{t}{R_0 / v_0} \tag{F.22}$$

$$\kappa_m^* = \frac{k_m}{1/R_0} \tag{F.23}$$

$$p^* = \frac{p - p_0}{P_C} \tag{F.24}$$

$$\tau_{ij}^* = \frac{\tau_{ij}}{\rho v_0^2} \tag{F.25}$$

where v_{rc} and P_C characteristic values for v_r and p respectively. They are unknown at this time and will be determined in the late scaling procedure. The above non-dimensional parameters are created so that their magnitude is of the order of one.

Introducing these non-dimensional parameters into the governing equations and initial and boundary conditions, the scaled equations are then given by:

- Scaled Mass Balance Equation

$$v_{rc} \frac{1}{r^*} \frac{\partial}{\partial r^*}(r^* v_r) + v_0 \frac{\partial v_z}{\partial z} = 0 \tag{F.26}$$

Dividing the equation through by v_{rc}, we have

$$\frac{1}{r^*} \frac{\partial}{\partial r^*}(r^* v_r) + \frac{v_0}{v_{rc}} \frac{\partial v_z}{\partial z} = 0 \tag{F.27}$$

Because there are only two terms in this equation, both derivatives must be $\vartheta(1)$, and we must have $v_{rc} = v_0$. So the scaled mass balance equation is:

$$\frac{1}{r^*} \frac{\partial}{\partial r^*}(r^* v_r) + \frac{\partial v_z}{\partial z} = 0 \tag{F.28}$$

- Scaled Momentum Balance Equations

$$\rho\frac{v_0^2}{R_0}\left(\frac{\partial v_r^*}{\partial t^*}+v_r^*\frac{\partial v_r^*}{\partial r^*}+v_z^*\frac{\partial v_r^*}{\partial z^*}\right)=-\frac{P_C}{R_0}\frac{\partial p^*}{\partial r^*}+\frac{\rho v_0^2}{R_0}\left(\frac{1}{r^*}\frac{\partial}{\partial r^*}\left(r^*\tau_{rr}^*\right)+\frac{\partial\tau_{rz}^*}{\partial z^*}\right) \quad \text{(F.29a)}$$

$$\rho\frac{v_0^2}{R_0}\left(\frac{\partial v_z^*}{\partial t^*}+v_r^*\frac{\partial v_z^*}{\partial r^*}+v_z^*\frac{\partial v_z^*}{\partial z^*}\right)=-\frac{P_C}{R_0}\frac{\partial p^*}{\partial z^*}+\frac{\rho v_0^2}{R_0}\left(\frac{1}{r^*}\frac{\partial}{\partial r^*}\left(r^*\tau_{rz}^*\right)+\frac{\partial\tau_{zz}^*}{\partial z^*}\right)+\rho g \quad \text{(F.29b)}$$

Dividing the equations through by $\rho\frac{v_0^2}{R_0}$, we have

$$\frac{\partial v_r^*}{\partial t^*}+v_r^*\frac{\partial v_r^*}{\partial r^*}+v_z^*\frac{\partial v_r^*}{\partial z^*}=-\frac{P_C}{\rho v_0^2}\frac{\partial p^*}{\partial r^*}+\frac{1}{r^*}\frac{\partial}{\partial r^*}\left(r^*\tau_{rr}^*\right)+\frac{\partial\tau_{rz}^*}{\partial z^*} \quad \text{(F.30a)}$$

$$\frac{\partial v_z^*}{\partial t^*}+v_r^*\frac{\partial v_z^*}{\partial r^*}+v_z^*\frac{\partial v_z^*}{\partial z^*}=-\frac{P_C}{\rho V_0^2}\frac{\partial p^*}{\partial z^*}+\frac{1}{r^*}\frac{\partial}{\partial r^*}\left(r^*\tau_{rz}^*\right)+\frac{\partial\tau_{zz}^*}{\partial z^*}+\frac{gR_0}{v_0^2} \quad \text{(F.30b)}$$

Let $P_C=\rho v_0^2$, the scaled momentum balance equations become:

$$\frac{\partial v_r^*}{\partial t^*}+v_r^*\frac{\partial v_r^*}{\partial r^*}+v_z^*\frac{\partial v_r^*}{\partial z^*}=-\frac{\partial p^*}{\partial r^*}+\frac{1}{r^*}\frac{\partial}{\partial r^*}\left(r^*\tau_{rr}^*\right)+\frac{\partial\tau_{rz}^*}{\partial z^*} \quad \text{(F.31a)}$$

$$\frac{\partial v_z^*}{\partial t^*}+v_r^*\frac{\partial v_z^*}{\partial r^*}+v_z^*\frac{\partial v_z^*}{\partial z^*}=-\frac{\partial p^*}{\partial z^*}+\frac{1}{r^*}\frac{\partial}{\partial r^*}\left(r^*\tau_{rz}^*\right)+\frac{\partial\tau_{zz}^*}{\partial z^*}+\frac{1}{Fr} \quad \text{(F.31b)}$$

where $Fr=\frac{v_0^2}{R_0 g}$ is the Froude number. In a typical lubricant spray in hot forging with average velocity of droplets 5-20 m/s and average radium 20-200 μm, the Fr is in the range of 30 to 100,000. Thus, the gravity effect can be neglected in this case.

- Scaled Initial and Boundary Conditions

I.

When $t^*=0$, $v_r^*=0, v_z^*=-1, and\ p^*=\frac{2}{We}$ (F.32)

II.

When $t^*=0$, $\left(z^*-1\right)^2+r^{*2}=1$, or $r^*=\sqrt{z^*(2-z^*)}$, $0\le z^*\le 2$ (F.33)

III.

At $r^*=0, v_r^*=0, \frac{\partial v_z^*}{\partial r^*}=0$ (F.34)

IV.

At $z^*=0, v_r^*=0$ and $v_z^*=0$, (F.35)

V. At the moving surface

$$p^* = \frac{4\kappa_m^*}{We} \tag{F.36}$$

Where We is the Weber number: $We = \frac{2\rho v_0^2 R_0}{\gamma}$.

$$\tilde{v}^* = (\tilde{v}^* \cdot \hat{n})\hat{n} \tag{F.37}$$

F.3 Numerical Solution – FLOW-3D Simulation

FLOW-3D is chosen to be the simulation tool for this study. FLOW-3D is a general purpose, three-dimensional, computational fluid dynamic (CFD) program that has the ability to predict flows with free surfaces. It has many capabilities. Using different input data, researchers can select various physical options to represent a wide range of fluid flow phenomena.

FLOW-3D uses the volume of fluid (VOF) method to predict free-surface fluid motions. It numerically solves the fluid flow governing equations using finite-difference approximations. The computational domain is divided into uniform/variable sized rectangular cells and the geometric features are embedded in the mesh blocks. For each cell, values are computed for the basic flow quantities (e.g., velocity, pressure, temperature).

Before the discussion of the application of FLOW-3D for numerically solving the fluid dynamic model of the lubricant droplet impact, it is important to understand how FLOW-3D works to simulate the basic fluid flow, especially the Volume of Fluid (VOF) method.

In FLOW-3D free surfaces are modeled with the Volume of Fluid (VOF), a technique first reported in Nichols and Hirt (1975), and more completely in Hirt and Nichols (1981). The VOF method consists of three ingredients: a scheme to locate the surface, an algorithm to track the surface as a sharp interface moving through a computational grid, and a means of applying boundary conditions at the surface.

F.3.1 Fraction Function, Fractional Volume and Fractional Area

The fluid fraction function F is defined to be equal to 1.0 in the fluid and 0.0 outside fluid, i.e. in the void. Averaged over a control volume (or a cell), the value of F will be within the segment [0.0, 1.0], as shown in Fig. 3.3. The volume of fluid in a cell is defined:

$$FV = V_f dxdydz \tag{F.38}$$

The kinematic equation for the VOF function F in the absence of mass sources is:

$$\frac{\partial F}{\partial t} + \left[\frac{\partial}{\partial x}(Fv_x) + \frac{\partial}{\partial y}(Fv_y) + \frac{\partial}{\partial z}(Fv_z) \right] = 0 \tag{F.39}$$

FLOW-3D utilizes the fractional area/volume method (FAVOR) to model complex geometric boundaries instead of using deformed grids employed by finite-element methods. The FAVOR concept can be used in connection with any type of grid including grids consisting of rectangular or distorted elements and whether or not the grid is structured or unstructured. Structured grids are best because they are easy to generate and the indices for neighboring elements are known. Rectangular grid elements make it easy to compute the fractional areas and volumes of elements used by the FAVOR method.

As shown in the Fig. 3.4, the fractional area and volume ratios A_f and V_f are defined as:

$$A_f = \frac{\text{open area}}{\text{cell edge area}} \quad \text{and} \quad V_f = \frac{\text{open volume}}{\text{volume of the cell}} \tag{F.40}$$

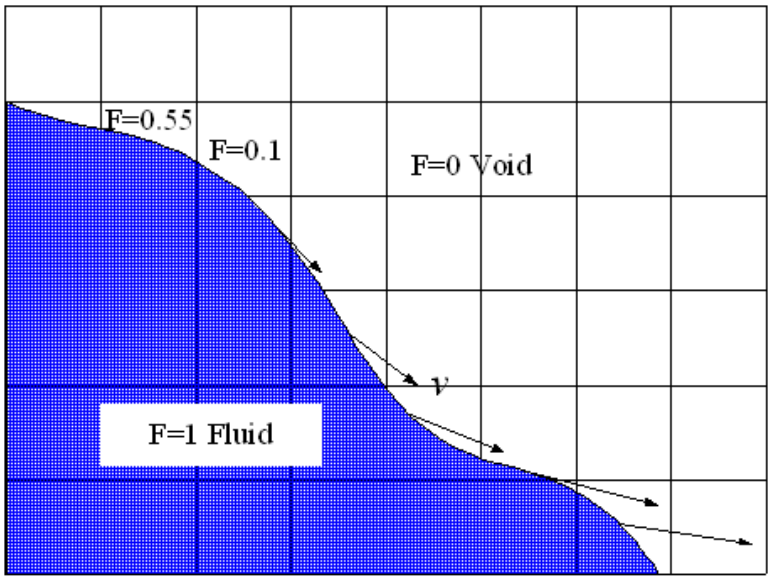

Figure F. 3: Typical values of the VOF function *F* in the droplet model.

If there are geometrical constraints of the flow, then the kinematic equation of F is:

$$V_f \frac{\partial F}{\partial t} + \nabla \cdot (\vec{A}\vec{v}F) = 0 \tag{F.41}$$

or

$$\frac{\partial F}{\partial t} + \left[\frac{\partial}{\partial x}\left(FA_x v_x\right) + \frac{\partial}{\partial y}\left(FA_y v_y\right) + \frac{\partial}{\partial z}\left(FA_z v_z\right) \right] = 0 \tag{F.42}$$

where V_f and $\vec{A} = (A_x, A_y, A_z)$ are the volume and area fractions describing the geometrical constraints of the flow, $\vec{v} = (v_x, v_y, v_z)$ is the flow velocity. The numerical solution of Equation (F.41) or (F.42) must prevent unphysical distortion of the interface and preserve its sharpness. The latter requirement means that the interface between fluid and void must be no more than one cell wide. Integrating the A_f and V_f into conversion equations, we have the equation transformation as:

$$\frac{\partial C}{\partial t} + v_x \frac{\partial C}{\partial x} + v_y \frac{\partial C}{\partial y} + v_z \frac{\partial C}{\partial z} \Rightarrow \frac{1}{VF}\frac{\partial C}{\partial t} + v_x AF_x \frac{\partial C}{\partial x} + v_y AF_y \frac{\partial C}{\partial y} + v_z AF_z \frac{\partial C}{\partial z} \quad \text{(F.43)}$$

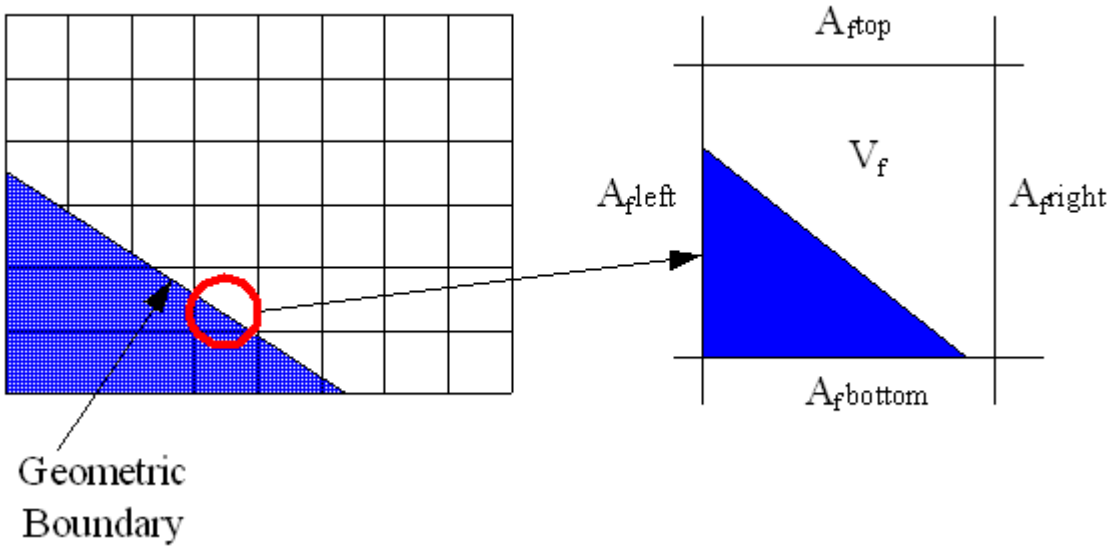

Figure F. 4: Fractional area/volume method (FAVOR).

F.3.2 The Governing Equations in Flow-3D Format

Introducing F, V_f and $\vec{A} = (A_r, A_\theta, A_z)$ into equations (F.1), (F.2) and (F.3), the governing equations become:

$$\frac{\partial}{\partial r}(v_r A_r) + \frac{\partial (v_z A_z)}{\partial z} + \frac{v_r A_r}{r} = 0 \quad \text{(F.44)}$$

$$\frac{\partial v_r}{\partial t}+\frac{1}{V_f}\left(v_r A_r \frac{\partial v_r}{\partial r}+v_z A_z \frac{\partial v_r}{\partial z}\right) = -\frac{1}{\rho}\frac{\partial p}{\partial r}+\frac{1}{\rho V_f}\left(\frac{\partial}{\partial r}\left(A_r \tau_{rr}\right)+\frac{\partial\left(A_z \tau_{rz}\right)}{\partial z}+\frac{\left(A_r \tau_{rr}\right)}{r}\right) \tag{F.45}$$

and

$$\frac{\partial v_z}{\partial t}+\frac{1}{V_f}\left(v_r A_r \frac{\partial v_z}{\partial r}+v_z A_z \frac{\partial v_z}{\partial z}\right) = -\frac{1}{\rho}\frac{\partial p}{\partial z}+\frac{1}{\rho V_f}\left(\frac{\partial}{\partial r}\left(A_r \tau_{rz}\right)+\frac{\partial\left(A_z \tau_{zz}\right)}{\partial z}+\frac{\left(A_r \tau_{rz}\right)}{r}\right)-g \tag{F.46}$$

F.3.3 Numerical Approximations

The governing equations are numerically solved by Flow-3D using Finite Differences method. To produce a simple and efficient computation, explicit scheme is applied to evaluate the current time level values of the velocities except those of pressure forces because pressures can only be calculated by implicitly coupling momentum equations and mass equation. Explicit scheme means one unknown value of a variable can be found directly from known values of the variables. However, implicit scheme means the discretization produces an equation where several unknown values are related to several known values, and thus to produce a solution with an implicit scheme a set of simultaneous equations must be solved to find the unknown values.

Discretizing equations (F.45) and (F.46), the form of explicit scheme for the finite differences approximation of velocities is:

$$v_r\Big|_{i,j}^{n+1} = v_r\Big|_{i,j}^{n}+\delta t^{n+1}\left[\frac{p_{i+1,j}^{n+1}-p_{i,j}^{n+1}}{\rho\left(\delta r_i+\delta r_{i+1}\right)/2}-FRR-FRZ+VISR\right] \tag{F.47}$$

and

$$v_z\Big|_{i,j}^{n+1} = v_z\Big|_{i,j}^{n}+\delta t^{n+1}\left[-\frac{p_{i,j+1}^{n+1}-p_{i,j}^{n+1}}{\rho\left(\delta r_z+\delta r_{z+1}\right)/2}-FZR-FZZ+VISZ-g\right] \tag{F.48}$$

where: FRR, FRZ mean the advective flux of v_r in the r and z directions respectively; Similarly, FZR, FZZ mean the advective flux of v_z in the r and z directions respectively. VISR and VISZ are the r and z components viscous acceleration respectively. And they are:

FRR

$$= \frac{0.5\left(\delta r_i + \delta r_{i+1}\right)}{\delta r_i V_f\Big|_{i,j} + \delta r_{i+1} V_f\Big|_{i+1,j}} \left[\left(v_r\Big|^n_{i+1,j} A_r\Big|_{i+1,j} + v_r\Big|^n_{i,j} A_r\Big|_{i,j} \right) \frac{v_r\Big|^n_{i+1,j} - v_r\Big|^n_{i,j}}{\delta r_{i+1}} + \left(v_r\Big|^n_{i,j} A_r\Big|_{i,j} + v_r\Big|^n_{i-1,j} A_r\Big|_{i-1,j} \right) \frac{v_r\Big|^n_{i,j} - v_r\Big|^n_{i-1,j}}{\delta r_i} \right] \tag{F.49}$$

FRZ

$$= \frac{0.5\left(\delta z_i + \delta z_{i+1}\right)}{\delta z_i V_f\Big|_{i,j} + \delta z_{i+1} V_f\Big|_{i+1,j}} \left[\left(v_r\Big|^n_{i+1,j} A_z\Big|_{i+1,j} + v_r\Big|^n_{i,j} A_z\Big|_{i,j} \right) \frac{v_r\Big|^n_{i+1,j} - v_r\Big|^n_{i,j}}{\delta z_{i+1}} + \left(v_r\Big|^n_{i,j} A_z\Big|_{i,j} + v_r\Big|^n_{i-1,j} A_z\Big|_{i-1,j} \right) \frac{v_r\Big|^n_{i,j} - v_r\Big|^n_{i-1,j}}{\delta z_i} \right] \tag{F.50}$$

VISR

$$= \frac{\delta r_i + \delta r_{i+1}}{2\rho\left(\delta r_i V_f\Big|_{i,j} + \delta r_{i+1} V_f\Big|_{i+1,j}\right)} \left[\frac{\left(\tau_{rr}\Big|^n_{i,j} A_r\Big|_{i,j} - \tau_{rr}\Big|^n_{i-1,j} A_r\Big|_{i-1,j} \right)}{\delta r_i} + \frac{\left(\tau_{rz}\Big|^n_{i,j} A_z\Big|_{i,j} - \tau_{rz}\Big|^n_{i-1,j} A_z\Big|_{i-1,j} \right)}{\delta z_i} + \frac{\tau_{rr}\Big|^n_{i,j} A_r\Big|_{i,j} + \tau_{rr}\Big|^n_{i-1,j} A_r\Big|_{i-1,j}}{2 r_i} \right] \tag{F.51}$$

FZR

$$= \frac{0.5\left(\delta r_i + \delta r_{i+1}\right)}{\delta r_i V_f\big|_{i,j} + \delta r_{i+1} V_f\big|_{i+1,j}} \left[\left(v_z\big|^n_{i+1,j} A_r\big|_{i+1,j} + v_z\big|^n_{i,j} A_r\big|_{i,j} \right) \frac{v_z\big|^n_{i+1,j} - v_z\big|^n_{i,j}}{\delta r_{i+1}} + \left(v_z\big|^n_{i,j} A_r\big|_{i,j} + v_z\big|^n_{i-1,j} A_r\big|_{i-1,j} \right) \frac{v_z\big|^n_{i,j} - v_z\big|^n_{i-1,j}}{\delta r_i} \right] \quad \text{(F.52)}$$

FZZ

$$= \frac{0.5\left(\delta z_i + \delta z_{i+1}\right)}{\delta z_i V_f\big|_{i,j} + \delta z_{i+1} V_f\big|_{i+1,j}} \left[\left(v_z\big|^n_{i+1,j} A_z\big|_{i+1,j} + v_z\big|^n_{i,j} A_z\big|_{i,j} \right) \frac{v_z\big|^n_{i+1,j} - v_z\big|^n_{i,j}}{\delta z_{i+1}} + \left(v_z\big|^n_{i,j} A_z\big|_{i,j} + v_z\big|^n_{i-1,j} A_z\big|_{i-1,j} \right) \frac{v_z\big|^n_{i,j} - v_z\big|^n_{i-1,j}}{\delta z_i} \right] \quad \text{(F.53)}$$

And

VISZ

$$= \frac{\delta r_i + \delta r_{i+1}}{2\rho\left(\delta r_i V_f\big|_{i,j} + \delta r_{i+1} V_f\big|_{i+1,j}\right)} \left[\frac{\left(\tau_{rz}\big|^n_{i,j} A_r\big|_{i,j} - \tau_{rz}\big|^n_{i-1,j} A_r\big|_{i-1,j} \right)}{\delta r_i} + \frac{\left(\tau_{zz}\big|^n_{i,j} A_z\big|_{i,j} - \tau_{zz}\big|^n_{i-1,j} A_z\big|_{i-1,j} \right)}{\delta z_i} + \frac{\tau_{rz}\big|^n_{i,j} A_r\big|_{i,j} + \tau_{rz}\big|^n_{i-1,j} A_r\big|_{i-1,j}}{2 r_i} \right] \quad \text{(F.54)}$$

Equations (F.47) and (F.48) evaluate velocities by the advective and viscous terms of the previous time level (n) values. However, the pressures at time level n+1 (p^{n+1}) are unknown at the beginning of the cycle, and p^{n+1} in Equations (F.47) and (F.48) must be placed by p^n to get a first guess for the new velocity.

The pressures must be solved by coupling the Equations (F.47) and (F.48) and the following discretized mass balance equation:

$$\frac{v_r\Big|_{i,j}^{n+1} A_r\Big|_{i+1,j} + v_r\Big|_{i,j} A_r\Big|_{i,j}}{\delta r_{i+1}} + \frac{v_z\Big|_{i,j}^{n+1} A_z\Big|_{i+1,j} + v_z\Big|_{i,j} A_z\Big|_{i,j}}{\delta z_{i+1}} + \frac{v_r\Big|_{i,j}^{n+1} A_r\Big|_{i,j} + v_{r-1}\Big|_{i,j} A_r\Big|_{i-1,j}}{2r_i} = 0 \qquad \text{(F.55)}$$

Then the updated pressures can be used in Equations (F.47) and (F.48) to get the values of velocities for the next time level.

The initial condition Equation (F.6) is used to evaluate the beginning values of $F\Big|_{i,j}^{0}$, $A_r\Big|_{i,j}^{0}, A_z\Big|_{i,j}^{0}$, and $V_f\Big|_{i,j}^{0}$, while Equation (F.5) is used to determine beginning values of $v_r\Big|_{i,j}^{0}, v_z\Big|_{i,j}^{0}$, and $p_{i,j}^{0}$.

Then the boundary conditions are applied to get the values at the boundary points:

- Equation (F.7) sets $v_r\Big|_{i,j}^{n} = 0$ and $v_z\Big|_{i,j}^{n} = v_z\Big|_{i+1,j}^{n}$ for all cells at *r = 0*.
- Equation (F.8) sets $v_r\Big|_{i,j}^{n} = 0$ and $v_z\Big|_{i,j}^{n} = 0$ for all cells at *z = 0*.
- Equation (F.10) sets $v_r\Big|_{i,j}^{n} = v_r\Big|_{i+1,j}^{n}$, $v_r\Big|_{i,j}^{n} = v_r\Big|_{i,j+1}^{n}$, $v_z\Big|_{i,j}^{n} = v_z\Big|_{i+1,j}^{n}$ and $v_z\Big|_{i,j}^{n} = v_z\Big|_{i,j+1}^{n}$ for all cells in which $0 < F < 1$ at free moving surface.
- Equation (F.14) sets $p_{i,j}^{n} = p_0 + 2\gamma\kappa_m\Big|_{i,j}^{n}$ for all cells in which $0 < F < 1$ at free moving surface. $2\gamma\kappa_m\Big|_{i,j}^{n}$ is approximated as the surface tension pressure, detailed in FLOW-3D Manual, Version 8.1, 2201.

Additionally, for the Newtonian liquid with constant viscosity, constitutive Equation (F.17) sets:

$$\tau_{rr}\Big|_{i,j}^{n} = 2\mu \frac{\left(v_r\Big|_{i+1,j}^{n} - v_r\Big|_{i,j}^{n}\right)}{\delta r_{i+1}} \qquad \text{(F.56)}$$

$$\tau_{zz}\Big|_{i,j}^{n} = 2\mu \frac{\left(v_z\Big|_{i+1,j}^{n} - v_z\Big|_{i,j}^{n}\right)}{\delta z_{i+1}} \qquad \text{(F.57)}$$

and

$$\tau_{rz}\Big|_{i,j}^{n} = \tau_{zr}\Big|_{i,j}^{n} = \mu \frac{\left(v_r\Big|_{i+1,j}^{n} - v_r\Big|_{i,j}^{n}\right)}{\delta z_{i+1}} + \mu \frac{\left(v_z\Big|_{i,j+1}^{n} - v_z\Big|_{i,j}^{n}\right)}{\delta r_{i+1}} \qquad \text{(F.58)}$$

Equations (F.56) to (F.58) are introduced to stress terms in Equation (F.51) and (F.54) to evaluate the viscous accelerations VISR and VISZ.

F.4 Experimental Setup

Before experiment, graphite-based lubricant with 54% solid content (weight %) was diluted by distilled water to 5:3, 1:1, 1:5, and 1:20, which are volume ratios of lubricant to water. Droplets of these diluted lubricants were used in the experiment. As illustrated in Fig. F.5, the experiment was set up with a droplet generator mounted on a fixture to create droplets. A camcorder and a high speed camera took pictures of the droplet formation and its kinetics during impact on the heated surface. The images were later sent to computer for imaging processing to measure deposition dimensions. Lubricant droplets were generated in diameters of 2mm, 3mm, and 4 mm and made to fall under their own gravity. Impact velocities were obtained between 10cm/s and 200 cm/s by changing the height "H" of the droplet generator. The flat H-13 steel surface was finished to roughness Ra 50 micro-inch (or 1.25μm).

F.5 Measurement of the Lubricant Properties

The lubricant contains many surfactants and binders that change the droplet surface energy, rheology, physics and thermodynamics. The composition of the lubricant is often a trade secret. Hence, we have to determine the properties of the lubricant before we go further to build our fluid dynamic model.

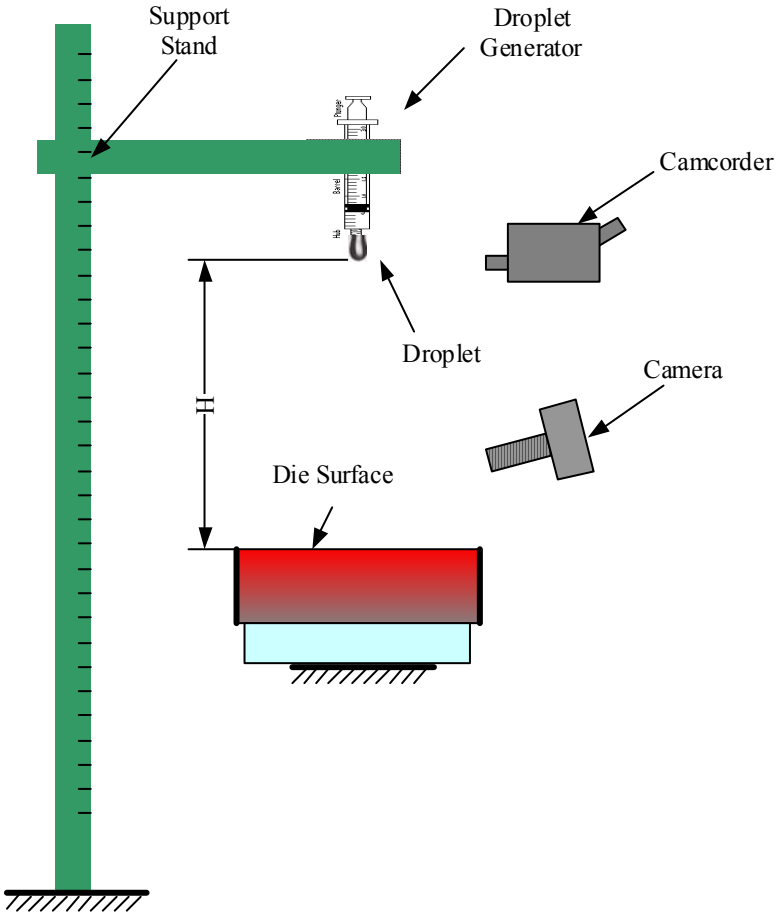

Figure F. 5: Schematic experiment setup.

F.5.1 Surface Tension

Two methods, pendant drop method and capillary action method, are used to measure the surface tension of the lubricants.

- **Pendant drop method**

In the experiments, lubricant is slowly discharged from a droplet generator. It is shown in Fig. F.6.

Mechanical equilibrium between surface tension force and gravity can be expressed in the form:

$$mg = \pi d_{\min}\gamma \text{, or } \rho\left(\frac{1}{6}\pi d^3\right)g = \pi d_{\min}\gamma \qquad \text{(F.59)}$$

where $d_{\min}$ is approximately the diameter of the dropper exit, ρ the density of lubricant, γ the surface tension. From this relation, the surface tension γ is:

$$\gamma = \frac{\rho_l g d^3}{6 d_{\min}} \qquad \text{(F.60)}$$

where ρ_l is the density of lubricant and is obtained through dividing the lubricant weight measured on a balance by the volume measured using a graduated glass cylinder. As long as we know d_{min} and d, σ is derivable. d_{min} and d are obtained through imaging processing by transporting the images taken by the speed camera.

- **Capillary action method**

Capillary action is the result of adhesion and surface tension. Adhesion of liquid to the walls of a vessel will cause an upward force on the liquid at the edges and result in a meniscus which turns upward. The surface tension acts to hold the surface intact, so instead of just the edges moving upward, the whole liquid surface is dragged upward. The method is schematically shown in Fig.F.7. The height "h" to which capillary action will lift liquid depends upon the weight of liquid which the surface tension will lift:

$$\gamma \cdot 2\pi R = \rho g(h\pi R^2) \qquad \text{(F.61)}$$

So, if the height of lifted liquid h is measured, surface tension can be given as:

$$\gamma = \frac{\rho_l g R h}{2} \qquad \text{(F.62)}$$

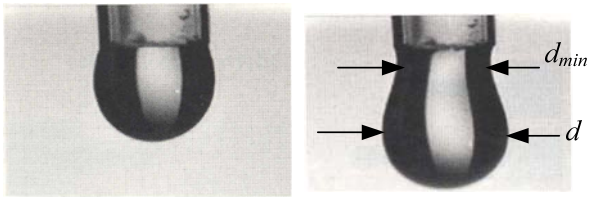

Figure F. 6: Generation of single droplets by a droplet generator.

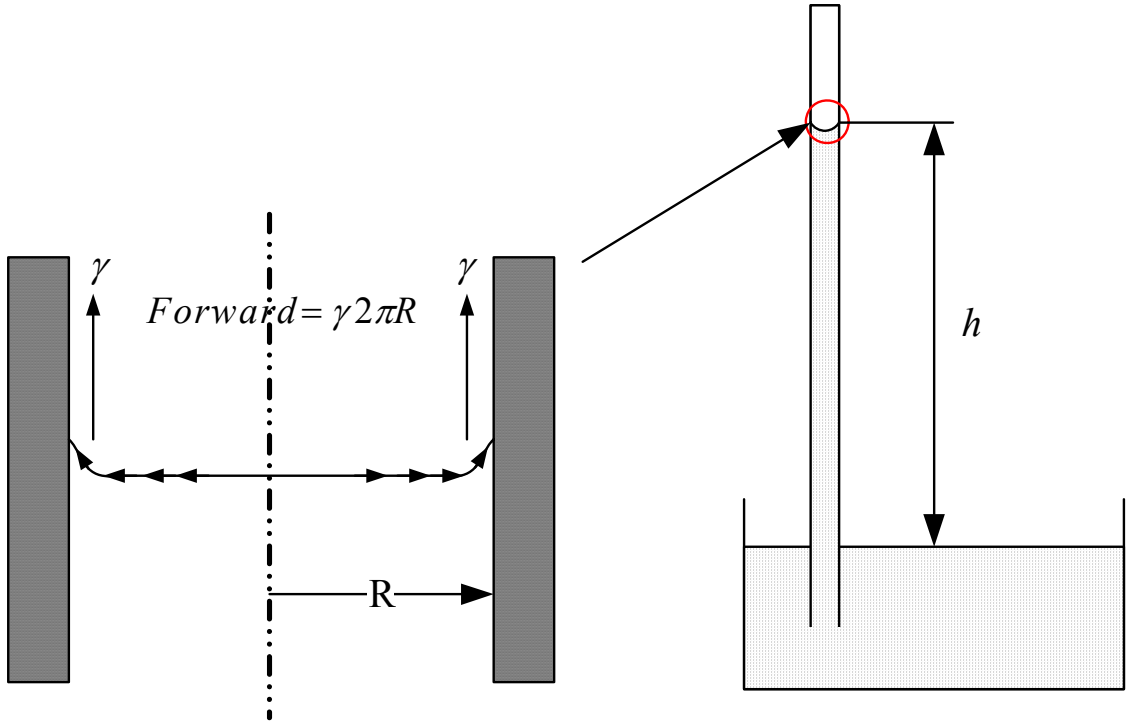

Figure F. 7: Capillary action method.

F.5.2 Viscosity

With lubricant for which the shear stress and shear rates are proportional (Newtonian flow behavior), the kinematic viscosity can be determined by measuring the time for a volume of lubricant to flow under gravity through a calibrated glass capillary viscometer. This method is recommended by the ASTM445-01. Shown in Fig.F.8, the kinematic viscosity ν is obtained by multiplying the time of emptying a fixed volume of liquid by a container constant C, which is calibrated by a liquid with known viscosity. Then we have the dynamic viscosity by multiplying the kinematic viscosity, ν, by the density of the lubricant.

F.5.3 Results of the Lubricant Properties

Table F.1 shows the measured properties of lubricants. DP stands for pendant drop method in

and CA capillary action method. Liquids tested include pure water. One can observe the facts: a). higher dilution ratio companies with higher surface tension; b). for liquids with dilution ratio larger than 1:1, the surface tension approaches to that of the water. As we can see that all surface tensions estimated by drop pendant method are less than those by capillary action method for about 10 dynes/cm though they share the same trend. Considering the fact that surface tension for water is 72.8 dynes/cm, we regard that results gained from capillary action method are closer to the true values.

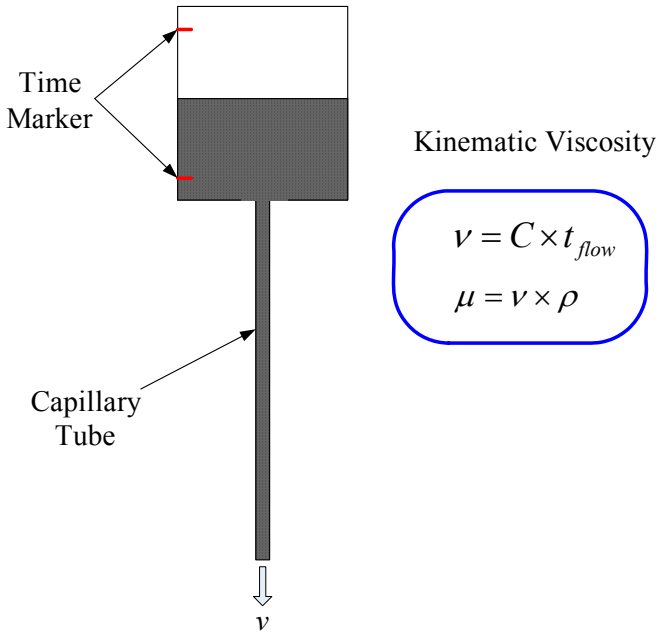

Figure F. 8: Viscosity measurement based on ASTM 445-01.

Liquids	Density ρ_l (g/cm^2)	γ by PD (dynes/cm)	γ by CA (dynes/cm)	Kinematic (cSt)	Dynamic (Poise)
5:3	1.08	40.67	52.71	56.43	0.523
1:1	1.065	45.15	69.89	7.22	0.077
1:5	1.021	55.57	71.00	1.58	0.016
1:20	1.005	59.03	73.38	1.25	0.013
Water	0.999	62.21	75.22	1.03	0.011

Table F. 1: Measured properties of lubricants

Since dynamic viscosity of water is 0.0114 poise, when dilution ratio is large than 1:5, the viscosity of lubricant is approaching to that of the water.

F.6 CFD Simulation

The simulations were controlled to maintain the phenomena in the spreading wetting regions (<250^{o}C) [Yang, L., 2005]. To numerically compute fluid flow and heat transfer during a lubricant

droplet impact is extremely difficult since it involves interaction between such phenomena as free surfaces undergoing large deformations, rapid vaporization of the liquid, and deposition of inside solid particles. We start the CFD model without heat transfer, i.e., only fluid dynamic is considered. This model takes no more than 0.5 second, a time which is very short compared to that of evaporation. Influence of solid particle on flow motion was neglected since the forces that particle exert on the fluid are small compared to the fluid inertia during impact, especially for high diluted lubricant droplets in which particle mass is small.

The simulations were conducted by varying droplet size (2mm, 3mm and 4mm), velocity (10cm/s, 50cm/s, 100cm/s and 200cm/s) and lubricant properties (surface tension and viscosity). Effects of contact angle were neglected in this dynamic simulation, justified by the work of Pasandideh-Fard [Fukai, J., 1993]. The configuration and meshing of the simulation is shown as Fig. F.9. to F.11 give examples of the simulation results of lubricant 1:1 with 4mm diameter droplet at impact velocity 10cm/s and 100cm/s respectively.

It can be observed that the flow recoils back to the center when the droplet reaches the maximum spreading. This can be explained by the balance of surface tension and inertial forces. The inertia of the droplet overcomes the viscous force and surface tension and spreads outwards from the center when the droplet hits the surface. The increasing surface consumes all inertia when the droplet reaches the maximum spreading. After that, the surface tension draws back the droplet and the flow is recoiled. This process cycles several times before the flow is stabilized. Since the maximum contact area of the droplet with the surface is very important for the heat transfer rate (the larger this area is, the faster the heat can be transferred), we introduced the dimensionless factor, $\xi_{max} = D_{max}/Do$, to describe the spreading characteristics.

F.7 Results and Discussions

Since the maximum contact area of the droplet with the surface is very important for the heat transfer rate (the larger this area is, the faster heat transfer can be expected) and film formation, we introduced the dimensionless factor, $\xi_{max} = d_{max}/d_o$, to describe the spreading characteristics.

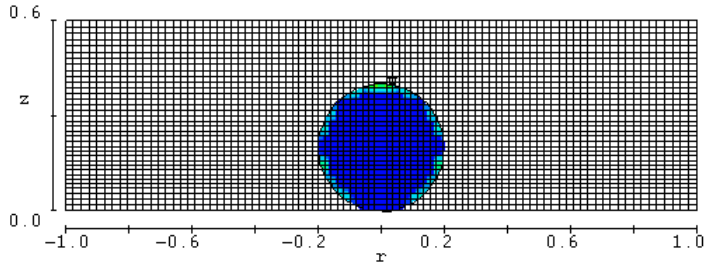

Figure F. 9: The configuration and meshing of the simulation.

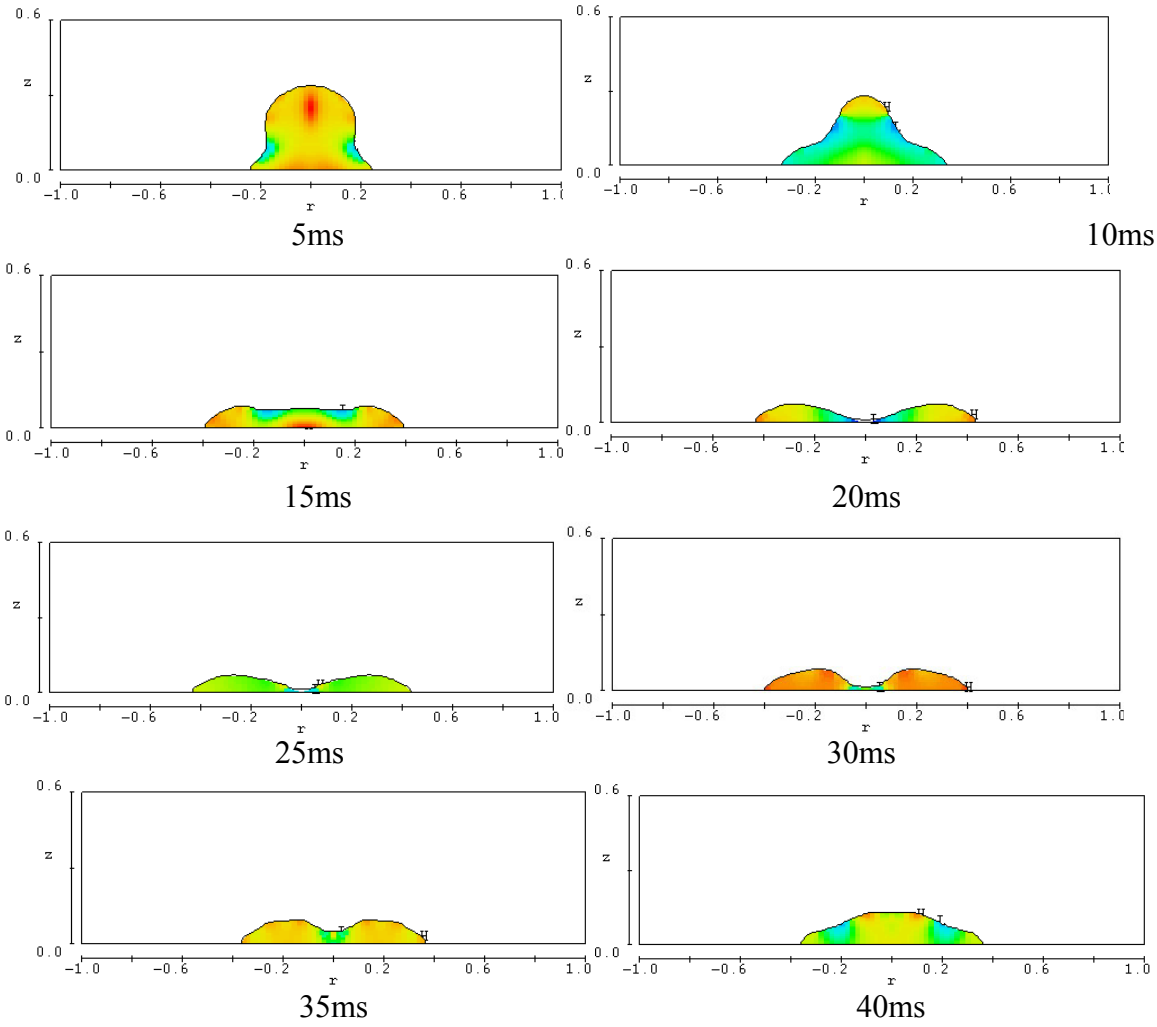

Figure F. 10: simulation results of lubricant 1:1 with 4mm diameter droplet at impact velocity 10cm/s.

Fig. F.12 shows the experimental results of ξ_{max} as a function of die surface temperature. This figure presents that spreading coefficient ξ_{max} are almost independent of temperature at die temperatures below Leidenfrost points (<300^{o}C for all dilution ratios). The results of water based graphite lubricants correspond with what observed in studies [Makino, K., 1984, Engel, O.G., 1955; Savic, P., 1955, 1958; Inada, S., 1983; Toda, S.1974; Akao, F., 1980; Chandra, S., 1991] and allow the fluid dynamic model to present the droplet spreading in the region of nucleate and convection boiling. Fig. F.13 shows the comparison of experiment and simulation results of ξ_{max} versus Reyonlds number *Re* for lubricants with different dilution ratios, while Fig. 3.14 shows the results of ξ_{max} versus Weber number *We*. Shown both in Figs.F.13 and F.14, results of experiment and simulation agree well except at high values of We, the numbers close to critical We number We_{crit} beyond which droplet will undergo breakup. For all lubricants at high Weber numbers, results of simulation are higher than those from experiments. This may be caused by the neglecting effects of graphite suspended in the liquid in our simulation model.

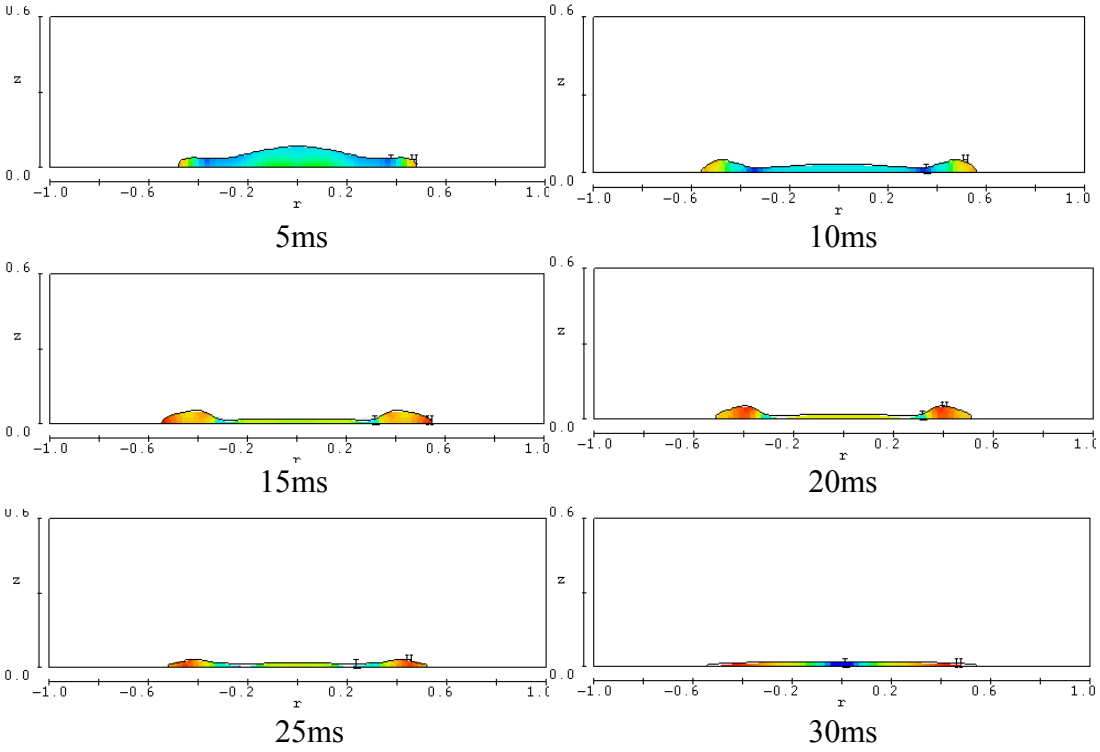

Figure F. 11: Simulation results of lubricant 1:1 with 4mm diameter droplet at impact velocity 100cm/s.

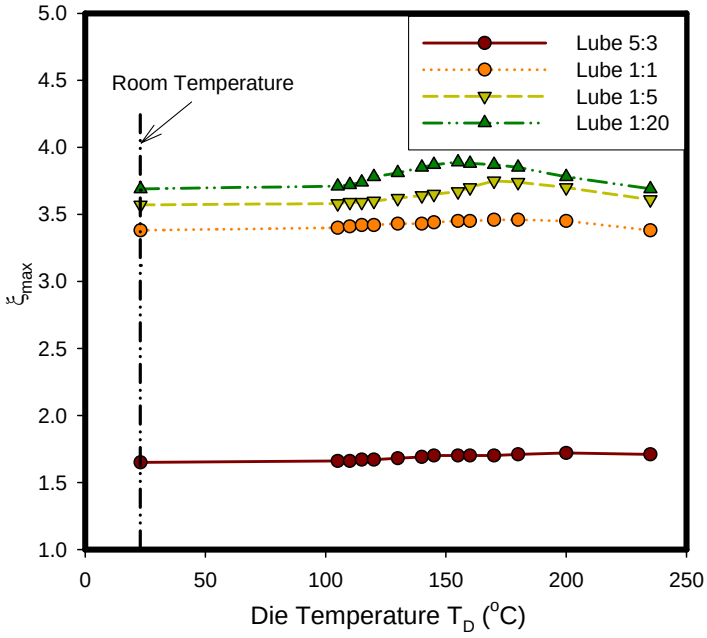

Figure F. 12: Experimental results of ξ_{max} v.s. TD. We = 27.

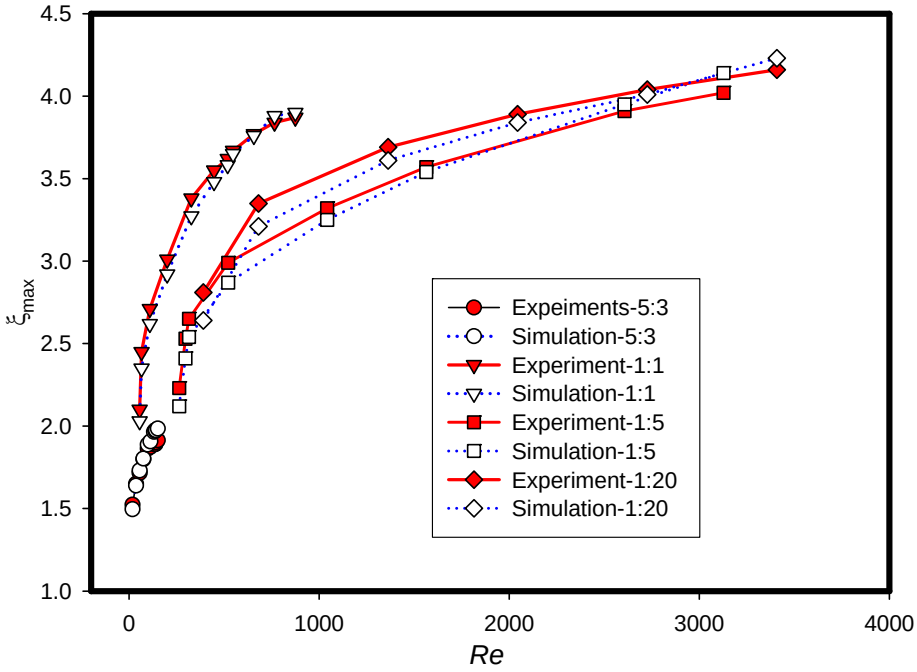

Figure F. 13: Experiment and simulation results of lubricants, ξ_{max} v.s. Re.

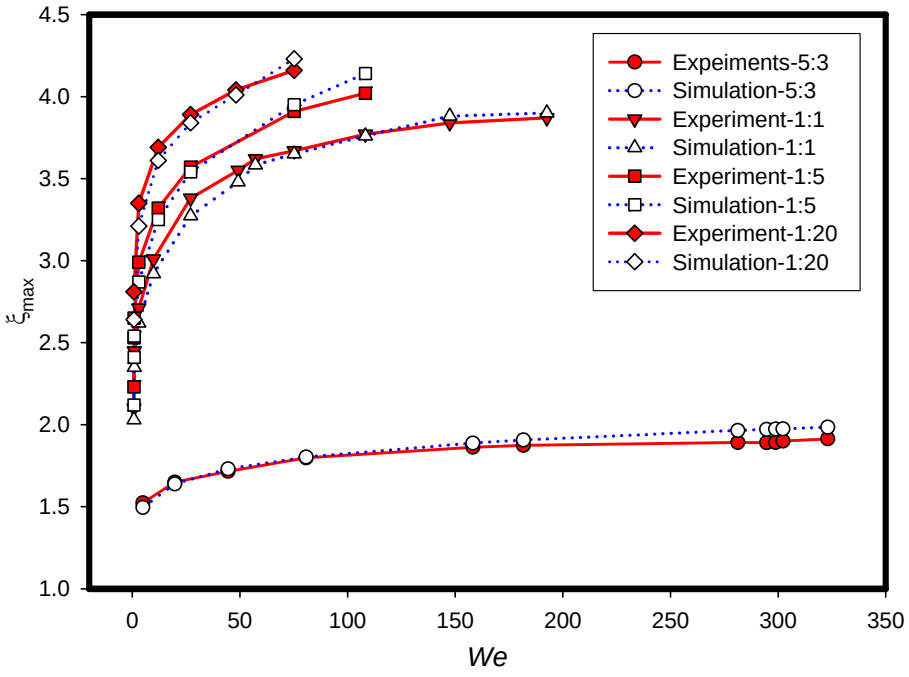

Figure F. 14: Experiment and simulation results of lubricants, ξ_{max} v.s. We.

It is observed in the simulations that spreading velocity in radial direction is 5 to 10 times higher than impact velocity at the high end of We. The velocity change is high enough to make the liquid with suspensions to be shear-thickening liquid [Boersma, W.H., 1995; Bender, J. W., 1995],

i.e., its viscosity increases as the sheer rate increases.

The formation of shear thickening may be explained by clustering of graphite particles at high shear rate, and these flow-induced clusters results in an increased dissipation of energy and, consequently, the viscosity increases. Boersma et al. [Boersma, W.H., 1995] stated that for a suspension to exhibit shear-thickening, two conditions must hold: firstly, the volume fraction of solids in the suspension must be high; secondly, the suspension must be nonflocculated. The lubricants studied in this paper meet both of the two criteria, and shear thickening caused by graphite is reasonable to explain the result difference of simulation and experiment shown in Fig. F.13 and Fig. F.14. From Fig. F.15 and Fig. F.16 one can observe that there is a good linear log-log relationship between ξ_{max} and Re, *We* for lubricants. However, two segments are identified: one at low range of Re or We, another at high Re or We for the highly diluted lubricants. This may be caused by the effect of viscosity force coupling with the spreading velocity. At low velocity (low level of *Re* and *We* for each lubricant) viscous dissipation can be ignored for high diluted lubricants, but it can be dominant for droplet of lubricant 5:3 spreading on the die surface even at low velocity level. When impact velocity is increased, viscous dissipation becomes dominant even for highly diluted lubricants considering the shear thickening discussed above.

Dilution Ratios	Simulation		Experiment	
β	A	B	A	B
5:3	0.1269	0.0679	0.1479	0.0534
1:1	0.3544	0.1093	0.3727	0.1012
1:5	0.3846	0.1154	0.4056	0.1015

Table F. 2: Material constants for different dilution rations for equation
$\log(\xi_{\max}) = \mathrm{A} + \mathrm{B}\ \log(\mathrm{We})$

We observed that the higher lubricant is diluted, the larger spreading $\xi_{\max}$ is obtained for a fixed Re or We number. This is because low diluted lubricant has high viscosity and low surface tension. Viscosity of lubricant with dilution ratio of 5:3 is almost 50 times more than that of lubricant with dilution ratio of 1:20, while surface tension of the former is more than half of the latter. This means that viscous dissipation is a dominant factor for lubricant with high dilution ratio comparing with the effect of surface tension, especially at the beginning of the impact when the change of surface area is small. Another reason may also rely on the easier shear thickening for high volume fraction of graphite suspensions in the low diluted lubricant. Ignoring the turning of log- log curves at low Weber number *We* in Fig. F.16, we fit these curves by the least square method and obtain the relations shown in Table F.2. We see that for lubricants with diluted ratio higher than 1:1, the log-log relations between spreading coefficient $\xi_{\max}$ v.s. Weber number *We* are pretty much close. We fit the simulation results for all these lubricants together and have:

$$\log(\xi_{\max}) = \mathrm{A} + \mathrm{B}\ \log(\mathrm{We}) \qquad \text{(F.63)}$$

Where A = 0.3906 and B = 0.1038 for β less than equal to one. Equation (F.63) in its simple

expression can be used in the evaluation of droplet impact of lubricant with high dilution ratios in metal processing.

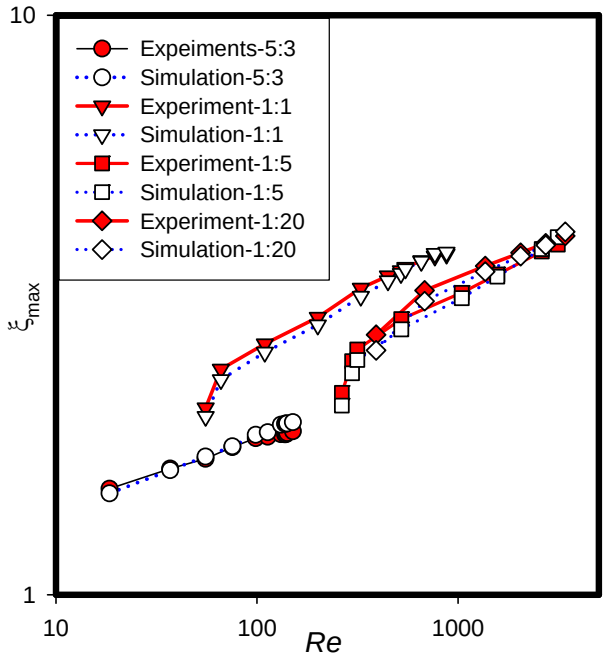

Figure F. 15: Experiment and simulation results of lubricants, log(ξ_{max}) v.s. log(Re).

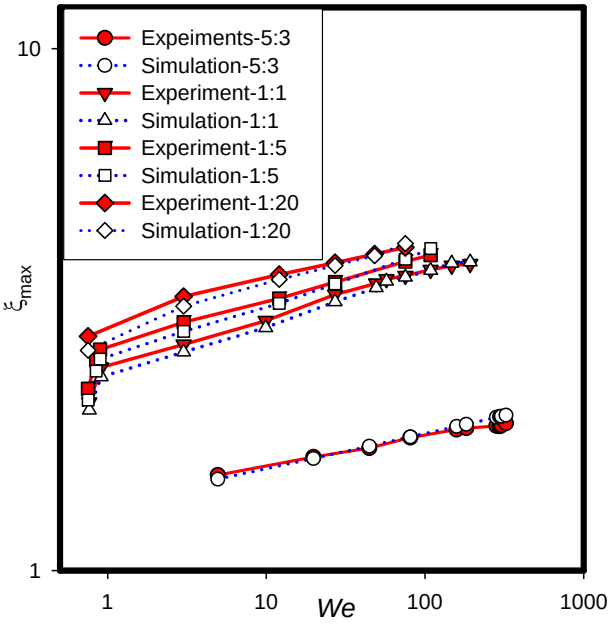

Figure F. 16: Experiment and simulation results of lubricants, log(ξ_{max}) v.s. log(We).

F.8 Summary of the Investigation

In this chapter, an isothermal model based on momentum equations is proposed for investigating lubricant spread on hot die surfaces. The governing equations are discretized using the VOF finite difference scheme. The lubricant properties needed for this model are determined by simple capillary experiments. This model is applied to the study of droplet dynamics and spread for different lubricant properties and different impact conditions. The model predictions are compared with those of single droplet experiments at different Weber numbers and lubricant dilution ratios. It is seen that the numerical model adequately simulates the droplet behavior including its spread over the entire range of experimental conditions. Finally, a relation is derived between the spread factor and the Weber number that is valid for all dilution ratios greater than unity (dilute suspensions). This relation together with the numerical model can be used to determine the best droplet spray parameters for the desired lubricant film thickness.

APPENDIX - G

LUBRICANT DRY-OFF AND BOUNCE-OFF ON HOT DIE SURFACES: MODEL DEVELOPMENT AND VALIDATION

Lubrication plays a critical role in the efficacy of metal flow, die surface thermal softening, and quality during hot processing of metals. The lubricant is often applied to the hot die surface between 250 to 700^{o}C by spraying a dilute graphite suspension through high pressure nozzles. The atomized droplets in the spray impact on the die surface and undergo film boiling and nucleation boiling. The lubricant film is formed after all the residue liquid on the hot surface is dried off. The evaporation time of droplets is not only a productivity index in hot metal processing but also an important factor for product quality and life of die. This chapter presents an analytical model to estimate the evaporation time of a droplet impact on a die surface heated to temperature beyond Leidenfrost point. Experiments are conducted to measure the dryoff times for lubricants interested. Calculated and experimental evaporation times are compared and agree well for highly diluted lubricants.

G.1 Introduction

In hot deformation processing, the dies are lubricated and cooled by spraying dilute water based lubricants on the heated die surfaces. The lubricant not only cools the hot surface from a temperature as high as 700^{o}C but also deposits a lubricant film that aids in metal flow. For example in hot forging, the lubricant is often a fine suspension of graphite particles in water, with surfactants and binders added to aid in the spreading and the formation of an adherent lubricant film. When droplets of the spray approach the die surface heated to high temperatures, the fast evaporation rate can generate a "cushion" of vapor between the die surface and the droplet to repel the droplet up and support the droplet suspending above the die surface. This is so called film boiling of a droplet. Evaporation time of the droplet not only influences the cooling rate and film formation rate, but also effect of the die life and part quality of the metal processing. Residue liquid lubricant remained in the die can lead to die crack at corners due to high vapor pressure in the forging processes. Entrapped vapors of un-dried lubricant in the melt flow also result in casting porosity for die casting processes. Therefore, the evaporation time of droplets is the key factor to evaluate efficiency of metal processing.

Previous studies on the droplet impact on surface with temperature beyond Leidenfrost have mainly focused on experimental research [King, M.D., 1997; Avedisian, C.T, 1987; Downie, B., 1995; Tamura, Z., 1995]. Early theoretical approaches were limited to model evaporation of a spherical droplet of which kinetic energy is negligible, i.e., the droplet gently seats on the solid surface. Gottfried et al. [Gottfried, B.S., 1966] modeled the film boiling of small droplets deposited on a hot flat at Leidenfrost temperature. The model assumed that the droplet is in isothermal at the saturation temperature. Both conduction and radiation were included in their model and the evaporation rate was found by solving mass, momentum and heat balances equations. Wachters et al. [Wachters, L.H.J., 1966] considered the impact of droplets about 60 μm impacting a heated surface in the range of 5 m/s. Their model yielded an estimate of the height of

the gap between the drop and the surface. Lifetimes of droplets agree well with experimental observations in this study.

Later studies took into account the inertia in the modeling of the impinging droplet. Buyvich et al. [Buyevich, Y.A., 1995] developed a heat transfer model in which they assumed the volume of the droplet to be constant. Heat transfer in the liquid and solid was neglected and only heat transfer in vapor was considered. Rein introduced a disk model in which the inertia of both the droplet and the vapor were considered [Rein, M., 1999]. The disk model did not consider the dynamic of the droplet and took the droplet as a disk with constant radium and thickness. The vapor flow was described as an inviscid flow. Rein showed that the disk model described the main features of the dynamic Leidenfrost phenomenon. Limited droplet impact models were numerically solved by CFD methods. Harvie and Fletcher [Harvie, J.E., 2001] modeled the behavior of the vapor and heat transfer in the solid and droplet using the computational code they named "BOUNCE". Their simulation results were validated by experiments and showed good agreement.

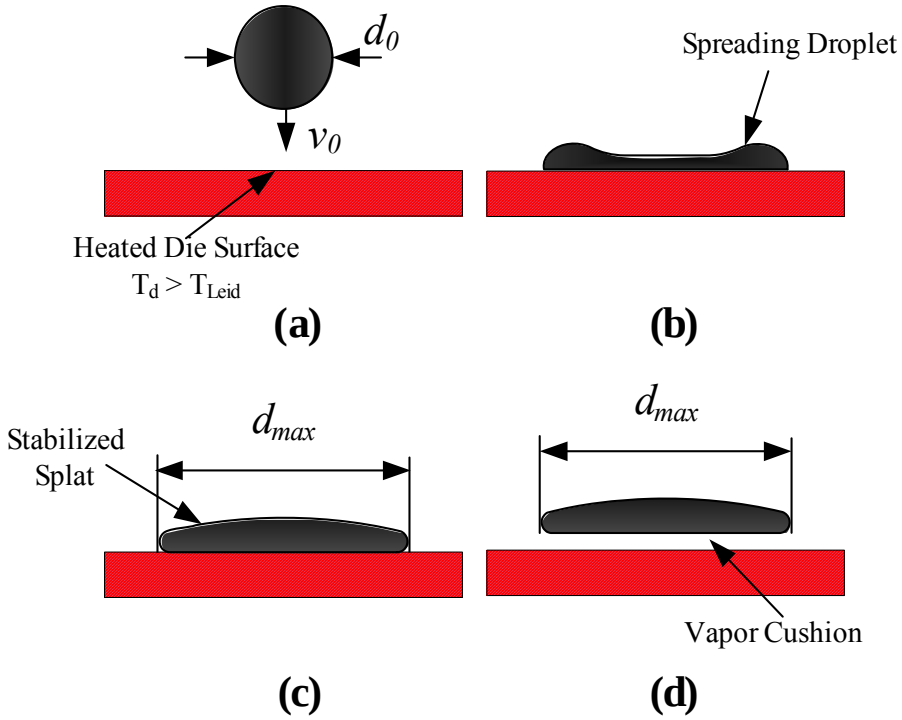

Figure G. 1: Dryoff process of a lubricant droplet at film boiling: (a)- (c) fluid dynamic process, (d). quasi-steady dryoff process.

This appendix presents the analytical model to estimate the dryoff time of a lubricant droplet impact on a die surface at temperature higher than Leidenfrost point. Instead of solving the dynamic and evaporation simultaneously, we will separate the dryoff process into two steps: fluid dynamic process and quasi-steady dryoff process, Fig. E.1. Fluid dynamic process presents the deformation phenomena of the droplet when it impacts on the surface. This model has been discussed in Chapter F. Fig. G.1 (a) demonstrates a droplet of diameter d_0 impact at the heat surface with an initial velocity v_0. The droplet deforms as it hits on the surface and spreads radially. Then the mass of droplet accumulates at the outer ring of the splat and all inertia energy

is converted to surface energy, the droplet recoils back to the center driven by the surface tension force. The dynamic process is stabilized when the conversion cycle between inertia and surface energy ends due to viscous dissipation. This process is shown in (b) and (c) of Fig. G.1. The time it takes to stabilize the deformation process is very short, for example, the time is less than 40 ms for a lubricant droplet of 4 mm diameter with initial impact velocity 1 m/s. The maximum radius the splat is numerically calculated from the fluid dynamic model as we developed for the highly diluted lubricants in Chapter 3. This chapter only cites the results of the fluid dynamic model. Quasi-steady dryoff process is introduced after the droplet deformation is stabilized and kinetic energy has completely converted into surface energy and consumed by viscous dissipation, (d) in Fig. G.1. It is assumed that liquid in lubricant droplet begin to evaporate and lose mass only when quasi-steady dryoff process starts, i.e., kinematic energy of the droplet is not considered. This assumption is justified because the time scale of fluid dynamic (tens of milliseconds) is much smaller than that of the dryoff (tens of seconds).

G.2 Droplet Impact on a Hot Surface

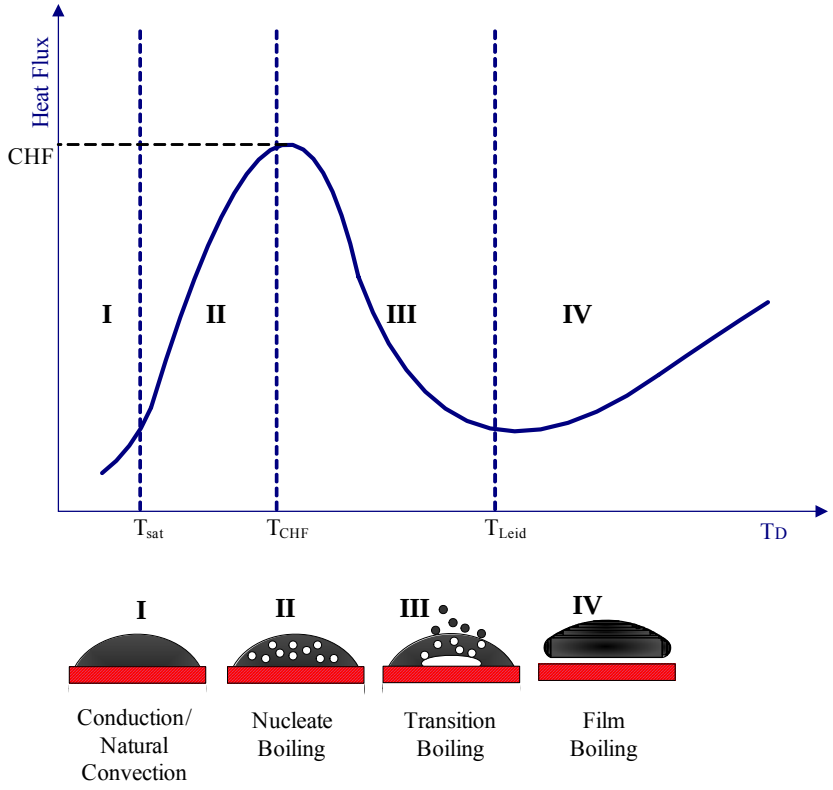

Figure G. 2: Boiling curve of a droplet deposited on a hot solid surface.

In the study of droplet impact on hot surface the following has been observed. At high surface temperatures, vapor forms between the droplet and the surface causing the droplet to bounce off. In water based graphite this leads to pollution with graphite particles depositing on the surrounding surfaces and the press structure. As the surface cools due to heat loss, the droplet

stays on the surface but is separated from it by a vapor blanket. The heat transfer is low in this regime of film boiling in Fig. G.2 (regime IV). The point of least heat flux is called Leidenfrost point. On further cooling of the surface, the droplet enters a regime of transition boiling (regime III in Fig. G.2). The heat starts increasing as the steam can escape from the surface. The heat transfer reaches a maximum when nucleate boiling initiates with vigorous convection (regime II in Fig. G.2). The point of maximum heat transfer is called CHF (critical heat flux). At significantly lower surface temperatures the heat transfer is through natural convection and conduction (regime I in Fig. G.2). This appendix concentrates the study of regime IV which represents working conditions of lubricant spray on the die surface. We will discuss the boiling curve of lubricants in the next chapter.

G.3 Fluid Dynamic Model

The fluid dynamic model for lubricants was developed based on momentum equations. The droplet was modeled as isothermal Newtonian liquid in the model. This model simulates the impact of a liquid droplet on a solid from the moment that the lubricant droplet comes into contact with the die surface and proceeding until the spreading process is completed. The surface tension is included in the model as the linear force to calculate the free moving boundary, part of the solution of governing equation. To evaluate the influence of lubricant properties and spray parameters on the lubricant spreading on the die surface, we simulate impact of lubricants with different dilution ratios, droplet size and impact velocity on a polished die surface.

Summarizing the simulation results, a good log-log linear relationship are found between spreading coefficient $\xi_{\max} = d_{\max}/d_0$ and Weber number $We = \rho_L v_0^2 d_0/\gamma$ for lubricant with dilution ratio higher than 1:5 (volume ratio). Here $d_{\max}$ is the maximum diameter of the splat, d_0 the initial diameter of the droplet, ρ_L the density of droplet liquid, v_0 initial impact velocity, and γ surface tension. The relation is expressed as:

$$\log(\xi_{\max}) = 0.3906 + 0.1038 \log(\mathrm{We}) \qquad \text{(G.1)}$$

Rewriting Equation (G.1), we have:

$$d_{\max} = 2.4581 d_0 \left(\frac{\rho_L v_0^2 d_0}{\gamma} \right)^{0.1038} \quad \text{or} \quad r_{\max} = 2.4581 r_0 \left(\frac{\rho_L v_0^2 d_0}{\gamma} \right)^{0.1038} \qquad \text{(G.2)}$$

where $r_{\max}$ is the maximum radius of the splat, r_0 the initial radius of the droplet.

Since the maximum diameter of the splat was observed very close to the diameter of the splat

when the dynamic process becomes stabilized, we utilize Equation (G.2) as the initial condition of the quasi-steady dryoff model discussed below, shown in Fig. G.1 (d).

G.4 Quasi-steady Dryoff Model

G.4.1 Model Description

The heat flux q due to conduction is given by:

$$q = k_V \frac{\partial T}{\partial z} = k_V \frac{T_D - T_{sat}}{\delta} \tag{G.3}$$

where k_V is the thermal conductivity of the vapor, T_D the temperature of the die surface and T_{sat} the saturation temperature of the lubricant liquid.

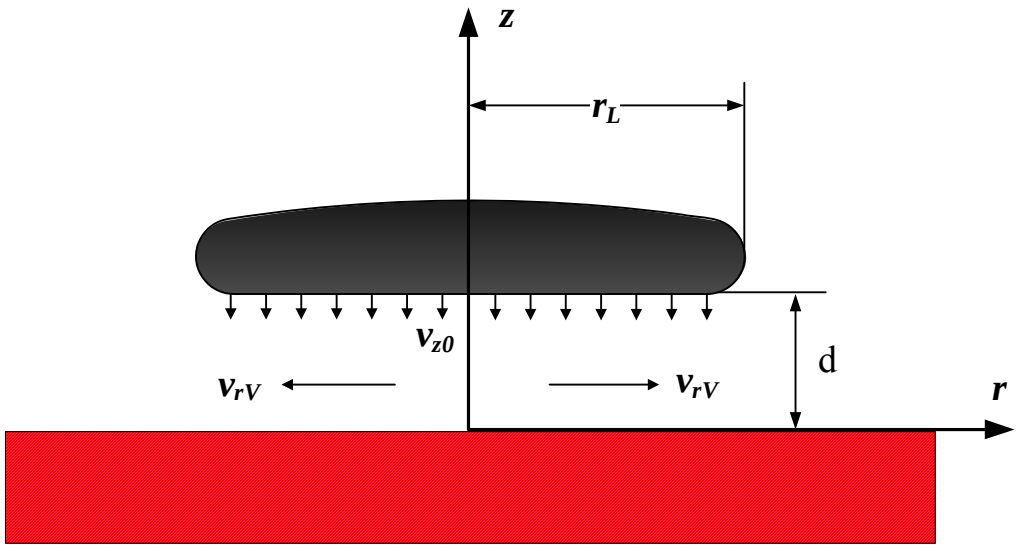

Figure G. 3: Modeling of the quasi-steady dryoff of a lubricant droplet.

So Equation (4.3) can be written as:

$$v_{z0} = -\frac{k_V (T_D - T_{sat})}{L_V \rho_V} \frac{1}{\delta} \tag{G.4}$$

G.4.2 Governing Equations

Assuming the velocity of vapor in z direction ($0 < z < \delta$) is negligible, then the mass balance equation for any radius $r < r_L$ can yield:

$$\int_0^{\delta} v_{rV} 2\pi r dz = \pi r^2 v_{z0} \tag{G.5}$$

Introducing Equation (G.4), Equation (G.5) becomes:

$$\int_0^{\delta} v_{rV} dz = -\frac{k_V (T_D - T_{sat})}{2 L_V \rho_V} \frac{r}{\delta} \tag{G.6}$$

The general form of momentum balance equations in a two dimensional cylindrical coordinates is:

$$\rho_V \left(\frac{\partial v_{rV}}{\partial t} + v_{rV} \frac{\partial v_{rV}}{\partial r} + v_{zV} \frac{\partial v_{rV}}{\partial z} \right) = -\frac{\partial p}{\partial r} + \mu_V \left(\frac{\partial}{\partial r} \left(\frac{1}{r} \frac{\partial}{\partial r} (r v_{rV}) \right) + \frac{\partial^2 v_{rV}}{\partial z^2} \right) \tag{G.7}$$

$$\rho_V \left(\frac{\partial v_{zV}}{\partial t} + v_{rV} \frac{\partial v_{zV}}{\partial r} + v_{zV} \frac{\partial v_{zV}}{\partial z} \right) = -\frac{\partial p}{\partial z} + \mu_V \left(\frac{1}{r} \frac{\partial}{\partial r} \left(r \frac{\partial v_{zV}}{\partial r} \right) + \frac{\partial^2 v_{zV}}{\partial z^2} \right) + \rho_V g \tag{G.8}$$

where p is the pressure and μ_V the viscosity of the vapor.

Because δ is small comparing with r_L, we take the assumptions that: 1). v_{zV} is negligible, 2). the flow of vapor is steady state, i.e., v_{rV} is independent of time, 3). viscous terms in z direction are dominant, i.e., the advection and viscous terms in radial direction are negligible, 4). gravity is not considered. Then the momentum equations reduce to:

$$\frac{\partial p}{\partial r} = \mu_V \frac{\partial^2 v_{rV}}{\partial z^2} \tag{G.9}$$

$$\frac{\partial p}{\partial z} = 0 \tag{G.10}$$

Equation (G.10) indicates that the pressure is a function of r, and Equation (G.9) can be rewritten

as:

$$\frac{\partial^2 v_{rV}(r,z)}{\partial z^2} = \frac{1}{\mu_V}\frac{dp(r)}{dr} \tag{G.11}$$

G.4.3 Analytical Solution

To solve Equation (G.11), boundary conditions at the die surface and droplet bottom surface are needed. Assumption of no-slip at both surfaces is made and it yields:

$$v_{rV} = 0 \text{ at } z = 0 \tag{G.12}$$

and

$$v_{rV} = 0 \text{ at } z = \delta \tag{G.13}$$

Integrating Equation (G.11) twice over z and introducing Equation (G.12) and (G.13) to determine the integral constants, the velocity v_{rV} becomes:

$$v_{rV}(r,z) = \frac{1}{2\mu_V}\left(z^2 - \delta z\right)\frac{\partial p}{\partial r} \tag{G.14}$$

Replacing v_{rV} in Equation (G.14) into mass balance equation (G.6), we have that:

$$\frac{\partial p}{\partial r} = \frac{6\mu_V k_V (T_D - T_{sat})}{L_V \rho_V}\frac{r}{\delta^4} \tag{G.15}$$

Taking another boundary condition that:

$$p = p_0 \text{ at } r = r_L \tag{G.16}$$

and integrating Equation (G.15) yields:

$$p = p_0 + \frac{3\mu_V k_V (T_D - T_{sat})}{L_V \rho_V} \frac{r_L^2 - r^2}{\delta^4} \tag{G.17}$$

Let constant $F_c = \frac{3\mu_V k_V (T_D - T_{sat})}{L_V \rho_V}$, which can be regarded as a characteristic force introduced by the vapor generation, then the pressure is:

$$p = p_0 + F_c \frac{r_L^2 - r^2}{\delta^4} \tag{G.18}$$

It is this pressure that supports the gravity of the droplet. As it is assumed that the droplet is in quasi-steady state and forces exerted on the droplet must be balanced, we have:

$$\int_0^{r_L} \left(p_0 + F_c \frac{r_L^2 - r^2}{\delta^4} - p_0 \right) 2\pi r dr = \rho_L g V \tag{G.19}$$

where ρ_L denotes the density of the lubricant and V the volume of the droplet.

Arranging Equation (G.19), we finally obtain the thickness of the vapor layer as:

$$\delta = \left(\frac{\pi F_c}{2\rho_L g V} \right)^{1/4} r_L \tag{G.20}$$

Let $C = \left(\frac{\pi F_c}{2\rho_L g} \right)^{1/4}$ the coefficient of vapor layer height. Equation (G.20) represents linear relationship between the thickness of the vapor layer δ and the radius of the impact splat r_L for a given volume of the droplet. Since volume of the droplet is a function of time as the liquid continuously escapes as the vapor from the bottom side of the droplet, the height of the vapor δ changes with time.

To calculate the mass loss rate of the droplet, Equation (G.20) is introduced to Equation (G.4):

$$v_{z0} = \frac{k_V (T_D - T_{sat}) V^{1/4}}{C L_V \rho_V} \frac{1}{r_L} \tag{G.21}$$

The splat radius r_L in equation (G.21) can be approximated as the maximum radius r_{max} of the splat fitted by the fluid dynamic model, which is given by the Equation (G.2). The volume of the droplet V changes as a function of mass loss rate $\dot{m}$ and time t:

$$V(t) = V_0 - \frac{1}{\rho_L}\int_0^t \dot{m}dt \tag{G.22}$$

where $V_0 = \frac{\pi d_0^3}{6}$ is the initial volume of the droplet and $0 \le t < t_{dry}$. t_{dry} is the droyoff time.

Introducing Equations (G.21) and (G.22), then the mass loss rate is:

$$\dot{m} = \int_0^{r_L} \rho_V v_{z0} 2\pi r dr = \frac{\phi}{r_L}\int_0^{r_L} r\left(V_0 - \frac{1}{\rho_L}\int_0^t \dot{m}dt\right)^{1/4} dr \tag{G.23}$$

where $\phi = \frac{2\pi k_V (T_D - T_{sat})}{CL_V}$ and $r_L = 1.2291 r_0 \left(\frac{\rho_L v_0^2 d_0}{\gamma}\right)^{0.1038}$.

Since the vapor leaves evenly along the radial direction of the bottom surface of the droplet, $\dot{m}$ is independent of r. Therefore, the term $\left(V_0 - \frac{1}{\rho_L}\int_0^t \dot{m}dt\right)^{1/4}$ can be taken out of the integral and Equation (G.23) can be rewrite as:

$$\dot{m}\left(V_0 - \frac{1}{\rho_L}\int_0^t \dot{m}dt\right)^{-1/4} = \frac{\phi r_L}{2} \tag{G.24}$$

To find the solution of this nonlinear equation, we have to use numerical iteration techniques. This paper uses Gauss-Newton method to find the solutions of mass loss rate $\dot{m}(t)$ as a function of time t. The mass loss rate becomes unstable and unreasonably small during the computation when evaporation time $t \to t_{dry}$ or the volume of the droplet $V \to 0$. To compensate this but not lose the power of the model, we applied $\dot{m}(t_{90\%})$, the mass loss rate at which the remaining volume of droplet is exactly 10% of the initial volume of the droplet, to be the mass lost rate for the rest process of evaporation till all droplet has been dried off.

If we assume that there is no mass loss in the dynamic process and mass loss only caused by evaporation in the quasi-steady dryoff stage, droyoff time of the lubricant droplet in boiling region t_{dry} is given by:

$$m_0 = \int_0^{t_{dry}} \dot{m} dt \qquad \text{(G.25)}$$

where m_0 is the initial mass of the droplet and $m_0 = \frac{\rho_L \pi d_0^3}{6}$. Again, solving Equation (G.25) numerically using the results from Equation (G.24), we can finally obtain the dryoff time $t_{dry.}$

G.5 Experiment Setup

In this research, the fluid dynamics and thermal behaviors of a droplet impacting on a hot die were experimentally studied by water-based graphite lubricant commonly used in hot forging process. The experiment setup is similar to the one described previously except thermal measurement configuration is included in this experiment. Again, graphite-based lubricant with 54% solid content (weight %) is diluted by distilled water to 1:1, 1:5, and 1:20 before experiment. Droplets of these diluted ratios are used in the experiment. Properties of droplets are measured by experiments. The results of properties are shown in Chapter F. As illustrated in Fig. G.4, lubricant droplets were generated by a droplet generator with tip diameters of 1.0mm, 1.5mm, and 2.0mm, and made to fall down onto a flat H13 die under their own gravity. Impact velocities were obtained by changing height of the droplet generator "*H*" and the range of velocity was controlled at levels of 10cm/s continuously to 200cm/s. A camcorder took pictures at the moment a droplet formed. The impact behaviors of the droplet were also recorded by a speed camera. The images were later sent to computer for imaging processing to measure deposition dimensions and dryoff time. Dryoff time was also measured through a stop watch with precision of 0.01s. The flat die surface was finished to roughness Ra 50μ inch (or 1.25μm). The die was mounted around by an induction bind heater whose temperature was adjustable from room temperature to 450^{o}C. Temperature at die surface was measured by embedded fast response thermocouples (response time≤ 2ms) which right beneath the impacting area of the die surface. The distance of thermocouple tips to the die surface is 0.5 mm, 1 mm and 1.2 mm separately. The voltage signals of thermocouples were sent to National Instrument (NI) Data Acquisition System so that the temperature could be monitored and recorded. The thermodynamic properties of vapor, which is regarded as gas phase of water in this study, are function of temperature and pressure and are calculated using fitting equations recommended in [Wagner, W.,, 2002; Saul, A., 1989; IAPWS, 1997].

G.6 Results and Discussion

Fig. G.5 shows the time-averaged vapor thickness calculated by the dryoff model versus die

surface temperature for droplets with different Weber numbers. Since most of the lubricants interested demonstrate Leidenfrost points a few degrees lower than 300°C [Yang, L., 2005], we start temperature at 305°C to locate the study in the film boiling regime.

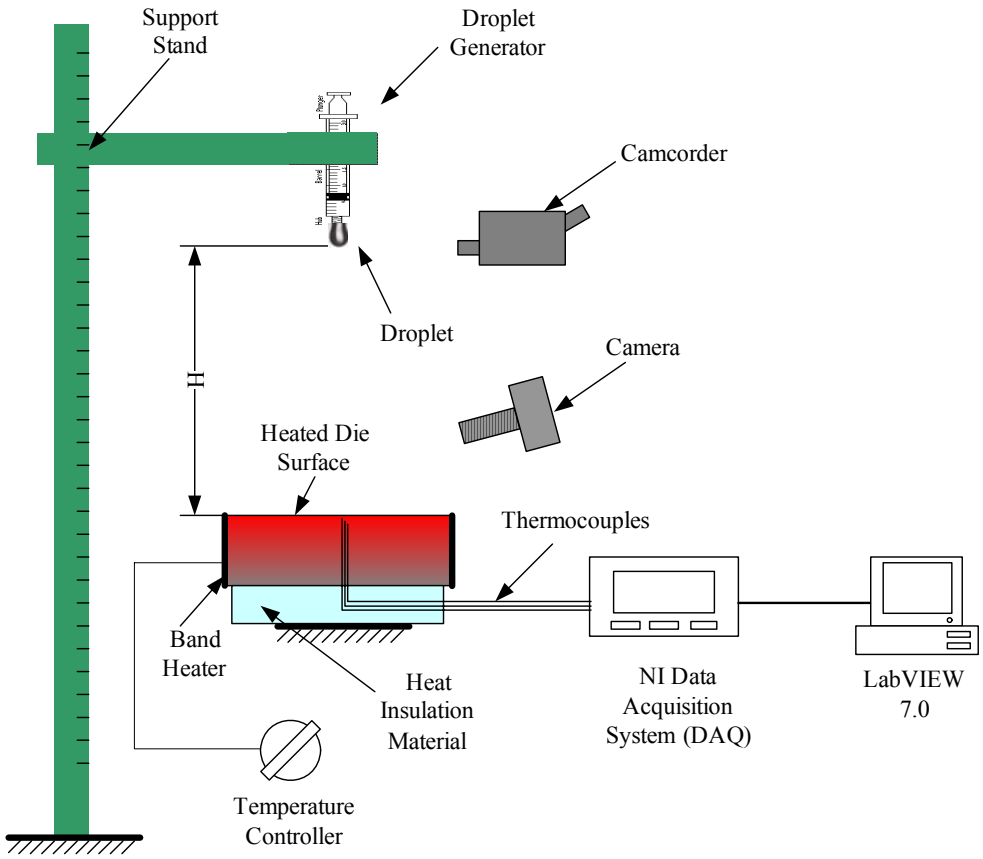

Figure G. 4: Schematic experiment setup.

From Fig. G.5, the thickness of the vapor layer ranges from around 28 μm to 127 μm. Though there are limited experimental data on the thickness of the vapor layer, Chandra and Aziz [Chandra, S., 1994] measured the thickness of the vapor layer between a deposited nitrogen droplet and a glass surface. They measured the thickness by enlarging the images taken in the experiments for different droplet sizes. The results of thickness of vapor layer beneath the evaporating nitrogen droplet range from 15 μm to 50 μm in their experiments. Since their measurements did not consider the inertia energy and thermal effects, the calculated thickness of the vapor layer by the dryoff model agree well on the magnitude of the results obtained by Chandra and Aziz at low surface temperatures and low Weber numbers.

One can observe from Fig. G.5 that the height of the vapor layer increases with temperature, evidently at temperatures beyond 370 °C, for all droplets with different Weber number. This is because that the thermal conductivity k of vapor changes dramatically from 0.1815 W/m/K at 370°C to 0.3238 W/m/K at 380°C [Yang, L., 2005]. The enhanced conduction generates more

vapor than it can be promptly transported to the outside of the shaded area of the droplet and increases the pressure of the vapor layer p. The increased pressure difference $p - p_0$ lifts the droplet, and in return, the widened gap decreases the vapor pressure p until the pressure difference $p - p_0$ drops to a level just right to support the weight of droplet, see Equation (G.15).

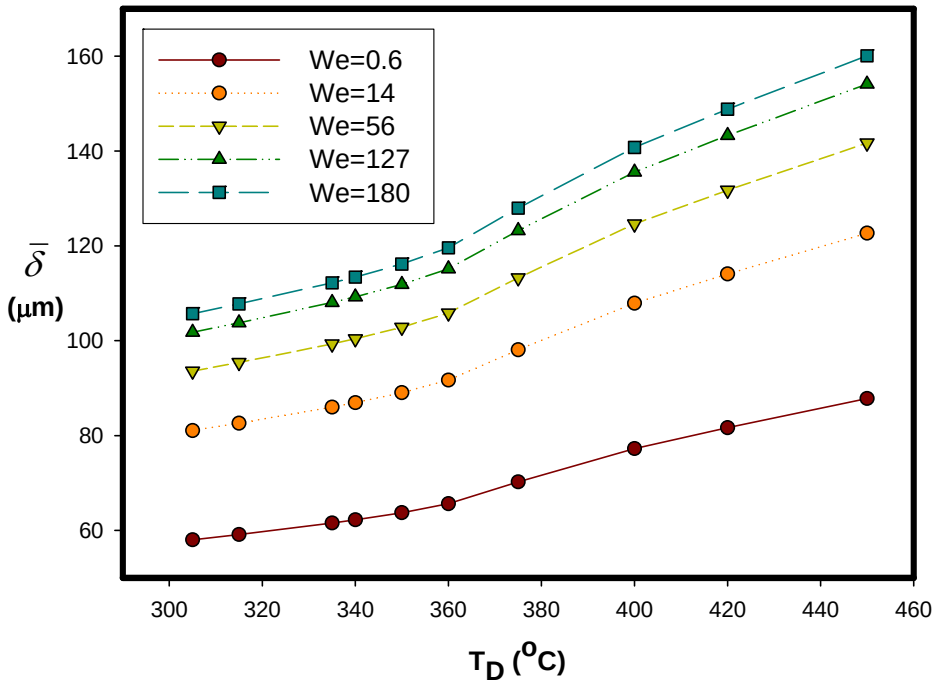

Figure G. 5: Averaged thickness of the vapor layer as a function of temperature and Weber number.

Moreover, the thickness of vapor layer increases with the Weber number *We*, illustrated in Fig. 4.5. This is mainly because that, as it can be read from Equation (4.2), high Weber number brings about large spreading radius r_L which enlarges the heat contact area and improves the evaporation. Another direct explanation is that enlarged contact area needs lower pressure to support the weight of the droplet than it does for a smaller contact area, and thereby, a larger vapor layer height. As Weber number of the droplet continues to increase, the thickness of the vapor layer does not increase accordingly for all range of Weber number. Instead, a different physical phenomenon is introduced for droplet-surface interactions of high Weber number. Studies have shown that droplets of the lubricant break up on die surface at room temperature normally at Weber number *We* greater than 180, a critical Weber number which can be lower for a heated die surface [Yang, L., 2005]. Fig. G.5 indicates that the vapor generated by severe evaporation at high temperature may introduce high transient pressure and help to blow the droplet apart.

Fig. G.6 illustrates the time-weighted averaged mass loss rate $\dot{m}$ versus die surface temperature for different Weber numbers. The increase of mass loss rate $\dot{m}$ with die temperature correlates with the trend of the thickness of vapor layer shown in Fig. G.5. The mass loss rate is also observed to increase with Weber number. This is also caused by enhanced heat transfer due to large diameters of splat for a high Weber number impact, demonstrated by our fluid dynamic model. It should be noted that the density of the vapor increases with temperature [Wagner, W., 2002; Saul, A., 1989]. Therefore, even if the velocity of the vapor leaving from the droplet keeps the same, the higher temperature will result in more mass to be taken out by the vapor. This explains the observation that the mass loss accelerates at the high temperature illustrated in Fig. G.6.

The dryoff times calculated for a lubricant droplet with initial diameter d_0 = 3mm are shown in Fig. 4.7 comparing with the dryoff times obtained through experiments. The droplets impact on the die surface at two impact velocities: 0.1 m/s and 1 m/s. The calculated dryoff times for droplets with impact velocity v_0=0.1 m/s are in the range of 70-90 s, while the range for those measured in experiments is 63-75 s. The comparison for those droplets with impact velocity v_0=1 m/s also shows that dryoff times calculated by the model are of the correct order comparing with those measured in the experiment (27-40 s from the model and 34-64 s from experiments).

The interesting finding is that the model predicts longer dryoff times than the times observed in the experiments for droplets at low impact velocity, but it is opposite for those with a relatively high velocity.

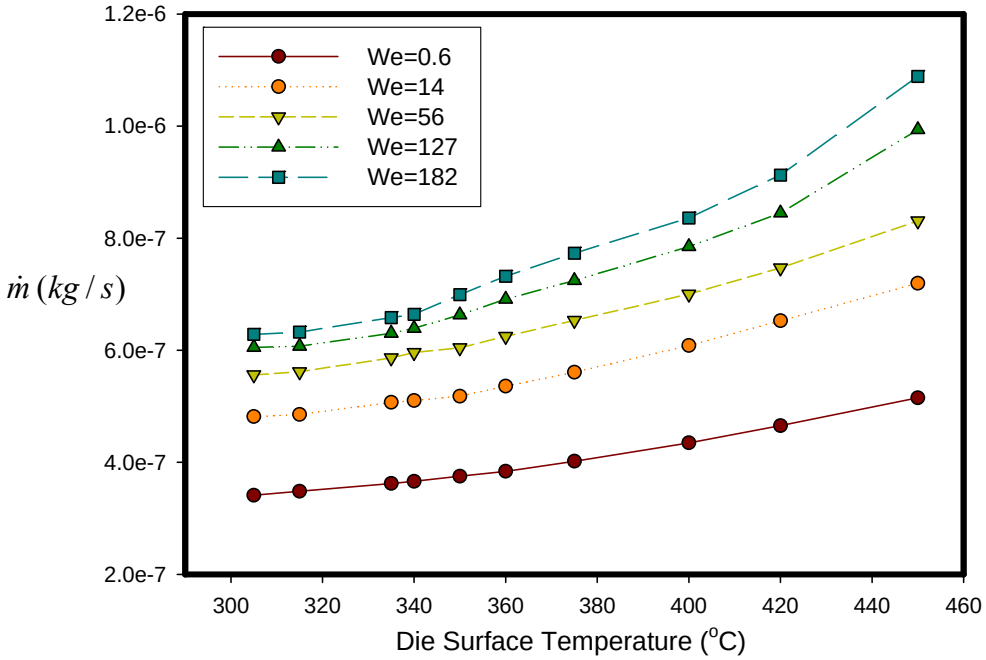

Figure G. 6: Averaged mass loss rate as a function of temperature and Weber number.

The presence of lower prediction for high impact velocity droplets can be explained by the assumption made in the model that the spreading radius, calculated from fluid dynamic model, does not change with time afterwards at the quasi-steady dryoff stage. This may not reflect the droplet dryoff process very well especially at the late life of the droplet. In fact, the droplets were observed to draw back to a spheroidal shape after impact because of high surface tension at vapor-liquid interface. This behavior reduces the contact area of droplet with die surface and depresses the heat transfer. As the vapor takes more and more mass from the lubricant droplet, the Bond number $Bo = \rho g d_0^2 / \gamma$, a ratio of the gravity to capillary effects, becomes smaller and smaller and capillarity solely determines the shape of the droplet. At this end stage of dryoff, the shape of the droplet is almost spherical, which is the poorest geometry condition for heat conduction. The higher calculated dryoff times for droplets with a low impact velocity may be caused by the underestimate of the spreading radius by the fluid dynamic model. A further study on the effect of graphite suspensions on dry off should also be conducted because it is observed in the experiments that graphite accumulate at the bottom of the droplet when liquid leaves from the bottom of droplet as a form of vapor. The graphite forms a porous phases through which the liquid passed and evaporates to compensate the mass loss in the vapor layer. This phenomenon is not considered in the analytical mode discussed above and may contribute the discrepancy of the prediction and experimental results.

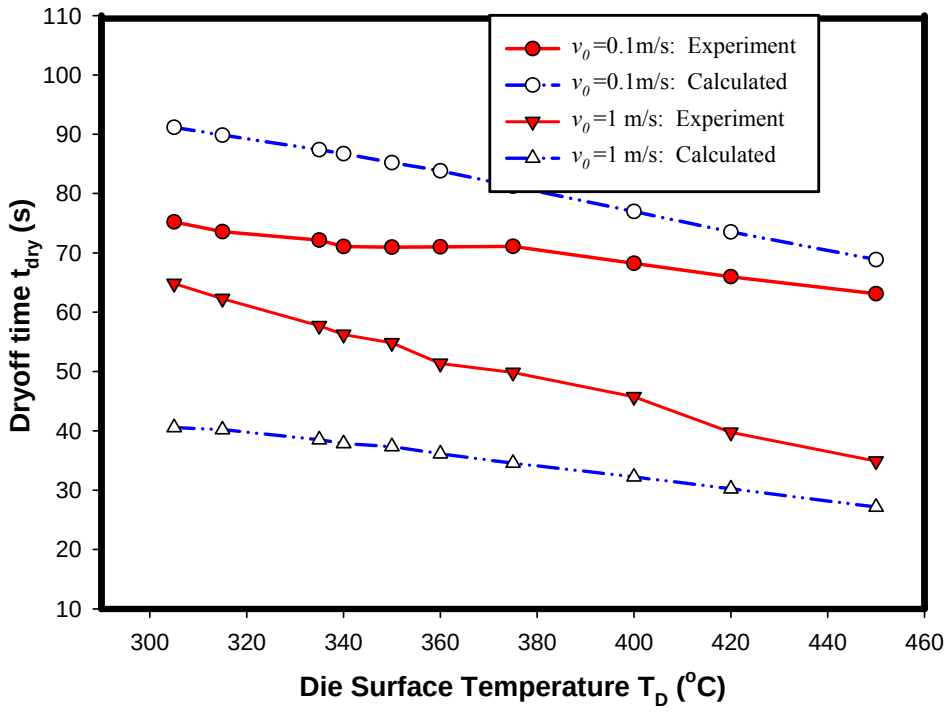

Figure G. 7: Dryoff time of a droplet with initial diameter d_0=3mm.

G.7 Summary

A model has been developed to predict the dryoff time of a lubricant droplet impact on a die surface heated to temperatures beyond Leidenfrost point. This model couples two components: fluid dynamic model presented at a separate paper, and quasi-steady dryoff model. Thickness of vapor layer and mass loss rate have been calculated from the model. It is shown that thickness of vapor and mass loss rate are correlated with each other and both increase with die surface temperature and Weber number *We*. Validation of the model is accomplished by comparing dryoff times computed by the model and those observed in the experiments. The calculated results agree with the experimental results in the right magnitude.

References

Akao, F., Araki, K., Mori, S., and Moriyama, A.: Deformation behaviors of a liquid droplet impinging onto hot metal surface, Trans. Iron Steel Inst. Japan, 20, 737, 1980.

Aoyama, S., Akase, M., Sakamoto, K., and Umemura, T., Die lubricant deposit and its effect on ejection in die casting, Trans. NADCA, 335-341, 1991.

Avedisian, C.T, Koplik, J., Leidenfrost boiling of methanol droplets on hot porous/ceramic surfaces, Int. J. Heat Mass Transfer 30, 1587–1603, 1987.

Banerjee, R., Collins, P. C., and Fraser, H. L., "Laser Deposition of In Situ Ti and TiB Composites," Advanced Engineering Materials, Vol. 4, No. 11, pp. 847 - 851, 2002.

Bariani, P. F., Dal Negro, T., Masiero, S.: Experimental evaluation and FE simulation of thermal conditions at tool surface during cooling and deformation phases in hot forging applications, Annals CIRP, 51/1/ 219-222, 2002.

Bariani, P. F., Dal Negro, T. and Masiero, S: Influence of coolant spray conditions on teat transfer at die surface in hot forging, Proc. 7th ICTP, Yokohama, Vol.1, 781-786, 2002.

Bender, J. W., and Wagner, N. J., J, Optical measurement of the contributions of colloidal forces to the rheology of concentrated suspensions, Colloid Interface Sci. 172, 171, 1995.

Bernardin J.D., Stebbins C.J., Mudawar I., Mapping of impact and heat transfer regimes of water drops impinging on a polished surface, Int. J. Heat Mass Transfer 40, 247–267, 1997.

Boersma, W. H., Laven, J., and Stein, H. N., J., Computer simulations of shear thickening of concentrated dispersions, Rheol. 39, 841, 1995

Boddu, M. R., Landers, R. G., and Liou, F. W., "Control of Laser Cladding For Rapid Prototyping – A Review," presented at Solid Freeform Fabrication Proceedings, Austin, TX, 2001.

Bolle L., Moureau J.C., Spray cooling of hot surfaces, in: J.D. Hewitt, N. Zuber (Eds.), Multiphase Science and Technology, Hemisphere, New York, 1–92, 1981.

Bussmann, M, Mostaghimi, J., Chandra, S.: On a three-dimensional volume tracking model of droplet impact, Physics of Fluids, Vol. 11, pp. 1406-1417, 1999.

Buyevich, Y.A., Mankevich, V.N., Interaction of a dilute mist flow with a hot body, Int., J., Heat Mass Transfer 38, 731-744, 1995.

Chandra, S., Avedisian, C.T.: On the collision of a droplet with a solid surface, Proc. R. Soc. London A 432, 13–41, 1991.

Chandra, S. and Aziz, S.D., Leidenfrost evaporation of liquid nitrogen droplets", ASME Journal of Heat Transfer ,116, pp. 999-1006, 1994.

Collins, P. C., Banerjee, R., and Fraser, H. L., "The influence of the enthalpy of mixing during the laser deposition of complex titanium alloys using elemental blends," Scripta Materialia, Vol. 48, No. 10, pp. 1445-1450, 2003.

Doege, E., Alasti, M., Schmidt-Jurgensen, R., Accurate friction and heat transfer laws for enhanced simulation models for precision forging processes, J. Matl. Proc. Tech., 150, 92-99, 2004.

Downie, B., Polymeropoulos, C., Gogos, G., Interaction of a water mist with a buoyant methane diffusion flame, Fire Safety J. 24, 359–381, 1995.

Engel, O.G.: Waterdrop collisions with solid surfaces, J. Res. NBS 5, 281–298, 1955.

Fischer, P., Karapatis, N., Romano, V., Glardon, R., and Weber, H. P., "A model for the interaction of near-infrared laser pulses with metal powders in selective laser sintering," Applied Physics A Materials Science & Processing, Vol. 74, No. 4, pp. 467 - 474, 2002.

Fischer, P., Romano, V., Weber, H. P., Karapatis, N. P., Boillat, E., and Glardon, R., "Sintering of commercially pure titanium powder with a Nd:YAG laser source," Acta Materialia, Vol. 51, No. 6, pp. 1651-1662, 2003.

Fu, Y., Loredo, A., Martin, B., and Vannes, A. B., "A theoretical model for laser and powder particles interaction during laser cladding," Journal of Materials Processing Technology, Vol. 128, No. 1-3, pp. 106-112, 2002.

Fukai, J., Zhao, Z., Poulikakos, D.: Modelling of the deformation of a liquid droplet impinging upon a flat Surface, Physics of Fluids A 5, 2588-2599, 11, 1993.

Gottfried, B.S., Lee, C.J., Bell, K.J., The Leidenfrost phenomenon: Film boiling of liquid droplets on a flat plate, Int. J. Heat Mass Transfer 9, 1167-1187, 1966.

Griffith, M. L., Ensz, M. T., Puskar, J. D., Robino, C. V., Brooks, J. A., Philliber, J. A., Smugeresky, J. E., and Hofmeister, W. H., "Understanding the microstructure and properties of components fabricated by Laser Engineered Net Shaping (LENS)," Materials Research Society Symposium - Proceedings, Vol. 625, pp. 9-20, 2000.

Grujicic, M., Hu, Y., Fadel, G. M., and Keicher, D. M., "Optimization of the LENS Rapid Fabrication Process for In-Flight Melting of Feed Powder," Journal of Materials Synthesis and Processing, Vol. 9, No. 5, pp. 223-233, 2001.

Harlow, F.H. and Welch, J.E.: Numerical calculation of time-dependent viscous incompressible flow of fluid with free surface, The Physics of Fluids, Volume 8, pp.1029-2332, December, 1965.

Harvie, J.E. and Fletcher, D.F., A hydrodynamic and thermodynamic simulation of droplet impacts on hot surfaces, Part I： theoretical model, Int. J., Heat and Mass Transfer, Vol. 44, pp.2633-2642, 2001.

Horsky, J., Raudensky, M., Sauer, W.: Experimental study of cooling characteristics in hot rolling, J. Mater. Proc., Tech., 45, pp. 131-135, 1994.

Hu, Y. P., Chen, C. W., and Mukerjee, K., "Development of a new laser cladding process for manufacturing cutting and stamping dies," Journal of Materials Science, Vol. 33, No. 5, pp. 1287-1292, 1998.

IAPWS, Revised Release on the IAPS Formulation 1985 for the Viscosity of Ordinary Water Substance, International Association for the Properties of Water and Steam, Erlangen, Germany, 15, 1997.

Inada, S., Miyasaka, Y., Mishida, K., and Chandratilleke, G.R.: Transient temperature variation of a hot wall due to an impinging water drop: effect of subcooling of the water drop, Proceedings of the Joint ASME/ JSME Thermal Engineering Conference, Vol. 1, ASME, 173– 182, 1983.

J. A. Brooks, C. V. Robino, T. Headley, S. Goods, R. C. Dykhuizen, and M. L. Griffith, "Microstructure and Property Optimization of LENS® Deposited H13 Tool Steel," presented at Solid Freeform Fabrication Symposium, Austin, TX, 1999.

Jeong, D. J., Kim, D. J., Kim, J. H., Kim, B. M., and Dean, T. A., "Effects of surface treatments and lubricants for warm forging die life," Journal of Materials Processing Technology, Vol. 113, No. 1-3, pp. 544-550, 2001.

Kang, J. H., Park, I. W., Jae, J. S., and Kang, S. S., "A study on a die wear model considering thermal softening: (I) Construction of the wear model," Journal of Materials Processing Technology, Vol. 96, No. 1-3, pp. 53-58, 1999.

Kang, J. H., Park, I. W., Jae, J. S., and Kang, S. S., "A study on die wear model considering thermal softening (II): Application of the suggested wear model," Journal of Materials Processing Technology, Vol. 94, No. 2-3, pp. 183-188, 1999.

Kar, A. and Mazumder, J., "Laser chemical vapor deposition of thin films," Materials Science & Engineering, Vol. B41, No. 3, pp. 368-373, 1996.

Kathuria, Y. P., "Laser-cladding process: a study using stationary and scanning CO2 laser beams," Surface and Coatings Technology, Vol. 97, No. 1-3, pp. 442-447, 1997.

Ki, H., Mohanty, P. S., and Mazumder, J., "Modelling of high-density laser-material interaction using fast level set method," Journal of Physics D: Applied Physics, Vol. 34, No. 3, pp. 364-372, 2001.

King, M.D., Yang, J.C., Chien, W.S., Grosshandler, W.L., Evaporation of a small water droplet containing an additive, Proceedings of the ASME National Heat Transfer Conference, Baltimore, MD, 1997.

Ko Y.S., Chung S.H., An experiment on the breakup of impinging droplets on a hot surface, Expt. Fluids 21, 118–123, 1996.

Lass H.: Vector and Tensor Analysis, McGraw-Hill, New York, 1950.

Lewis, G. K. and Schlienger, E., "Practical considerations and capabilities for laser assisted direct metal deposition," Materials and Design, Vol. 21, No. 4, pp. 417-423, 2000.

Li, Y. and Ma, J., "Study on overlapping in the laser cladding process," Surface and Coatings Technology, Vol. 90, No. 1-2, pp. 1-5, 1997.

Lin, J. and Hwang, B.-C., "Clad profiles in edge welding using a coaxial powder filler nozzle," Optics and Laser Technology, Vol. 33, No. 4, pp. 267-275, 2001.

Liu, C.-C. and Huang, J.-L., "Effect of the electrical discharge machining on strength and reliability of TiN/Si3N4 composites," Ceramics International, Vol. 29, No. 6, pp. 679-687, 2003.

Liu, G.W., Morsi, Y.S., Clayton, B.R, Characterisation of the spray cooling heat transfer involved in a high pressure die casting process, Int. J. Thermal Science 39, 582-591, 2000.

Makino, K., Michiyoshi, I.: The behavior of a water droplet on heated surfaces, Int. Journal of Heat Mass Transfer, Vol, pp.781-791, 1984.

Manzello, S.L. and Yang, J.C.: Experimental study of high Weber number impact of Methoxy-Nonafluorobutane C4F9OCH3 (HFE-7100) and n-heptane droplets on a heated solid surface, Int. J. of Heat and Mass Transfer, Vol. 45, No.19, 3961-3971, 2002.

Miller, R. S., Cao, G., and Grujicic, M., "Monte Carlo Simulation of Three-Dimensional Nonisothermal Grain-Microstructure Evolution: Application to LENS Rapid Fabrication," Journal of Materials Synthesis and Processing, Vol. 9, No. 6, pp. 329-345, 2001.

Ming, Q., Lim, L. C., and Chen, Z. D., "Laser cladding of nickel-based hardfacing alloys," Surface and Coatings Technology, Vol. 106, No. 2-3, pp. 174-182, 1998.

Pasandideh-Fard, M., Chandra, S., Mostaghimi, J.: a Three-dimensional model of droplet impact and solidification, Int. J. Heat Mass Trans. 45, 2229-2242, 2002.

Pasandideh-Fard, M., Aziz, S. D., Chandra, S. and Mostaghimi, J.: Cooling effectiveness during the impact of cold water droplets on a hot steel plate: simulations and experiments, International Journal of Heat and Fluid Flow, 22, pp. 201-210, 2001.

Qian, M., Lim, L. C., Chen, Z. D., and Chen, W. L., "Parametric Studies of Laser Cladding Processes," Journal of Materials Processing Technology, Vol. 63, No. 1-3, pp. 590-593, 1997.

Quiao, Y.M., Chandra, S., Experiments on adding a surfactant to water drops boiling on a hot surface, Pro. R. Soc. Lond. A, 453, 673-689, 1997.

Rein, M., Phenomena of liquid droplet impact, Fluid Dyn. Res. 12, 61–93, 1993.

Rein, M., The reflection of drops off hot surfaces, Math. Mech., 79(S3): S743-S744, 1999.

Reiners, U., Jeschar, R., Scholz, R., Measuring method for quick determination of local heat transfer coefficients in spray water cooling within the range of stable film boiling, Steel Research 56,1985.

Saiki, H., Marumo, Y., Minami, A., and Sonoi, T., "Effect of the surface structure on the resistance to plastic deformation of a hot forging tool," Journal of Materials Processing Technology, Vol. 113, No. 1-3, pp. 22-27, 2001.

Saul, A.; Wagner, W., A Fundamental equation for water covering the range from the melting line to 1273 K at pressures up to 25000 MPa, J. Phys. Chem. Ref. Data, 18, 4, 1537-1564, 1989.

Savic, P. and. Boult. G.T.: The fluid flow associated with the impact of liquid drops with solid surfaces, National Research. Council of Canada, Report No. MT-26, 1955.

Savic, P.: The cooling of a hot surface by drops boiling in contact with it. Report no. MT-26, National Research Council of Canada , Ottawa, 1958.

Sexton, L., Lavin, S., Byrne, G., and Kennedy, A., "Laser cladding of aerospace materials," Journal of Materials Processing Technology, Vol. 122, No. 1, pp. 63-68, 2002.

Toda, S.: A study of mist cooling - 2nd Report: Theory of mist cooling and its fundamental experiments,

Heat Transfer Japan, Res., 3, No.1, pp. 1–44, 1974.
Tamura, Z., Tanasawa, Y., Evaporation and combustion of a drop contacting with a hot surface, Proc. Combust. Inst. 7, 509–522, 1959.
Trapaga, G., Szekely, J.: Mathematical modeling of the isothermal impingement of liquid droplets in spraying processes, Metall. Trans. B, 22B, 901, 1991.
Tseng, A.A., Lin, F.H., Gungeria, A.S., and Ni, D.S.: Roll cooling and its relationship to roll life, Metallurgical Transactions, Vol. 20A, 1989.
Vasinonta, A., Beuth, J. L., and Griffith, M. L., "Process Maps for Controlling Residual Stress and Melt Pool Size in Laser-based SFF Processes," presented at Solid Freeform Fabrication Proceedings, Austin, TX, 2000.
Wachters, L.H.J., Westerling, N.A.J.: The heat transfer from a hot wall to impinging water drops in a spheroidal state, Chem. Eng. Sci. 21, 1047–1056, 1966.
Wagner, W., Pruss, A., The IAPWS formulation 1995 for the thermodynamic properties of ordinary water substance for general and scientific use, J. Phys. Chem. Ref. Data, 31, 2, 387-535, 2002.
Yang, L., Liu, C., Shivpuri, R.: Comprehensive approach to film formation, pollution and heat transfer in hot die lubrication, Proceedings of the ICTP, 2005.
Yang, L., Liu, C., Shivpuri, R.: Physiothermodynamics of lubricant deposition on hot die surfaces, Annals of the CIRP, 54/1, 2005.
Yevko, V., Park, C. B., Zak, G., Coyle, T. W., and Benhabib, B., "Cladding formation in laser-beam fusion of metal powder," Rapid Prototyping Journal, Vol. 4, No. 4, pp. 168-184, 1998.
Zhao, Z., Poulikakos, D. and Fukai, J.: Heat transfer and fluid dynamics during the collision of a liquid droplet on a substrate: I-modeling," International Journal of Heat and Mass Transfer, Vol. 39, pp. 2771-2789, 1996.